A Frequency-Constrained MILP Framework for Power System Restoration Planning

by

Xiangyu (Harry) Zou

A thesis submitted in conformity with the requirements
for the degree of Master of Applied Science

Edward S. Rogers Sr. Department of Electrical and Computer Engineering
University of Toronto

A Frequency-Constrained MILP Framework for Power System Restoration Planning

Xiangyu (Harry) Zou
Master of Applied Science
Edward S. Rogers Sr. Department of Electrical and Computer Engineering
University of Toronto
2025

Abstract

Power system restoration plans involve sequences of operator actions, such as line energization and load pick-up. During the planning process, operators must be mindful of the system dynamics that follow each restorative action and ensure that they fall within safe limits. In this thesis, we formulate a frequency-constrained mixed-integer linear program (MILP) for black-start restoration planning of transmission systems. First, we use a DC power flow model to construct an optimization framework for generator and load recovery. Next, we introduce a novel method to predict the system's frequency nadir by analyzing the IEEEG1 governor-turbine model for synchronous generators. The predictions are linearized by an iterative receding-horizon algorithm and inserted into the MILP as constraints on the power imbalance introduced by each action. We further build upon this framework by allowing energy storage systems (ESS) to participate in the restoration process. We show how frequency security and recovery speed can be improved by coordinating the ESS setpoints with restoration actions. Case studies are simulated on MATLAB and PSS/E to show the effectiveness of the proposed frequency nadir estimation and restoration planning methods. Finally, we demonstrate the flexibility of the proposed framework by recommending some possible extensions.

To my loving grandparents.

Acknowledgements

First, I would like to express my sincere gratitude to my supervisor, Professor John Simpson-Porco, for his invaluable support and encouragement throughout my time as a master's student. Our discussions each week were "persistently exciting" and thought-provoking, and I always came out with more clarity on my next steps. Moreover, I am deeply grateful to Professor Simpson-Porco for introducing me to the field of control systems, of which I had little prior knowledge in. It has been a pleasure to learn under your guidance, and working with you has had a great influence on my decision to pursue a Ph.D.

This work would not have been possible without the contributions from my collaborators and mentors, Dr. Ilyas Farhat and Professor Sunghoon Lim. During various stages of this project, your thoughtful ideas and suggestions have provided clarity and guidance.

I would also like to thank the members of my thesis committee, Professor Zeb Tate and Professor Peter Lehn, for their perspectives and feedback on my thesis. Your time and commitment are greatly appreciated. In particular, Professor Tate's guidance during my undergraduate studies was pivotal to my interest in power systems research. Thank you for your unwavering support throughout my time at the University of Toronto.

To my parents, your dedication to my education has been the foundation for all my academic pursuits. I would not be here if not for everything you have done for me. To my grandparents, thoughts of you have given me the resolve to power through times of difficulty.

Finally, I would like to appreciate all of my dear friends. Through all the stress and worries, smiles and laughter, thank you for being a part of this journey.

Contents

List of Tables

List of Figures

Chapter 1

Background

1.1 Introduction

Modern power systems face unprecedented threats from severe weather and cyber attacks [1]. These high impact, low probability events may cause widespread outages with significant potential financial and human costs. Power outages cause up to $50 billion dollars in financial loss annually in the United States alone [2], while individual large-scale events such as the Northeastern blackout of 2003 affected 50 million people and incurred an estimated $6 billion in losses [3]. Damages and risks increase with the duration of the outage [2], highlighting the need for fast grid recovery strategies. To prepare for outage scenarios, Independent System Operators (ISOs) proactively develop restoration plans, which include guidelines or specified actions that assist decision making during grid recovery [4].

Following a complete blackout, all network components are offline, and an initial source of power is required for system re-energization. ISOs designate several synchronous generators (SGs), often hydro or gas turbine units, as black-start units (BSUs) capable of self-starting without external power [5]. Crucially, these units provide power support to non-black-start units (NBSUs), which cannot start up by themselves [6]. Black-start restoration can be characterized by four phases: sectionalization, generator recovery, load recovery, and synchronization [7]. First, the grid is sectioned into multiple regions, each with exactly one BSU, to be restored in parallel as individual subsystems. This strategy makes better use of the BSUs and accelerates system recovery [6]. During the generator recovery phase, the BSUs provide power to the NBSUs while energizing transmission lines along the way. The loads are picked up primarily to balance the system and maintain voltage levels, with the exception of important loads such as critical infrastructure or communication services, which are prioritized [8]. Early generator recovery provides access to additional power capacity and improves the resilience of the system to disturbances by increasing its inertia [8]. The transition toward load recovery is not clearly defined—the focus progressively shifts toward rapid load energization as more generators are synchronized. Once the individual subsystems have been restored, the regions are synchronized to reassemble the complete grid.

During the generator and load recovery stages, restoration plans describe a sequential set of actions by the system operators, which may include closing breakers to energize a transmission line or signaling for the start-up of an NBSU. Each restorative action perturbs the system and induces transient dynamics that take time to settle; for example, a load pick-up introduces a power imbalance that causes the frequency to decline. Planners should be wary of the dynamic effects of each action, as excessive disturbances may destabilize the system [9]. The smaller and weaker islands during the early stages are particularly susceptible to instability, which can lead to a cascade of failures. Consequently, restoration planning involves a trade-off between speed, which reduces damages associated with the outage, and reliability, which reduces the chance of system failure during restoration.

Recent developments in inverter-based resources (IBRs) present both challenges and opportunities to restoration planning. On the one hand, IBRs can provide black-start services and can be dispatched at a faster rate than SGs [10], [11]. On the other hand, as IBRs replace conventional generation, systems have lowered inertia and are more prone to frequency deviations [12]. Excessive deviations from the nominal 50 or 60 Hz may damage both utility and consumer devices and impede restoration by triggering load-shedding protection systems [12]. Therefore, it is vital that operators are aware of how frequency dynamics develop during the restoration process. The lowest point achieved by the post-disturbance frequency, known as the frequency nadir, is a key indicator of system security [12]. To avoid nadirs that violate the safe frequency limits, operators impose heuristic rules on load pick-ups, such as limiting pick-ups to less than 5% of the active generator capacity [8]. While these rules are designed to ensure stability, they can be too conservative and delay system recovery. Heuristics also provide no insight on the dynamic impact of candidate actions and rely on the operator's judgment. Furthermore, in current restoration plans used by ISOs, IBRs and energy storage systems (ESS) are either excluded from the restoration process [8] or are not considered at all [13], [14], leaving valuable power capacity and dynamic services unused.

In this work, we propose a tool for finding frequency-secure restoration plans for the generator and load recovery phases, with two major improvements over heuristics. By actively considering frequency effects during planning, it ensures frequency security without resorting to overly conservative measures and provides more transparency and insight into how restorative actions impact system frequency.

1.2 Literature Review

In the 1980's, the foundational concepts of power system restoration were laid out by a pair of IEEE task force reports in an attempt to review existing practices, establish common terminology, and exchange strategies [15], [16]. Prior to this work, ISOs formulated restoration plans that are most appropriate for their individual systems. Despite each ISO adopting dif-

ferent strategies, the reports identified common goals and considerations, such as the timing of switching operations, black-start capability, and frequency security. In 1992, a new IEEE Committee report recommended the use of computer-aided approaches to restoration [17]. In this work, restoration planning is identified as a multi-objective combinatorial optimization problem, but limited computational power at the time rendered it prohibitive to solve. Instead, the report favors the use of heuristics-driven expert systems to assist operators in online decision making. This idea is elaborated on in a follow-up report that outlined the relevant constraints and criteria relevant to each phase of black-start restoration that a computer program must consider [18]. Many fundamental ideas are presented, such as avoiding underfrequency violations via small load pick-ups and synchronizing SGs to improve system inertia. During the 1990s, the committee also published multiple reports on specific aspects of restoration, such as those on nuclear plants [19] and protection systems [20]. A complete survey of restoration literature up to the 21st century is presented in [21], and progress in restoration research during 2006-2016 is presented in [22]. In general, developments in optimization approaches, graph theory, and artificial intelligence opened the door to new restoration planning tools both in offline and online settings. Emerging technologies such as IBRs and microgrids present both new opportunities and challenges. Despite these newer methods, ISO documents on power system restoration continue to adhere to heuristic-based guidelines, although the details of how these plans are created are not publicly available.

In this work, we focus on optimization-based restoration planning for transmission systems, which is well established in the literature as restoration involves making decisions based on multiple objectives and subject to operational constraints. Furthermore, optimization frameworks may address one or multiple phases of restoration, and include various levels of modeling detail depending on the objective of the framework. For example, the nonlinear, nonconvex power flow equations is often replaced by an approximate power flow model (more details are provided in Section 1.1) to provide computationally tractable problems.

Assuming that generator recovery has been completed, [23] develops an ordering problem for line and load recovery. The work considers the coordination of dispatching crews for transmission line repair with operator actions such as generator dispatch, introducing constraints on travel time and availability of the crews. This highlights the multifaceted nature of restoration problems and the need for appropriate models to represent real-world scenarios. This concept is also explored in [24], where mobile energy storage systems travel around the network and provide power support during restoration. The power system is overlaid onto a corresponding transportation network where mobile power sources can navigate and be dispatched subject to travel time constraints.

The ordering problem from [23] is extended in [25] to consider the rotor angle stability of each action. The system dynamics are modeled in the optimization problem by discretizing the ODEs that describe them and inserting them as constraints. Interestingly, other system dynamics, such as frequency and voltage, may be similarly introduced by performing the

same discretization on the differential equations that govern them. However, this naive approach scales poorly as the accuracy of discretization depends on the granularity of each discrete time step. Instead, it is preferable to bound the frequency dynamics indirectly by restricting the set of allowable operator actions itself to avoid problems caused by high dimensionality. Another extension of [23] introduces a computationally lighter alternative by solving the ordering problem iteratively [26]. The work shows that by coarsely ordering the set of all available restorative actions and recursively refining the sequence, restoration plans can be found much faster than solving the single large ordering problem at a small cost of optimality.

The sectionalization process is often performed individually to the other restoration phases, but it should ensure that all divided regions can be restored in roughly the same amount of time to prevent certain parts of the system from lagging behind. This idea is taken in [6], where system partitioning decisions are made alongside generator and load recovery actions. This work also presents the NBSU start-up procedure, a key aspect of generator recovery.

The proliferation of renewable energy has also sparked interest in how these resources can participate in power system restoration. The uncertainty of fluctuating wind power is addressed in [27] by chance constraints, while [28] uses a receding time horizon to mitigate the effect of wind uncertainty over a long period. Online restoration planning approaches have also been developed to address uncertainty using real-time measurements. A feedback control approach uses optimization-based controllers to find the next actions in [29]. These works show how renewable resources can be leveraged to accelerate system recovery.

While most works assume that the system returns to a steady state following each action, the load pick-up actions are bounded to prevent excessive frequency drops in [28]. The work formulates this constraint by adopting the frequency dynamics model from [30], which presents a relation between the frequency nadir and an electrical disturbance based on a linear generator response assumption. However, it is unclear how the nonlinear constraint is integrated into the mixed-integer linear framework in [28]. Furthermore, the linear generator response in [30] is not clearly justified, and is assumed to simplify the mathematical analysis. As no explicit model of the governor, the system that controls generators response, is provided, the work recommends selecting a conservative slope for the linear response, which compromises modeling accuracy. This thesis addresses these shortcomings by analyzing the frequency regulating systems, and providing both physical and mathematical justification for our simplifying assumptions. In addition, we describe in detail how frequency constraints can be manipulated and integrated into the restoration framework we construct.

The frequency dynamics following a disturbance is stabilized by the generators in the system and can be described as the output of a nonlinear system. Due to its complexity, the frequency model is often simplified in two ways—by reducing the governor model, or by making mathematical approximations. For instance, a second-order frequency model is

derived in [31] from a simple governor model, and extended in [32] for multi-machine systems and in [33] for a variety of generation types. A common mathematical approximation assumes that the post-disturbance frequency can be described by a linear [34] or quadratic [35] function. These simplified models lead to explicit representations of the post-disturbance frequency behavior at the cost of model accuracy. Importantly, these frequency prediction methods, when applied in the context of restoration, may be inadequate in two aspects. First, expressions for the frequency nadir must be embedded as a constraint in an optimization problem, which may render nonlinear or complex algebraic expressions unusable. Second, these methods address contingency scenarios, which are unforeseen disturbances, while disturbances from restorative actions are deliberately introduced and expected. In this thesis, we demonstrate how this extra knowledge can be used to improve the frequency response of the generators, making the aforementioned methods unideal for this application.

1.3 Contributions and Chapter Overview

The main contributions of this work are as follows. We develop a frequency-constrained black-start restoration planning optimization framework for transmission systems. Given any frequency limit, the optimization problem ensures that all actions in the restoration plan do not violate the limit subject to a small error. First, we present a mixed-integer linear program (MILP) for computing optimal restoration sequences. To incorporate frequency constraints, we analyze the governor-turbine systems of SGs, which control their response to power imbalances. The IEEEG1 governor-turbine model is chosen because it offers a mathematical representation of generator rate limits, which constrain variations in output power, and setpoints, which determine their steady-state output. The setpoints are assigned during normal operation by an economic dispatch problem to minimize the cost of operation [36], and do not normally contribute to frequency response. However, using the known timing and magnitudes of the restorative actions, we leverage generator setpoints to improve the system's frequency behavior. Following this strategy, we develop a closed-form expression of the frequency nadir and reformulate it as a constraint in the MILP, appearing as bounds on the load pick-up and generator start-up decisions. Although the frequency nadir expression is nonlinear in the decision variables, we present an iterative receding-horizon algorithm to predict future system parameters and linearize the constraint. We provide numerical results to validate the frequency nadir prediction method and the frequency-constrained planning program. The final sections of this thesis introduce ESS devices to the frequency-constrained restoration planning problem. We demonstrate their ability to assist in network recovery and frequency response by coordinating setpoint updates with restorative actions. Perhaps counterintuitively, numerical results show that charging ESS during restoration can accelerate load recovery.

This work is divided into two major discussions. Chapter 3 develops a method for

systems with only SGs to find frequency-secure plans. Chapter 4 extends the framework to scenarios where ESS devices actively participate in restoration and frequency response. A brief summary of each chapter is given below.

- Chapter 2 introduces the technical and mathematical background used in this work, including power flow equations, power system frequency dynamics. and mixed-integer programs.
- Chapter 3 introduces the frequency-constrained MILP for restoration planning, and consists of four sections. Section 3.1 develops the MILP for optimal restoration planning, which acts as a foundation for subsequent sections. Section 3.2 introduces the ramp approximation, a method that predicts the frequency nadirs by analyzing the structure of the IEEEG1 governor-turbine and using knowledge of the disturbance sizes. Section 3.3 discusses how frequency nadirs obtained by the ramp approximation can be incorporated into the MILP restoration framework as linear constraints through an iterative algorithm. Section 3.4 provides simulation results from MATLAB and PSS/E on a modified IEEE 9-bus system to show the impact of restorative actions on frequency.
- Chapter 4 introduces ESS to the MILP framework and the frequency nadir prediction method and consists of two sections. Section 4.1 integrates the ESS models into our mathematical analysis, and Section 4.2 provides MATLAB simulation results to show the effects of ESS participation.
- Chapter 5 details extensions to the work that is currently in development as well as avenues for future work. It also provides a brief overview of the strengths and limitations of the work.
- Appendix A derives optimal selections of the big M constants used in mixed-integer constraints.
- Appendix B derives the steady-state PFR outputs in a multi-machine system.
- Appendix C shows that for the ramp approximation, the maximum power imbalance with nonzero damping converges to the expression with zero damping as $D_{\text{sys}} \to 0$.
- Appendix D shows the parameters used in the IEEE modified 9-bus system.
- Appendix E shows the derivation of the maximum safe power imbalance with ESS support and a nonzero damping coefficient.

Chapter 2

Technical Preliminaries

In this chapter, we provide some background on the properties of power systems during steady-state and non-steady-state operation. First, we introduce the power flow equations that relate power transfers to voltages and show, using standard assumptions, some common approximations. Next, we show the frequency dynamics that occur following an electrical disturbance and describe how they are stabilized by the control systems of SGs. Finally, we introduce basic concepts related to mixed-integer programs, a class of optimization problems which restoration problems fall under.

2.1 Power Flow Equations

The network configuration of a balanced three-phase power system in steady state can be represented by the system admittance matrix $\mathbf{Y} \in \mathbb{C}^{B\times B} = \mathbf{G} + j\mathbf{B}$, where B is the number of buses [36]. The admittance matrix relates the complex power transfers through the branches to the complex nodal voltages. Written in real (active) and imaginary (reactive) components, the net power injection of each bus can be defined by the rectangular-form AC power flow (ACPF) equations (2.1) [36]

$$P_i = \sum_{j=1}^{B} V_i V_j (\mathbf{G}_{ij} \cos(\theta_i - \theta_j) + \mathbf{B}_{ij} \sin(\theta_i - \theta_j)) \tag{2.1a}$$

$$Q_i = \sum_{j=1}^{B} V_i V_j (\mathbf{G}_{ij} \sin(\theta_i - \theta_j) - \mathbf{B}_{ij} \cos(\theta_i - \theta_j)) \tag{2.1b}$$

where P_i, Q_i are power injections at bus i, and V_i, θ_i are the voltage magnitude and phase of bus i. In transmission systems, branches usually have much greater reactances than resistances [37]. If we assume that the entries of $\mathbf{G}$ are much smaller than those of $\mathbf{B}$, the

ACPF can be simplified to

$$P_i = \sum_{j=1}^{B} V_i V_j (\mathbf{B}_{ij} \sin(\theta_i - \theta_j))$$
$$Q_i = \sum_{j=1}^{B} V_i V_j (-\mathbf{B}_{ij} \cos(\theta_i - \theta_j))$$

Another common assumption is that the phase differences between buses are small, which physically means that the transmission lines are not heavily loaded [37]. This small-angle approximation uses $\sin(\theta_i - \theta_j) \approx \theta_i - \theta_j$ and $\cos(\theta_i - \theta_j) \approx 1$. This further simplifies the power flow equations to

$$P_i = \sum_{j=1}^{B} V_i V_j \mathbf{B}_{ij} (\theta_i - \theta_j) \tag{2.2a}$$
$$Q_i = -\sum_{j=1}^{B} V_i V_j \mathbf{B}_{ij} \tag{2.2b}$$

The final assumption is that, under normal operating conditions, the voltage magnitudes are close to a value of 1 per-unit. If we assume that any product of bus voltages is approximately 1, the active power expression (2.2a) simplifies to the DC power flow (DCPF) equation [37].

$$P_i = \sum_{j=1}^{B} \mathbf{B}_{ij} (\theta_i - \theta_j) \tag{2.3}$$

Although not considered in DCPF models, the reactive power expression can also be linearized in terms of voltage magnitudes. Defining $\mathbf{b}_{ii}$ as the ith bus shunt reactance, the element $\mathbf{B}_{ii} = \mathbf{b}_{ii} - \sum_{j \neq i}^{B} \mathbf{B}_{ij}$ can be isolated from the sum to re-express (2.2b) as

$$\begin{aligned} Q_i &= -\mathbf{b}_{ii} V_i^2 + \sum_{j \neq i}^{B} \mathbf{B}_{ij} V_i^2 - \sum_{j \neq i}^{B} V_i V_j \mathbf{B}_{ij} \\ &= -\mathbf{b}_{ii} V_i^2 + \sum_{j \neq i}^{B} V_i \mathbf{B}_{ij} (V_i - V_j) \end{aligned}$$

Now applying the unity voltage product assumption, the linearized reactive power flow is

$$Q_i = -\mathbf{b}_{ii} + \sum_{j \neq i}^{B} \mathbf{B}_{ij} (V_i - V_j) \tag{2.4}$$

The first term represents the reactive power consumed or delivered by a shunt inductor or capacitor, respectively. The second term represents reactive line flows that depend on the

bus voltage magnitudes.

2.2 Power System Frequency Dynamics

Power systems operate in steady state at a nominal frequency of 50 or 60 Hz [5]. When a disturbance is introduced, such as a power imbalance or the outage of any network element, the system's frequency undergoes a transient phase determined by active synchronous machines, whose large rotating turbines provide an inertial response driven by the conversion between stored mechanical energy and electrical energy [12]. The regional frequency dynamics are characterized at generator buses by the linearized swing equation [36].

$$\Delta\dot{\omega}_{\text{gen}} = \frac{1}{2H_{\text{gen}}} \left(\Delta P_{\text{m}} - \Delta P_{\text{e}} - D_{\text{gen}}\Delta\omega_{\text{gen}}\right)$$

where $H_{\text{gen}}, D_{\text{gen}}$ are the inertia and damping constants of the generator in the system-base units, ΔP_{m} and ΔP_{e}, both in the system-base power, are the mechanical power supplied by the turbine and the net electrical imbalance experienced at the bus, respectively. The damping constants of synchronous machines D_{gen} are usually small and are neglected. Local frequencies defined by the swing equation at each generator bus are coupled by the power flow equations to form a set of differential-algebraic equations (DAE). In contrast, the average system frequency (ASF) model [38] ignores regional frequency interactions by considering a unified center-of-inertia frequency $\Delta\omega$ defined by the system-wide swing equation

$$\Delta\dot{\omega} = \frac{1}{2H_{\text{sys}}} \left(\Delta P_{\text{m}} - \Delta P_{\text{e}}\right) \tag{2.5}$$

where ΔP_{m} and ΔP_{e} now represent the combined mechanical power output of all generators and the net power imbalance of the system. H_{sys} is a weighted inertia term defined by

$$H_{\text{sys}} = \frac{\sum_{i\in\mathcal{G}_{\text{s}}} H_i \overline{S_{\text{g}}}^{i}}{S_{\text{sys}}} \tag{2.6}$$

where $\mathcal{G}_{\text{s}}$ is the set of indices corresponding to the synchronized units in the system, H_i and $\overline{S_{\text{g}}}^{i}$ are the inertia constant and maximum power capacity of the ith unit, respectively, and S_{sys} is the system-base power. When a power shortage, represented by $\Delta P_{\text{e}} > 0$, is introduced, the frequency begins to decline at a rate proportional to the inertia constant. To arrest the decreasing frequency, a closed-loop feedback mechanism known as primary frequency response (PFR) adjusts the output of active generators to increase the ΔP_{m} term [36]. The specific behavior of the PFR depends on the governors and turbines that control the generator responses. PFR is primarily responsible for frequency stabilization, and secondary frequency response, which acts on a longer time scale (30 s-30 min), brings the frequency back to its nominal value [36]. The phases of frequency recovery following a step imbalance are shown in Fig. 2.1. The lowest point, or point of maximum deviation,

termed the frequency nadir, is a significant indicator of system security. The nadir can be used to assess whether the post-disturbance frequency will violate any safe thresholds.

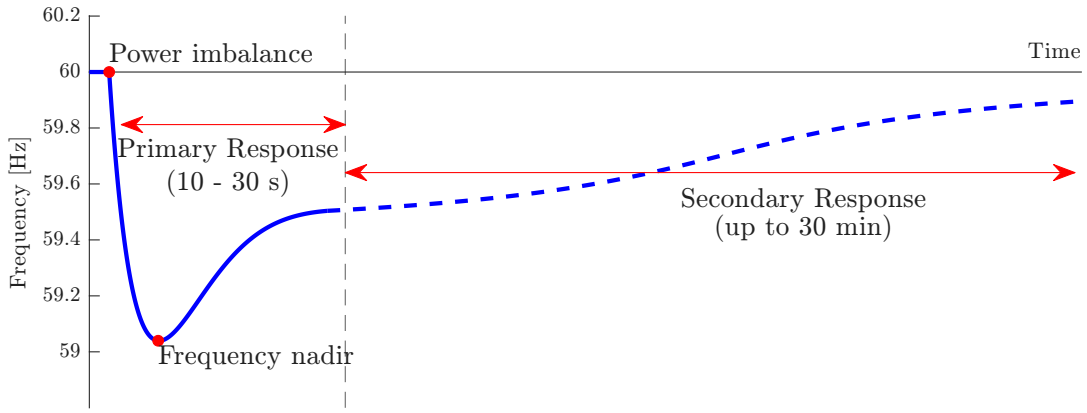

Figure 2.1: Frequency response following a disturbance

Since PFR is often provided by multiple units simultaneously, we modify the swing equation (2.5) to explicitly show ΔP_{m} as the combined contribution of the set of active PFR-providing generators, notated by $\mathcal{G}_{\mathrm{po}}$.

$$\Delta\dot{\omega} = \frac{1}{2H_{\mathrm{sys}}}\left(\sum_{i\in\mathcal{G}_{\mathrm{po}}} \alpha^i \Delta P_{\mathrm{m}}^i - \Delta P_{\mathrm{e}}\right) \tag{2.7}$$

with the power conversion factors α^i that convert ΔP_{m}^i, the output of each generator in their own base units, to the system-base units.

$$\alpha^i = \frac{S_{\mathrm{g}}^i}{S_{\mathrm{sys}}} \tag{2.8}$$

2.3 Mixed-Integer Programs

The general nonlinear mixed-integer program is an optimization problem with both continuous and integer decision variables.

$$\begin{aligned} \min_{x,y} \quad & f(x,y) \\ \text{s.t.} \quad & g(x,y) \leq 0 \\ & h(x,y) = 0 \\ x \in \mathbb{R}^n \quad & y \in \mathbb{Z}^m \end{aligned}$$

The main approach to solving mixed-integer problems is the branch-and-bound algorithm. By relaxing the integer variables into continuous variables and solving the simpler continuous problem, the algorithm creates optimality bounds and adds constraints to eliminate integer

infeasible solutions, iterating the process similarly to a tree search algorithm [39]. Importantly, this means that if the underlying integer-relaxed problem can be solved with efficient algorithms, solving the mixed-integer variant is much easier. Many classes of mixed-integer problems exist, such as the mixed-integer linear program (MILP), mixed-integer quadratic program (MIQP), and mixed-integer convex programs (MICP). In this work, we construct an MILP framework for black-start restoration, which takes on the form

$$\begin{aligned} \min_{x,y} \quad & c_x^\top x + c_y^\top y \\ \text{s.t.} \quad & Ax + By \leq 0 \\ & Cx + Dy = 0 \\ x \in \mathbb{R}^n \quad & y \in \mathbb{Z}^m \end{aligned}$$

where $c_x \in \mathbb{R}^n, c_y \in \mathbb{R}^m$ are cost vectors and A, B, C, D are matrices of appropriate sizes depending on the number of constraints. The important property is that the objective function and all constraints contain only linear terms of the variables. The underlying linear program can be solved efficiently using the simplex method [40], which allows MILPs to be solved efficiently using branching methods.

Chapter 3

Frequency-constrained MILP for Restoration Planning

Here, we synthesize the optimization-based restoration planning tool. This chapter is divided into several sections. Section 3.1 introduces the MILP model of the restoration planning problem without frequency constraints, Section 3.2 examines the system's frequency dynamics following restorative actions, deriving a relation between the frequency nadir and the magnitude of power imbalances. Section 3.3 shows how the relation can be enbedded within the MILP as a linear constraint by adopting an iterative planning algorithm. Finally, we show using a case study the effectiveness of the frequency nadir prediction method and frequency-constrained sequences in Section 3.4.

3.1 MILP Restoration Framework

This section presents the basic MILP formulation of the transmission-level black-start restoration problem. The framework in this thesis is inspired by the formulations in [27] and [6], with variations on the network constraints. We focus on the generator and load recovery phases and assume that the greater grid has been partitioned into subsystems for parallel recovery. As such, the MILP seeks an optimal sequence of actions to fully restore the subsystem in a minimum amount of time. To provide a practical plan, the problem must consider the physical characteristics and logical couplings of the network components. Subsequent sections will build on this framework by introducing additional considerations, such as safe frequency limits and ESS participation.

We consider a conventional system with synchronous machines as the sole supply of power and adopt the DC power flow model. The loads at each substation are usually defined by a single lump sum of demand. However, loads can be switched on at a finer scale, that is, the distribution feeders at a substation can be connected individually [41]. As such, the loads on each bus are split into their smallest discrete denominations.

3.1.1 Binary Status Constraints

Binary variables are used to model the on and off statuses of network elements. We consider a power system with B buses, L lines, D loads (demand) and G generators, and let $\boldsymbol{b}_\mathrm{b} \in \{0,1\}^{B\times T}$, $\boldsymbol{b}_\mathrm{l} \in \{0,1\}^{L\times T}$, $\boldsymbol{b}_\mathrm{d} \in \{0,1\}^{D\times T}$, $\boldsymbol{b}_\mathrm{g} \in \{0,1\}^{G\times T}$ denote matrices of binary variables that indicate the on/off status of the respective components over T discrete time steps.

$$\begin{aligned}
\boldsymbol{b}_\mathrm{b} &= \begin{bmatrix} \boldsymbol{b}_\mathrm{b}(1) & \boldsymbol{b}_\mathrm{b}(2) & \cdots & \boldsymbol{b}_\mathrm{b}(T) \end{bmatrix} \\
\boldsymbol{b}_\mathrm{l} &= \begin{bmatrix} \boldsymbol{b}_\mathrm{l}(1) & \boldsymbol{b}_\mathrm{l}(2) & \cdots & \boldsymbol{b}_\mathrm{l}(T) \end{bmatrix} \\
\boldsymbol{b}_\mathrm{d} &= \begin{bmatrix} \boldsymbol{b}_\mathrm{d}(1) & \boldsymbol{b}_\mathrm{d}(2) & \cdots & \boldsymbol{b}_\mathrm{d}(T) \end{bmatrix} \\
\boldsymbol{b}_\mathrm{g} &= \begin{bmatrix} \boldsymbol{b}_\mathrm{g}(1) & \boldsymbol{b}_\mathrm{g}(2) & \cdots & \boldsymbol{b}_\mathrm{g}(T) \end{bmatrix}
\end{aligned}$$

We use the notation $\boldsymbol{b}(k)$ for the kth column of matrix $\boldsymbol{b}$, and $\boldsymbol{b}^i$ for the ith row of $\boldsymbol{b}$. Between each time step $k \in \{1,\dots,T\}$, some fixed length of time t, in minutes, passes. In other words, restorative actions that alter the system state are taken every t minutes. The time between each step allows the transient dynamics to settle prior to the next action. The restoration time period T indicates the number of time steps in the problem and defines the length of the output restoration sequence. Its value should be chosen so that the system is fully restored at the end. Since the number of required actions depends on the size of the system and is unknown in advance, we introduce an iterative algorithm in Section 3.1.7 that ends when restoration is completed to circumvent the need to select T. The time between steps t is chosen by the operators to allow the transient dynamics to settle after each action, and is typically one to several minutes long. A uniform step size is used for mathematical simplicity, but in practice the period between actions can be decided by operators based on the state of the system.

We define, as notation, the stacked binary status matrix $\boldsymbol{b} = \mathsf{col}(\boldsymbol{b}_\mathrm{b}, \boldsymbol{b}_\mathrm{l}, \boldsymbol{b}_\mathrm{d}, \boldsymbol{b}_\mathrm{g})$. Changes in binary variables between any time steps represent system-altering actions that make up the overall restoration plan. Therefore, the optimal restoration plan can be recovered from the status matrix $\boldsymbol{b}$ alone. The initial statuses of the network elements prior to restoration are denoted by $\boldsymbol{b}_{\mathrm{b},0} \in \{0,1\}^B$, $\boldsymbol{b}_{\mathrm{l},0} \in \{0,1\}^L$, $\boldsymbol{b}_{\mathrm{d},0} \in \{0,1\}^D$, and $\boldsymbol{b}_{\mathrm{g},0} \in \{0,1\}^G$. With slight abuse of notation, these vectors will also be represented by $\boldsymbol{b}_\mathrm{b}(0)$, $\boldsymbol{b}_\mathrm{l}(0)$, $\boldsymbol{b}_\mathrm{d}(0)$, $\boldsymbol{b}_\mathrm{g}(0)$ respectively since they represent statuses at the zeroth time step. The corresponding stacked initial status vector $\boldsymbol{b}_0$, notated interchangeably as $\boldsymbol{b}(0)$, can be formed as

$$\boldsymbol{b}_0 = \mathsf{col}(\boldsymbol{b}_{\mathrm{b},0}, \boldsymbol{b}_{\mathrm{l},0}, \boldsymbol{b}_{\mathrm{d},0}, \boldsymbol{b}_{\mathrm{g},0}) = \boldsymbol{b}(0)$$

Without loss of generality, we let generator 1, the lone BSU in the system reside on bus 1. In a black-start scenario, the focus of this work, only the BSU and the bus that it resides

on are initially active. That is,

$$\forall i \in \{1, \ldots, G\}, \qquad \boldsymbol{b}_{\mathrm{g}}^{i}(0) = \begin{cases} 1 & i = 1 \\ 0 & i \neq 1 \end{cases}$$

$$\forall i \in \{1, \ldots, B\}, \qquad \boldsymbol{b}_{\mathrm{b}}^{i}(0) = \begin{cases} 1 & i = 1 \\ 0 & i \neq 1 \end{cases}$$

We impose that no network elements may be disconnected once they have been restored, as this goes against the high-level goals of restoration. This can be enforced through an element-wise linear inequality in binary variables,

$$\boldsymbol{b}(k) - \boldsymbol{b}(k-1) \geq \mathbb{0} \qquad \forall k \in \{1, \ldots, T\} \tag{3.1}$$

where $\mathbb{0}$ is the zeros vector of appropriate length. We also impose that at most one of each element type can be turned on at any time step. For example, turning on two lines at the same step is forbidden, but turning on a line and a bus together is allowed. This forces the plan to be a sequence of actions with a clear order of events, rather than sets of simultaneous actions. In mathematical terms, this means that for all $k \in \{1, \ldots, T\}$,

$$\mathbb{1}^{\top}(\boldsymbol{b}(k) - \boldsymbol{b}(k-1)) \leq 1 \tag{3.2}$$

where $\mathbb{1}$ is the ones vector of appropriate length. We will also use $\mathbb{1}_{n \times m}$ to denote a n by m matrix of all ones.

3.1.2 Power Flow Logic

The DCPF equation given in (2.3) is defined for systems with a fixed network configuration. During restoration, buses and lines may be energized and loads and generators may be picked up. To account for network changes, the binary status variables are integrated into the DCPF equations. First, we introduce element-to-bus adjacency matrices $\mathbf{A}_{\mathrm{l}} \in \{0,1\}^{B \times L}$, $\mathbf{A}_{\mathrm{d}} \in \{0,1\}^{B \times D}$, $\mathbf{A}_{\mathrm{g}} \in \{0,1\}^{B \times G}$ that map lines, demand (load), and generators to their bus, respectively.

$$\mathbf{A}_{n,ij} = \begin{cases} 1 & j\text{th element of } n \text{ is connected to bus } i \\ 0 & \text{otherwise.} \end{cases} \tag{3.3}$$

Let $\boldsymbol{P}_{\mathrm{d}} \in \mathbb{R}^{D}$ be the vector of magnitudes of the static active power load to be restored. Each of its entries represents an indivisible unit of load, multiple of which can reside on the same bus. The continuous variables $\boldsymbol{P}_{\mathrm{l}} \in \mathbb{R}^{L \times T}$ and $\boldsymbol{P}_{\mathrm{g}} \in \mathbb{R}^{G \times T}$ represent the active power

line flows and generator outputs at all time steps.

$$\boldsymbol{P}_{\mathrm{l}} = \begin{bmatrix} \boldsymbol{P}_{\mathrm{l}}(1) & \boldsymbol{P}_{\mathrm{l}}(2) & \dots & \boldsymbol{P}_{\mathrm{l}}(T) \end{bmatrix}$$
$$\boldsymbol{P}_{\mathrm{g}} = \begin{bmatrix} \boldsymbol{P}_{\mathrm{g}}(1) & \boldsymbol{P}_{\mathrm{g}}(2) & \dots & \boldsymbol{P}_{\mathrm{g}}(T) \end{bmatrix}$$

The vectorized active power balance equation at every bus and every time step can be compactly written as

$$\mathbf{A}_{\mathrm{g}}\boldsymbol{P}_{\mathrm{g}} - \mathbf{A}_{\mathrm{d}}\,\mathrm{diag}(\boldsymbol{P}_{\mathrm{d}})\boldsymbol{b}_{\mathrm{d}} = \mathbf{A}\boldsymbol{P}_{\mathrm{l}} \tag{3.4}$$

where $\mathbf{A} \in \mathbb{R}^{B\times L}$ is the network incidence matrix [42] given by

$$\mathbf{A}_{ij} = \begin{cases} +1, & \text{bus } i \text{ is the from-bus of line } j, \\ -1, & \text{bus } i \text{ is the to-bus of line } j, \\ 0, & \text{otherwise.} \end{cases}$$

where from and to buses are the sending and receiving ends of power through the line, respectively. The behaviors of $\boldsymbol{P}_{\mathrm{l}}$ and $\boldsymbol{P}_{\mathrm{g}}$ will be defined later. Let the phase angles at each bus be captured by $\boldsymbol{\theta} \in \mathbb{R}^{B\times T}$.

$$\boldsymbol{\theta} = \begin{bmatrix} \boldsymbol{\theta}(1) & \boldsymbol{\theta}(2) & \dots & \boldsymbol{\theta}(T) \end{bmatrix}$$

The phase angle at the slack bus, chosen to be the initially online BSU bus, is zero at all times.

$$\boldsymbol{\theta}^1(k) = 0 \qquad \forall k \in \{0, \dots, T\} \tag{3.5}$$

Voltage phase angles are undefined on inactive buses and are set to zero in this work. This can be modeled using the *big M* method, which uses a large constant to enforce logical conditions [43].

$$-M_1\boldsymbol{b}_{\mathrm{b}} \le \boldsymbol{\theta} \le M_1\boldsymbol{b}_{\mathrm{b}} \tag{3.6}$$

The phase angles at offline buses are set to zero as both their upper and lower bounds become zero in (3.6). For online buses, the large M_1 constant loosens the constraint to allow nonzero phase angles. The M constants are chosen to be larger than the expressions they bound, but not arbitrarily large, as this will cause numerical problems in mixed-integer solvers [43]. As notation, we use M_i to denote appropriately large constants in big M inequalities in the remainder of this work. The optimal selections of M constants are presented in Appendix A.

The DCPF defines active line flows as functions of the bus phases. However, we want the DCPF to be enforced only for energized lines and the flow through de-energized lines to

be zero. That is, for all $i \in \{1, \dots, L\}$ and $k \in \{1, \dots, T\}$

$$\boldsymbol{P}_{\mathrm{l}}^{i}(k) = \begin{cases} X_i^{-1}\mathbf{A}(i)^{\top}\boldsymbol{\theta}(k) & \boldsymbol{b}_{\mathrm{l}}^{i}(k) = 1 \\ 0 & \boldsymbol{b}_{\mathrm{l}}^{i}(k) = 0 \end{cases} \tag{3.7}$$

where X_i is the reactance of line i and $\mathbf{A}(i)$ is the ith column of $\mathbf{A}$. One candidate approach to enforcing (3.7) is $\boldsymbol{P}_{\mathrm{l}}^{i}(k) = \boldsymbol{b}_{\mathrm{l}}^{i}(k)X_i^{-1}\mathbf{A}(i)^{\top}\boldsymbol{\theta}(k)$, but the constraint becomes nonlinear due to the cross product of binary and continuous variables. Instead, the big M method can be used to address each line status case.

$$-M_2(\mathbb{1}_{L\times T} - \boldsymbol{b}_{\mathrm{l}}) \leq \boldsymbol{P}_{\mathrm{l}} - \mathbf{X}^{-1}\mathbf{A}^{\top}\boldsymbol{\theta} \leq M_2(\mathbb{1}_{L\times T} - \boldsymbol{b}_{\mathrm{l}}) \tag{3.8a}$$

$$-M_3\boldsymbol{b}_{\mathrm{l}} \leq \boldsymbol{P}_{\mathrm{l}} \leq M_3\boldsymbol{b}_{\mathrm{l}} \tag{3.8b}$$

where $\mathbf{X} \in \mathbb{R}^{L\times L}$ is the diagonal matrix of line reactances. Active power flows across energized lines are defined by (3.8a), while de-energized lines have zero power flow set by (3.8b).

3.1.3 Network Logic Constraints

The statuses of network elements must be linked by logical constraints in order to produce a sensible restoration plan. The graph structure of a power system network enforces some inherent conditions that must be followed when recovering the system.

In a valid system state, the from and to buses of an energized line must also be energized. This condition can be described mathematically through a linear constraint.

$$\mathbf{A}_{\mathrm{l}}(i)^{\top} \cdot \boldsymbol{b}_{\mathrm{l}}^{i} \leq \boldsymbol{b}_{\mathrm{b}} \qquad \forall i \in \{1, \dots, L\} \tag{3.9}$$

where $\mathbf{A}_{\mathrm{l}}(i) \in \{0, 1\}^B$ denotes the ith column of $\mathbf{A}_{\mathrm{l}}$, which contains two nonzero entries corresponding to the to and from buses of line i. The left-hand side of (3.9) indicates which buses must be online due to the status of the ith line. Conversely, if a bus is isolated, that is, not connected to any energized lines, then it must remain offline until an adjacent line is energized. The exception to this rule are the buses that are initially online, such as the BSU bus.

$$\mathbf{A}_{\mathrm{l}}\boldsymbol{b}_{\mathrm{l}} \geq \boldsymbol{b}_{\mathrm{b}} - \boldsymbol{b}_{\mathrm{b}}(0)\mathbb{1}^{\top} \tag{3.10}$$

The left hand side of (3.10) checks whether each bus has any adjacent active lines, and sets the bus status to zero if there is none. The initial status term $\boldsymbol{b}_{\mathrm{b}}(0)$ makes an exception for the BSU bus, which is online from the beginning. The final line-to-bus logical constraint states that any line may be energized only if one of its adjacent buses has already been restored. This condition prevents lines that are connected to offline buses to be "restored" but remain de-energized. In other words, at least one of the adjacent buses must already be

active for a line to be energized. That is, for all $k \in \{1, \ldots, T\}$.

$$\mathbf{A}_{\mathrm{l}}^{\top} \boldsymbol{b}_{\mathrm{b}}(k-1) \geq \boldsymbol{b}_{\mathrm{l}}(k) \tag{3.11}$$

Since loads and generators reside on buses, it follows that they can be turned on only after their buses have been turned on. A load can be energized on the same step as its bus. Since generator start-up involves time-sensitive phases (more details in the next section), we allow them to turn on at least one step after its bus has been energized.

$$\mathbf{A}_{\mathrm{d}} \boldsymbol{b}_{\mathrm{d}} \leq M_4 \boldsymbol{b}_{\mathrm{b}} \tag{3.12a}$$

$$\mathbf{A}_{\mathrm{g}} \boldsymbol{b}_{\mathrm{g}}(k+1) \leq M_5 \boldsymbol{b}_{\mathrm{b}}(k) \qquad \forall k \in \{0, \ldots, T-1\} \tag{3.12b}$$

3.1.4 Non-Black-Start Units Start-up Process

The active power output of generator i, $\boldsymbol{P}_{\mathrm{g}}^{i}$, is determined by its status. The NBSU start-up process can be described by the four phases shown in Fig. 3.1 [6]. Initially offline, the NBSU enters the cranking phase upon receiving the starting signal and consumes cranking power $\boldsymbol{P}_{\mathrm{c}}^{i}$ over a period $\boldsymbol{T}_{\mathrm{c}}^{i}$. Next, the NBSU enters the ramping phase, when its output increases linearly from zero to a minimum output $\underline{\boldsymbol{P}_{\mathrm{g}}^{i}}$. The ramp time $\boldsymbol{T}_{\mathrm{r}}^{i}$ determines the length of the period and the ramping slope. When the ramping phase is completed, the NBSU is fully activated and produces power within an operating range $[\overline{\boldsymbol{P}_{\mathrm{g}}^{i}}, \underline{\boldsymbol{P}_{\mathrm{g}}^{i}}]$. The aforementioned start-up parameters are defined for all generators and are vectors of size $\mathbb{R}^{G}$, with superscript i indicating the parameter of the ith unit.

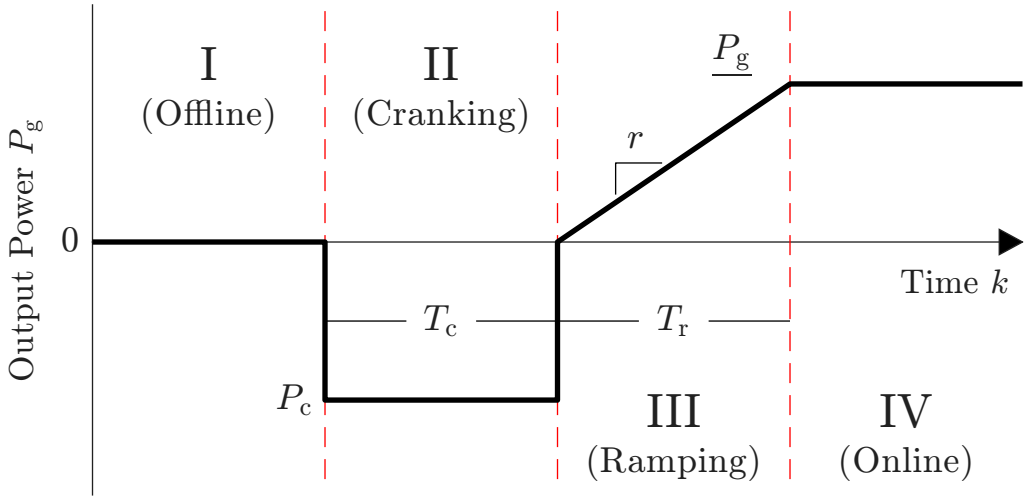

Figure 3.1: Four phases of NBSU start-up (Not to scale)

We introduce auxiliary binary variables $\boldsymbol{b}_{\mathrm{gc}}, \boldsymbol{b}_{\mathrm{gr}}, \boldsymbol{b}_{\mathrm{go}} \in \mathbb{R}^{G \times T}$, which indicate when the generators are cranking, ramping, or online, respectively. These variables depend solely on the variable $\boldsymbol{b}_{\mathrm{g}}$ as the cranking and ramping phases have known lengths. Consider a one-

machine example where $T_\mathrm{c} = 2$ and the generator is given the start-up signal on $k = 3$. The values of b_g and b_gc are shown in Table 3.1.

k	1	2	3	4	5	6	7
$b_\mathrm{g}(k)$	0	0	1	1	1	1	1
$b_\mathrm{gc}(k)$	0	0	1	1	0	0	0

Table 3.1: Example values of binary variable b_gc

In this example, b_gc can be defined by the difference equations

$$\begin{aligned} b_\mathrm{gc}(1) &= b_\mathrm{g}(1) \\ b_\mathrm{gc}(2) &= b_\mathrm{g}(2) \\ b_\mathrm{gc}(3) &= b_\mathrm{g}(3) - b_\mathrm{g}(1) \\ b_\mathrm{gc}(k) &= b_\mathrm{g}(k) - b_\mathrm{g}(k - T_\mathrm{c}) \end{aligned}$$

where a negative argument of the binary variable ($b_\mathrm{g}(k), \quad k < 0$) represents the binary status of the generator k steps *before* the initial network condition. Since the auxiliary variable turns on a fixed time after the start-up signal is received, it depends on the statuses from past time steps. In a black-start scenario, $b_\mathrm{g}(k) = 0 \quad \forall k < 0$ since all NBSUs are initially offline. Each NBSU has different cranking times, so the binary matrix $\boldsymbol{b}_\mathrm{gr}$ can be defined element-wise as

$$\boldsymbol{b}^i_\mathrm{gc}(k) = \boldsymbol{b}^i_\mathrm{g}(k) - \boldsymbol{b}^i_\mathrm{g}(k - \boldsymbol{T}^i_\mathrm{c}) \qquad \forall k \in \{1, \ldots, T\} \quad \forall i \in \{1, \ldots, G\} \tag{3.13}$$

where $k - \boldsymbol{T}^i_\mathrm{c}$ can be negative and refer to steps prior to the start of restoration. The same process can be applied to the ramping variable $\boldsymbol{b}_\mathrm{gr}$ to obtain the relationship

$$\boldsymbol{b}^i_\mathrm{gr}(k) = \boldsymbol{b}^i_\mathrm{g}(k - \boldsymbol{T}^i_c) - \boldsymbol{b}^i_\mathrm{g}(k - \boldsymbol{T}^i_\mathrm{c} - \boldsymbol{T}^i_\mathrm{r}) \qquad \forall k \in \{1, \ldots, T\} \quad \forall i \in \{1, \ldots, G\} \tag{3.14}$$

with similar definitions for the negative indices of the binary variables. Finally, the online indicator $\boldsymbol{b}_\mathrm{go}$ can be defined simply as a complement of the other two auxiliary variables.

$$\boldsymbol{b}_\mathrm{go} = \boldsymbol{b}_\mathrm{g} - \boldsymbol{b}_\mathrm{gc} - \boldsymbol{b}_\mathrm{gr} \tag{3.15}$$

To demonstrate the formulation of linear constraints that describe this piecewise behavior, we first skip the ramping phase and construct a model that only considers phases I, II, and IV. This model is equivalent to having $T_\mathrm{r} = 0$, and $\boldsymbol{P}_\mathrm{g}$ can be described by

$$-M\boldsymbol{b}_\mathrm{gc} + \mathrm{diag}(\underline{\boldsymbol{P}_\mathrm{g}})\boldsymbol{b}_\mathrm{g} \leq \boldsymbol{P}_\mathrm{g} \leq \mathrm{diag}(\overline{\boldsymbol{P}_\mathrm{g}})\boldsymbol{b}_\mathrm{g} + M\boldsymbol{b}_\mathrm{gc} \tag{3.16a}$$

$$-M(\mathbb{1}_{G\times T} - \boldsymbol{b}_\mathrm{gc}) \leq \boldsymbol{P}_\mathrm{g} + \boldsymbol{P}_\mathrm{c} \leq M(\mathbb{1}_{G\times T} - \boldsymbol{b}_\mathrm{gc}) \tag{3.16b}$$

The big M constants are used to associate the output powers $\boldsymbol{P}_{\mathrm{g}}$ with the auxiliary binary variables for each phase of NBSU start-up. When the generator is cranking, (3.16a) is loosened and (3.16b) becomes an equality constraint. When the generator is online, (3.16b) is loosened and (3.16a) becomes a box constraint on the output power. Table 3.2 shows the logic between the binary variables and the generator output.

$b_{\mathrm{g}}(k)$	$b_{\mathrm{gc}}(k)$	$P_{\mathrm{g}}(k)$
0	0	$P_{\mathrm{g}}(k) = 0$
1	0	$P_{\mathrm{g}}(k) = -P_{\mathrm{c}}$
1	1	$\underline{P_{\mathrm{g}}} \leq P_{\mathrm{g}}(k) \leq \overline{P_{\mathrm{g}}}$
0	1	impossible

Table 3.2: Logic table of crank-step generator start-up model

During the ramping phase, the generator power output increases linearly from 0 to $\underline{\boldsymbol{P}_{\mathrm{g}}}$ at a rate $\boldsymbol{r}$. Let $\boldsymbol{P}_{\mathrm{r}} \in \mathbb{R}^{G\times T}$ be the reference signal that $\boldsymbol{P}_{\mathrm{g}}$ will follow during the ramping period with a slope defined by $\boldsymbol{r}$. The constraints in (3.16) are adjusted to account for the extra ramping phase.

$$-M_6(1-\boldsymbol{b}_{\mathrm{gc}}) \leq \boldsymbol{P}_{\mathrm{g}} + \boldsymbol{P}_{\mathrm{c}} \leq M_6(1-\boldsymbol{b}_{\mathrm{gc}}) \tag{3.17a}$$

$$-M_7(1-\boldsymbol{b}_{\mathrm{gr}}) \leq \boldsymbol{P}_{\mathrm{g}} - \boldsymbol{P}_{\mathrm{r}} \leq M_7(1-\boldsymbol{b}_{\mathrm{gr}}) \tag{3.17b}$$

$$-M_8(\boldsymbol{b}_{\mathrm{gr}}+\boldsymbol{b}_{\mathrm{gc}}) + \mathrm{diag}(\underline{\boldsymbol{P}_{\mathrm{g}}})\boldsymbol{b}_{\mathrm{g}} \leq \boldsymbol{P}_{\mathrm{g}} \leq \mathrm{diag}(\overline{\boldsymbol{P}_{\mathrm{g}}})\boldsymbol{b}_{\mathrm{g}} + M_8(\boldsymbol{b}_{\mathrm{gr}}+\boldsymbol{b}_{\mathrm{gc}}) \tag{3.17c}$$

This set of constraints fully describes the four-stage start-up process of the NBSU. The adjustments from the model without ramping are the introduction of (3.17b), which is only active during the ramping phase, and an additional loosening term in (3.17c). The reference term $\boldsymbol{P}_{\mathrm{r}}$, a function that begins to increase linearly when the ramping phase begins, is only tracked during the ramping phase. We choose to discretize the linear increase in power by the midpoint value of each time step as shown in Fig. 3.2 to best capture the total energy supplied during the ramping process.

The value of $\boldsymbol{P}_{\mathrm{r}}$ at the beginning of the ramping phase is $\frac{1}{2}r$; the next is $\frac{3}{2}r$, and so on, as described by constraints (3.18).

$$-M_9\boldsymbol{b}_{\mathrm{gr}} \leq \boldsymbol{P}_{\mathrm{r}} + \tfrac{1}{2}\boldsymbol{r}\cdot\mathbb{1}^{\top} \leq M_9\boldsymbol{b}_{\mathrm{gr}} \tag{3.18a}$$

$$-M_{10}(1-\boldsymbol{b}_{\mathrm{gr}}(k)) \leq \boldsymbol{P}_{\mathrm{r}}(k) - \boldsymbol{P}_{\mathrm{r}}(k-1) - \boldsymbol{r} \leq M_{10}(1-\boldsymbol{b}_{\mathrm{gr}}(k)) \quad \forall k \in \{1,\ldots,T\} \tag{3.18b}$$

$\boldsymbol{P}_{\mathrm{r}}$ is maintained at $-\frac{1}{2}r$ outside of the ramping phase by (3.18a), but this value does not affect the power outputs as (3.17b) is loose. During the ramping phase, (3.18b) describes the linear increase of the reference term which is tracked by the generator output in (3.17b). The corresponding logic table for the complete four-phase start-up is shown in Table 3.3

During the final phase, generator outputs are bound by their ramp rates, but unlike

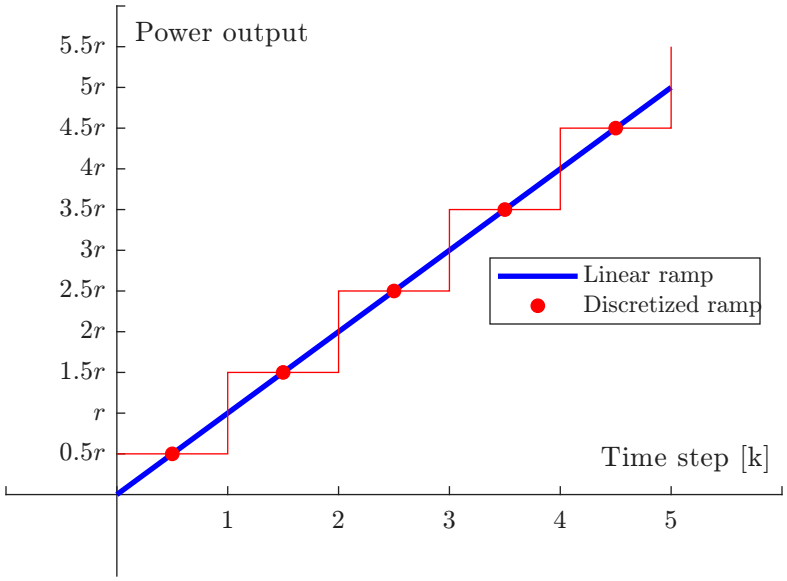

Figure 3.2: Discretized ramping reference function

$b_{\mathrm{g}}(k)$	$b_{\mathrm{gc}}(k)$	$b_{\mathrm{gr}}(k)$	$P_{\mathrm{g}}(k)$
0	0	0	$P_{\mathrm{g}}(k) = 0$
1	1	0	$P_{\mathrm{g}}(k) = -P_{\mathrm{c}}$
1	0	1	$P_{\mathrm{g}}(k) = -P_{\mathrm{r}}(k)$
1	0	0	$\underline{P_{\mathrm{g}}} \leq P_{\mathrm{g}}(k) \leq \overline{P_{\mathrm{g}}}$
All other combinations impossible			

Table 3.3: Logic table of complete NBSU start-up model

during the ramping phase, they are free to decrease and increase within the upper and lower limits. To impose this, we add that for all $k \in \{1, \ldots, T\}$,

$$-\boldsymbol{r} - M_{11}(1 - \boldsymbol{b}_{\mathrm{go}}(k)) \leq \boldsymbol{P}_{\mathrm{g}}(k) - \boldsymbol{P}_{\mathrm{g}}(k-1) \leq M_{11}(1 - \boldsymbol{b}_{\mathrm{go}}(k)) + \boldsymbol{r} \tag{3.19}$$

This constraint is only active for online generators, and allows their power outputs to change by at most $\pm\boldsymbol{r}$.

3.1.5 Objective Function

The overarching goal of restoration is the fast recovery of all network elements. It follows that the objective should contain binary status variables, with weight vectors $\boldsymbol{w}_{\mathrm{g}} \in \mathbb{R}^G$, $\boldsymbol{w}_{\mathrm{d}} \in \mathbb{R}^D$, $\boldsymbol{w}_{\mathrm{l}} \in \mathbb{R}^L$ that specify the degree of priority given to each generator, load, and line. This also allows certain loads, such as critical infrastructure, to be prioritized. The objective function

$$z = \sum_{k=1}^{T} \left[\boldsymbol{b}_{\mathrm{g}}(k)^{\top} \boldsymbol{w}_{\mathrm{g}} + \boldsymbol{b}_{\mathrm{d}}(k)^{\top} \mathrm{diag}(\boldsymbol{P}_{\mathrm{d}}) \boldsymbol{w}_{\mathrm{d}} + \boldsymbol{b}_{\mathrm{l}}(k)^{\top} \boldsymbol{w}_{\mathrm{l}} \right] \tag{3.20}$$

takes into account the statuses of all time steps to incentivize rapid recovery of the grid components. The term $\Delta \boldsymbol{P}_{\mathrm{d}}$ accounts for the sizes of the discrete load packets, so that $\boldsymbol{w}_{\mathrm{d}}$ represents the priority of a MW of load in each packet. Let $w_{\mathrm{d}} \in \boldsymbol{w}_{\mathrm{d}}$, $w_{\mathrm{g}} \in \boldsymbol{w}_{\mathrm{g}}$, $w_{\mathrm{l}} \in \boldsymbol{w}_{\mathrm{l}}$ represent any element in the respective weight vectors. We select the weights to prioritize generator recovery, where in general, $w_{\mathrm{g}} \gg w_{\mathrm{d}} \gg w_{\mathrm{l}}$, for two main reasons. First, the NBSU start-up process takes a substantial amount of time, and an earlier start-up gives access to more power capacity. Second, the weights act as an implicit incentive to increase the system inertia, which otherwise does not directly enter the MILP. These goals align with the guidelines of ISO recovery plans, which similarly advise prioritizing generator start-up, especially during the early stages, to increase the system's active power capability and system inertia [8]. An increased weight can be assigned to priority targets such as critical loads.

3.1.6 Full Optimization Problem Formulation

The complete formulation of the restoration MILP can be written as

$$\max z = \sum_{k=1}^{T} \left[\boldsymbol{b}_{\mathrm{g}}(k)^{\top} \boldsymbol{w}_{\mathrm{g}} + \boldsymbol{b}_{\mathrm{d}}(k)^{\top} \mathrm{diag}(\boldsymbol{P}_{\mathrm{d}}) \boldsymbol{w}_{\mathrm{d}} + \boldsymbol{b}_{\mathrm{l}}(k)^{\top} \boldsymbol{w}_{\mathrm{l}} \right] \tag{3.21}$$

subject to:

⇒Network elements stay on (3.1)

$$\boldsymbol{b}(k) - \boldsymbol{b}(k-1) \geq \mathbb{0} \quad \forall k \in \{1, \ldots, T\}$$

⇒1 element of each type per step (3.2)

$$\mathbb{1}^{\top} (\boldsymbol{b}(k) - \boldsymbol{b}(k-1)) \leq 1 \quad \forall k \in \{0, \ldots, T\}$$

⇒Active power balance (3.4)

$$\mathbf{A}_{\mathrm{g}} \boldsymbol{P}_{\mathrm{g}} - \mathbf{A}_{\mathrm{d}} \, \mathrm{diag}(\boldsymbol{P}_{\mathrm{d}}) \boldsymbol{b}_{\mathrm{d}} = \mathbf{A} \boldsymbol{P}_{\mathrm{l}}$$

⇒Bus voltage phase constraints (3.5), (3.6)

$$\boldsymbol{\theta}^{1}(k) = 0 \quad \forall k \in \{0, \ldots, T\}$$

$$-M_1 \boldsymbol{b}_{\mathrm{b}} \leq \boldsymbol{\theta} \leq M_1 \boldsymbol{b}_{\mathrm{b}}$$

⇒DCPF line flows (3.8)

$$-M_2(\mathbb{1} - \boldsymbol{b}_{\mathrm{l}}) \leq \boldsymbol{P}_{\mathrm{l}} - \mathbf{X}^{-1} \mathbf{A}^{\top} \boldsymbol{\theta} \leq M_2(\mathbb{1} - \boldsymbol{b}_{\mathrm{l}})$$

$$-M_3 \boldsymbol{b}_{\mathrm{l}} \leq \boldsymbol{P}_{\mathrm{l}} \leq M_3 \boldsymbol{b}_{\mathrm{l}}$$

⇒Line to bus logic (3.9), (3.10), (3.11)

$$\mathbf{A}_\mathrm{l}(i)^\top \cdot \boldsymbol{b}_\mathrm{l}^i \leq \boldsymbol{b}_\mathrm{b} \quad \forall i \in \{1,\dots,L\}$$
$$\mathbf{A}_\mathrm{l}\boldsymbol{b}_\mathrm{l} \geq \boldsymbol{b}_\mathrm{b} - \boldsymbol{b}_\mathrm{b}(0)\mathbb{1}^\top$$
$$\mathbf{A}_\mathrm{l}^\top \boldsymbol{b}_\mathrm{b}(k-1) \geq \boldsymbol{b}_\mathrm{l}(k) \quad \forall k \in \{1,\dots,T\}$$

⇒Load and generator to bus logic (3.12), (3.12)

$$\mathbf{A}_\mathrm{d}\boldsymbol{b}_\mathrm{d} \leq M_4\boldsymbol{b}_\mathrm{b}$$
$$\mathbf{A}_\mathrm{g}\boldsymbol{b}_\mathrm{g}(k+1) \leq M_5\boldsymbol{b}_\mathrm{b}(k) \quad \forall k \in \{1,\dots,T-1\}$$

⇒NBSU start-up auxiliary variables (3.13), (3.14), (3.15)

$$\boldsymbol{b}_\mathrm{gc}^i(k) = \boldsymbol{b}_\mathrm{g}^i(k) - \boldsymbol{b}_\mathrm{g}^i(k-\boldsymbol{T}_\mathrm{c}^i) \quad \forall k \in \{1,\dots,T\} \quad \forall i \in \{1,\dots,G\}$$
$$\boldsymbol{b}_\mathrm{gr}^i(k) = \boldsymbol{b}_\mathrm{g}^i(k-\boldsymbol{T}_c^i) - \boldsymbol{b}_\mathrm{g}^i(k-\boldsymbol{T}_\mathrm{c}^i-\boldsymbol{T}_\mathrm{r}^i) \quad \forall k \in \{1,\dots,T\} \quad \forall i \in \{1,\dots,G\}$$
$$\boldsymbol{b}_\mathrm{go} = \boldsymbol{b}_\mathrm{g} - \boldsymbol{b}_\mathrm{gc} - \boldsymbol{b}_\mathrm{gr}$$

⇒NBSU start-up phases (3.17)

$$-M_6(1-\boldsymbol{b}_\mathrm{gc}) \leq \boldsymbol{P}_\mathrm{g} + \boldsymbol{P}_\mathrm{c} \leq M_6(1-\boldsymbol{b}_\mathrm{gc})$$
$$-M_7(1-\boldsymbol{b}_\mathrm{gr}) \leq \boldsymbol{P}_\mathrm{g} - \boldsymbol{P}_\mathrm{gr} \leq M_7(1-\boldsymbol{b}_\mathrm{gr})$$
$$-M_8(\boldsymbol{b}_\mathrm{gr}+\boldsymbol{b}_\mathrm{gc}) + \mathrm{diag}(\underline{\boldsymbol{P}_\mathrm{g}})\boldsymbol{b}_\mathrm{g} \leq \boldsymbol{P}_\mathrm{g} \leq \mathrm{diag}(\overline{\boldsymbol{P}_\mathrm{g}})\boldsymbol{b}_\mathrm{g} + M_8(\boldsymbol{b}_\mathrm{gr}+\boldsymbol{b}_\mathrm{gc})$$

⇒NBSU ramping reference (3.18)

$$-M_9\boldsymbol{b}_\mathrm{gr} \leq \boldsymbol{P}_\mathrm{r} + \frac{1}{2}\boldsymbol{r}\cdot\mathbb{1}^\top \leq M_9\boldsymbol{b}_\mathrm{gr}$$
$$-M_{10}(1-\boldsymbol{b}_\mathrm{gr}(k)) \leq \boldsymbol{P}_\mathrm{r}(k) - \boldsymbol{P}_\mathrm{r}(k-1) - \boldsymbol{r} \leq M_{10}(1-\boldsymbol{b}_\mathrm{gr}(k)) \quad \forall k \in \{1,\dots,T\}$$

⇒Ramp limit in online phase (3.19)

$$-\boldsymbol{r} - M_{11}(1-\boldsymbol{b}_\mathrm{go}(k)) \leq \boldsymbol{P}_\mathrm{g}(k) - \boldsymbol{P}_\mathrm{g}(k-1) \leq M_{11}(1-\boldsymbol{b}_\mathrm{go}(k)) + \boldsymbol{r} \quad \forall k \in \{1,\dots,T\}$$

3.1.7 Iterative Algorithms

Here we motivate the use of suboptimal iterative algorithms to compute restoration plans, which addresses several challenges. First, larger systems with hundreds or thousands of buses require a longer time to fully restore, and the optimization problem may become too complex to solve in a reasonable amount of time. Although restoration planning is performed offline, operators may wish to run the program multiple times to account for different hypothetical scenarios or assess different weights in the objective function, making computational time a relevant concern. Another challenge involves selecting a suitable value for T, as the number of time steps required to fully restore the system is not known a priori. The number of network components to be restored cannot be used to define the restoration time because not all time steps involve recovering exactly one component. An overly long estimate further increases computational burden, while an overly short estimate may lead to an incomplete restoration plan.

In the iterative rolling-horizon algorithm shown in Fig. 3.3, T is instead defined as the

look-ahead period, which is shorter than the entire restoration period. The optimization problem is solved for T steps, after which a subset of the solution is saved and the rest discarded. That is, only the actions of the first t_c steps are added to the plan, where $t_c \leq T$ is termed the control period. Selecting a longer time horizon T improves the optimality of the solution at the cost of increased computational complexity. Algorithm 1 shows the iterative restoration planning framework for any T and t_c.

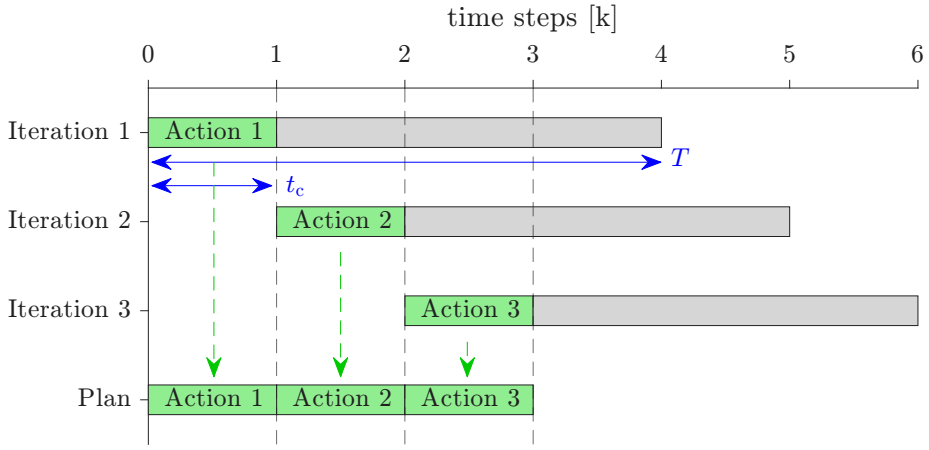

Figure 3.3: Rolling horizon optimization, also known as receding horizon optimization. In each iteration, actions in the control period (green) are added to the plan while the remaining actions (gray) are discarded

Algorithm 1 Iterative Restoration Sequence Computation (IRSC)

Initialize $\boldsymbol{b_0}$
Initialize $\mathsf{plan} = [\boldsymbol{b}_0]$
while $\boldsymbol{b}_0 \neq \mathbb{1}$ **do**
    Solve the MILP in (3.21) for T steps with initial values $\boldsymbol{b}_0$
    Append the plan with actions in the control period: $[\mathsf{plan}] \leftarrow [\mathsf{plan}, \boldsymbol{b}(1:t_c)]$
    Update initialization: $\boldsymbol{b}_0 = \boldsymbol{b}(t_c)$
end while
Output plan

Before the first iteration, the initial statuses of network elements are initialized. The while loop condition checks whether all network elements have been restored. This eliminates the need to estimate the length of the entire restoration sequence. In each iteration, the optimal actions within the control period t, encoded in the binary variables, are appended to the plan. This approach breaks down the full optimization problem into multiple lower-dimension problems that can be solved more efficiently.

Importantly, note that the MILP in (3.21) is no longer solely solving black-start problems. After each iteration, the initial variables are updated and will include more active statuses as the algorithm progresses. Thus, in the definitions of the auxiliary binary variables for cranking (3.13) and ramping (3.14), $\boldsymbol{b}_g(k)$ can have nonzero values for $k < 0$. The generator

statuses prior to the current initial state are stored in the plan variable and are used to construct expressions of $\boldsymbol{b}_{\mathrm{gc}}$ and $\boldsymbol{b}_{\mathrm{gr}}$.

The control period is often chosen as the immediate next time step ($t_{\mathrm{c}} = 1$) as the predictive accuracy of the solution decreases further into the future. The solutions approaching the end of the time horizon are especially poor, as the time steps that follow are not being considered by the optimization program. In an extreme example, the greedy algorithm takes a time horizon of a single step and is unsuitable for restoration as it does not see future rewards. For example, loads may be picked up instead of reserving capacity for NBSU start-up, which may provide more long-term benefit. Longer look-ahead horizons allow future steps to be correctly assessed. By discarding the solutions beyond the control period, the algorithm avoids taking actions that were computed without a proper evaluation of future steps. For the remainder of this work, we adopt a receding horizon approach with $t_{\mathrm{c}} = 1$ and $T > 1$.

Another crucial benefit of Algorithm 1 is its ability to update the system parameters in between each iteration. These system parameters may depend nonlinearly on current or future actions and cannot be incorporated in the MILP framework otherwise. One example of such a parameter is the system's inertia, which depends on the set of synchronized generators. A detailed discussion of parameter updates in between iterations is presented in Section 3.3.

3.2 Frequency Nadir Estimation

In this section, we use the ASF model to predict the frequency nadir caused by step electrical disturbances. The predictions are used to construct constraints on the maximum allowable electrical disturbance at any time step, which can be seamlessly introduced into the MILP to obtain frequency-secure restoration plans. Electrical imbalances are primarily caused by load pick-ups and generator cranking during restoration, so we focus on power shortage scenarios with a declining frequency.

First, we introduce the governor-turbine model that provides the PFR and analyze its structure. We show that coordinating generator setpoint adjustments with restorative actions can accelerate the system's frequency response. Furthermore, an appropriate assignment of setpoints leads to a closed-form approximate mathematical relation between the nadir and the magnitude of the disturbance that caused it. We first demonstrate the approximation on a system with a single machine providing PFR, and generalize the results to PFR contributed by multiple machines and systems with nonzero damping coefficients.

3.2.1 IEEEG1 Governor-Turbine Model and Ramp approximation

The frequency swing equation given by the ASF model was introduced in Section 2.2 by (2.5). A load pick-up introduces a net power shortage that causes a frequency decline. In response, the governors of the synchronous machines that participate in PFR send a signal

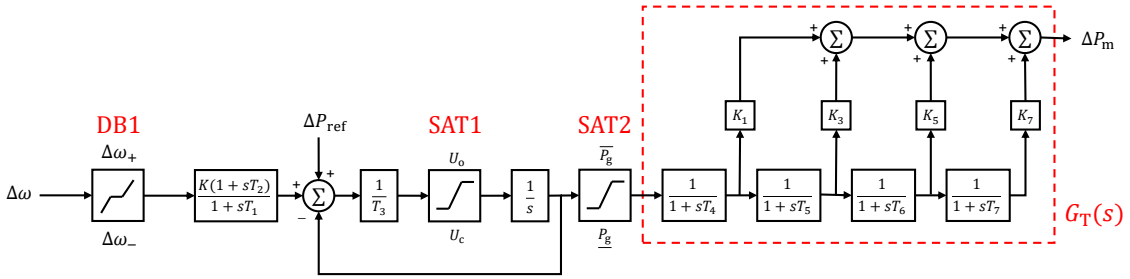

Figure 3.4: IEEEG1 turbine governor diagram

to increase the fuel infeed of the turbines and their power output [36]. Many governor-turbine models have been constructed with various levels of detail. This work will focus on the IEEEG1 governor-turbine model for steam turbines, although its analysis can be applied to other models with similar rate-limiting attributes. The IEEEG1 model, shown in Fig. 3.4, consists of a nonlinear governor that detects the frequency deviation and sends a power signal to the turbine [44]. The deadband block filters out noise to prevent small deviations from triggering PFR. The droop constant K determines the proportion between the frequency deviation and the increase in power. The change in reference power ΔP_{ref}, also termed the power setpoint, is determined by economic dispatch during normal operation and governs the steady-state output [36]. Two saturation blocks limit the rate of change and the magnitude of the PFR power. Physically, SAT1 limits the maximum speed at which the steam valves can be adjusted, and SAT2 limits the valve position. Importantly, note that the limits of SAT1 represent how quickly the generator can ramp up, and U_{o} is equivalent to the ramp rate r when converted to the same units. Finally, the turbine model is linear and is composed of cascading low-pass filters, with time constants $T_1, \ldots, T_7 \in \mathbb{R}_+$. All parameters and signals in the IEEEG1 model are in the per unit base of the generators. The model was selected for its explicit representation of rate limits and power setpoints, which simplified and linear governor-turbine models ignore.

To analyze the frequency response behavior of the IEEEG1 model to step power imbalances, some simplifications are first made. The deadband block can be neglected when studying scenarios where the frequency deviation is large enough to activate PFR. Furthermore, we observe that SAT2 is activated only when a generator reaches its maximum capacity during PFR. By adequately allocating the dynamic reserves of the generators that give PFR, SAT2 can be neglected. The simplified model is shown in Fig. 3.5.

The closed-loop feedback system with multiple synchronous generators is shown in Fig. 3.6. It is assumed that the system dynamics from previous actions have settled prior to the next action. Thus, the signals in 3.6 are given by their deviations from their steady-state values—for example, $\Delta\omega$ represents the frequency deviation from its nominal value and ΔP_{e} represents the change in power demand from the previous steady state. When multiple

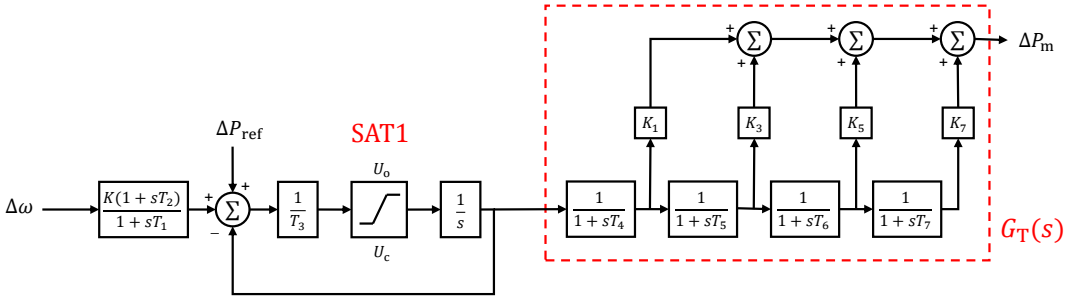

Figure 3.5: Simplified IEEEG1 turbine governor model

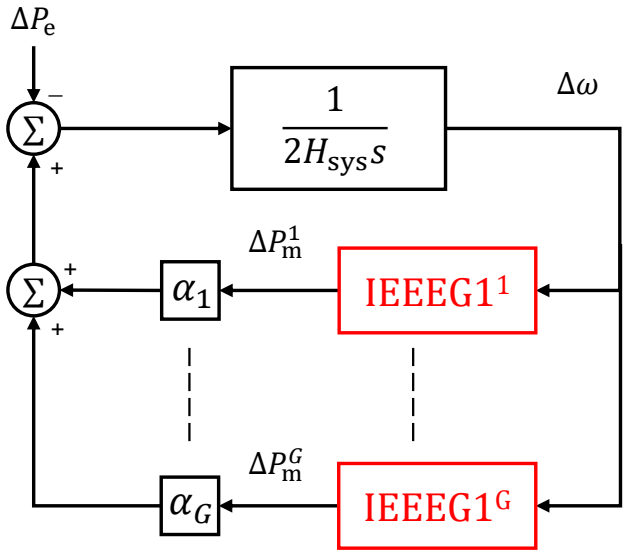

Figure 3.6: Closed-loop feedback of power system frequency with PFR

generators are participating in PFR, each generator carries a share of the power imbalance. After the dynamics settle, each generator's steady state power contribution is determined by their capacities $\overline{\boldsymbol{P}_{\mathrm{g}}}$ and droop coefficients K, as defined in (3.22). See Appendix B for the derivation.

$$\Delta P_{\mathrm{m}}^{i} = \frac{K_i \Delta P_{\mathrm{e}}}{\sum_{i \in \mathcal{G}_{\mathrm{po}}} K_i \alpha^i} \qquad \forall i \in \mathcal{G}_{\mathrm{po}} \tag{3.22}$$

For notational simplicity, we assume that all generators participating in PFR have the same droop constant K, which simplifies (3.22) such that all generators carry the same value in their own base units.

$$\Delta P_{\mathrm{m}}^{i} = \frac{\Delta P_{\mathrm{e}}}{\sum_{i \in \mathcal{G}_{\mathrm{po}}} \alpha^i} \qquad \forall i \in \mathcal{G}_{\mathrm{po}} \tag{3.23}$$

Given some lower bound on the frequency deviation $\Delta\omega_{\mathrm{lim}} < 0$ which we will also notate as $-\left|\Delta\omega_{\mathrm{lim}}\right|$, we wish to derive the maximum electrical disturbance magnitude that does not

violate the frequency bound. This is equivalent to finding the maximum positive input (ΔP_{e}) such that one of the states ($\Delta\omega$) of the nonlinear closed-loop system satisfies the bound $\Delta\omega \geq -|\Delta\omega_{\mathrm{lim}}|$ for all time. This is challenging due to the nonlinear nature of the SAT1 block and high-order linear terms in the turbines. PFR is delivered by multiple generators with different response rates, which further complicates the problem.

Another degree of freedom comes from the power setpoints P_{ref}. An increase in the setpoints prompts an increase in output power, even when a frequency deviation is not present. For example, a positive ΔP_{ref} will prompt a power output increase by feeding a positive value through SAT1 to the turbine, as shown in 3.5. During normal operating conditions, the power setpoints P_{ref} remain unchanged when PFR is activated during contingency events such as generator outages or line faults. It is impossible for operators to use the setpoints to improve frequency response because the contingencies, by nature, cannot be anticipated in advance. However, during the restoration process, electrical imbalances are caused by planned actions with known magnitudes and timing. Therefore, the generator setpoints can be adjusted simultaneously to restorative actions to improve the dynamic response of the system. A natural way to assign setpoints is to change the setpoints to their respective post-PFR steady-state outputs from (3.23).

$$\Delta P_{\mathrm{ref}} = \frac{\Delta P_{\mathrm{e}}}{\sum_{i \in \mathcal{G}_{\mathrm{po}}} \alpha^i}. \tag{3.24}$$

With this selection, the initial signal entering SAT1 from Fig. 3.5 at the onset of a power imbalance is $\frac{\Delta P_{\mathrm{ref}}}{T_3}$. If this value is greater than the upper rate limit of the saturation block, U_{o}, SAT1 will be active. Moreover, during a power shortage ($\Delta P_{\mathrm{e}} > 0$), the declining frequency will activate PFR and increase the signal entering SAT1 until the frequency decline is arrested. Hence, if SAT1 is initially activated ($\frac{\Delta P_{\mathrm{ref}}}{T_3} \geq U_{\mathrm{o}}$), it remains activated until the frequency nadir is reached. Importantly, this implies that for the purposes of calculating the nadir, we can assume that SAT1 is always in an active state. Under this approximation, the feedback loop in Fig. 3.6 is broken and the SAT1 block is replaced by a constant source U_{o}. Combined with the integrator block that follows, the simplified PFR is characterized by a linear ramp that feeds into the turbine block. As such, we term this approach the "Ramp Approximation". Physically, the approximation assumes that all generators respond to a power shortage by increasing their output at their maximum rates. The method will produce a slightly optimistic value of the frequency nadir, as the actual PFR will be slower. Condition $\frac{\Delta P_{\mathrm{ref}}}{T_3} \geq U_{\mathrm{o}}$ is more likely to be satisfied for larger imbalances. The approximate open-loop system is shown in Fig. 3.7.

Next, we present a simple example to illustrate the derivation of the frequency nadir using the ramp approximation, and extend the approach to general multi-machine systems with damping.

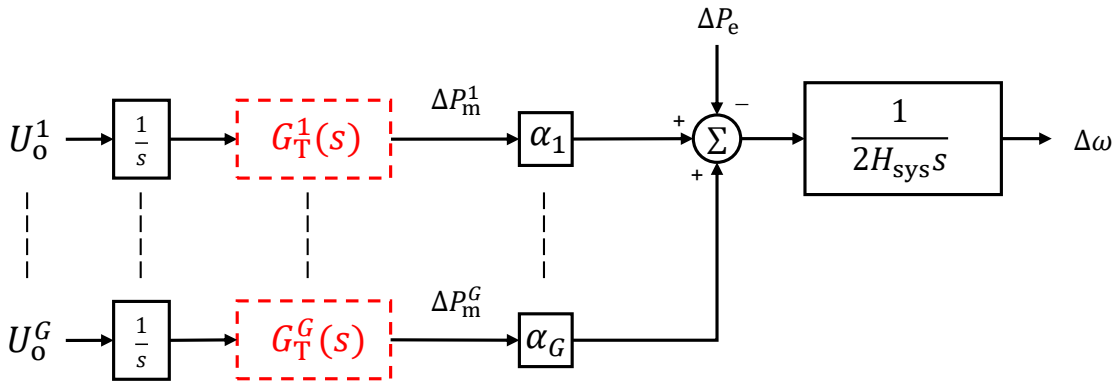

Figure 3.7: Open-loop model of the ramp approximation

3.2.2 Single-Machine Zero-Damping Example

We consider a single-machine system, neglect the effects of the damping coefficient D_{sys}, and approximate the turbine block with the low-pass filter $\frac{1}{sT_4+1}$. This closed-loop system can be expressed in the time domain by the nonlinear state-space model

$$\begin{aligned}
\Delta\dot{\omega}(t) &= \frac{1}{2H_{\text{sys}}}\left(\alpha\Delta P_{\text{m}}(t) - \Delta P_{\text{e}}\right) \\
\dot{x}(t) &= \frac{1}{T_1}\left(-x(t) + K\Delta\omega(t)\right) \\
\dot{\tilde{a}}(t) &= \text{sat}_1\left(\frac{1}{T_3}\left[\left(\frac{T_2}{T_1} - 1\right)x(t) - \frac{T_2}{T_1}K\Delta\omega(t) - \tilde{a}(t) + P_{\text{ref}}\right]\right) \\
\Delta\dot{P}_{\text{m}}(t) &= \frac{1}{T_4}\left(-\Delta P_{\text{m}}(t) + \tilde{a}(t)\right)
\end{aligned}$$

where $x, \tilde{a} \in \mathbb{R}$ are internal states of the governor. Under the assumption that a steady state is reached before the disturbance, the states $\Delta\omega, \Delta P_{\text{m}}$ have zero initial values as they represent deviations from the steady state. From the state-space model, it follows that the governor internal states also have zero initial values. Applying the ramp approximation, the third state simplifies to a linear ramp with slope U_{o} for all positive time.

$$\tilde{a}(t) = U_{\text{o}}t$$

The fourth state, the output mechanical power, can now be solved by the ODE

$$\Delta\dot{P}_{\text{m}}(t) = \frac{1}{T_4}\left(-\Delta P_{\text{m}}(t) + U_{\text{o}}t\right)$$

With the zero initial condition, the solution is

$$\Delta P_{\text{m}}(t) = T_4U_{\text{o}}e^{-\frac{1}{T_4}t} + U_{\text{o}}t - T_4U_{\text{o}}$$

Substituting $\Delta P_{\mathrm{m}}(t)$ into the equation for $\Delta\dot{\omega}(t)$ and integrating, an explicit expression for the frequency deviation is obtained in (3.25).

$$\Delta\omega(t) = \frac{1}{2H_{\mathrm{sys}}}\left(-\alpha T_4^2 U_{\mathrm{o}} e^{-\frac{1}{T_4}t} + \frac{1}{2}\alpha U_{\mathrm{o}} t^2 - \alpha T_4 U_{\mathrm{o}} t - \Delta P_{\mathrm{e}} t + \alpha T_4^2 U_{\mathrm{o}}\right) \tag{3.25}$$

If the turbine time constant is small ($T_4 \ll 1$), the exponential term has a small coefficient and decays quickly. By neglecting it in the nadir calculations, the remaining expression is quadratic in time. The nadir is achieved at time $t_{\mathrm{nadir}} = T_4 + \frac{\Delta P_{\mathrm{e}}}{\alpha U_{\mathrm{o}}}$, with a nadir value computed to be

$$\Delta\omega(t_{\mathrm{nadir}}) = \frac{U_{\mathrm{o}}}{4H_{\mathrm{sys}}}\left(T_4^2 - 2\frac{T_4\Delta P_{\mathrm{e}}}{U_{\mathrm{o}}} - \frac{\Delta P_{\mathrm{e}}^2}{U_{\mathrm{o}}^2}\right)$$

For an imposed frequency limit $\Delta\omega(t_{\mathrm{nadir}}) \geq -|\Delta\omega_{\mathrm{lim}}|$, the corresponding maximum load increase $\Delta P_{\mathrm{e,max}}$ can be found by solving the quadratic inequality.

$$\frac{U_{\mathrm{o}}}{4H_{\mathrm{sys}}}\left(T_4^2 - 2\frac{T_4\Delta P_{\mathrm{e}}}{U_{\mathrm{o}}} - \frac{\Delta P_{\mathrm{e}}^2}{U_{\mathrm{o}}^2}\right) \geq -|\Delta\omega_{\mathrm{lim}}| \tag{3.26a}$$

$$(\Delta P_{\mathrm{e}} + U_{\mathrm{o}}T_4)^2 - 2U_{\mathrm{o}}^2T_4^2 - 4H_{\mathrm{sys}}U_{\mathrm{o}}|\Delta\omega_{\mathrm{lim}}| \leq 0 \tag{3.26b}$$

$$\Delta P_{\mathrm{e}} \leq \sqrt{2U_{\mathrm{o}}^2T_4^2 + 4H_{\mathrm{sys}}U_{\mathrm{o}}|\Delta\omega_{\mathrm{lim}}|} - U_{\mathrm{o}}T_4 = \Delta P_{\mathrm{e,max}} \tag{3.26c}$$

First, the frequency limit is substituted into the nadir expression yielding an inequality. From (3.26a), we multiply both sides by $4H_{\mathrm{sys}}U_{\mathrm{o}}$ and complete the square for ΔP_{e} to obtain (3.26b). Finally, the power imbalance term can be isolated to obtain $\Delta P_{\mathrm{e,max}}$. If the system inertia and frequency limit are fixed and the generator parameters U_{o}, T_4 are known, (3.26c) gives a solvable bound on the electrical disturbance that can be introduced. This derivation can also be done in the Laplace domain, where the expression for the frequency deviation is

$$\Delta\omega(s) = \frac{1}{2H_{\mathrm{sys}}s}\left(\frac{\alpha U_{\mathrm{o}}}{s^2}\left(\frac{1}{sT_4+1}\right) - \frac{\Delta P_{\mathrm{e}}}{s}\right) \tag{3.27}$$

We examine the effect of neglecting the fast-decaying exponential term. By using the Laplace operator $\mathcal{L}(\cdot)$ on (3.25), we arrive at

$$\begin{aligned}\Delta\omega(s) &= \mathcal{L}\left[\frac{1}{2H_{\mathrm{sys}}}\left(\frac{1}{2}\alpha U_{\mathrm{o}}t^2 - \alpha T_4 U_{\mathrm{o}} t - \Delta P_{\mathrm{e}} t + \alpha T_4^2 U_{\mathrm{o}}\right)\right] \\ &= \frac{1}{2H_{\mathrm{sys}}}\left(\frac{\alpha U_{\mathrm{o}}}{s^3} - \frac{\alpha T_4 U_{\mathrm{o}}}{s^2} - \frac{\Delta P_{\mathrm{e}}}{s^2} + \frac{\alpha T_4^2 U_{\mathrm{o}}}{s}\right) \\ &= \frac{1}{2H_{\mathrm{sys}}s}\left(\frac{\alpha U_{\mathrm{o}}}{s^2}\left(1 - sT_4 + s^2T_4^2\right) - \frac{\Delta P_{\mathrm{e}}}{s}\right)\end{aligned} \tag{3.28}$$

where the low-pass filter block $\frac{1}{sT_4+1}$ from (3.27) is replaced by its second-order polynomial expansion $1 - sT_4 + s^2T_4^2$. In Fig. 3.8, the Bode plots of the first terms of (3.27) and (3.28) are compared for two values of T_4.

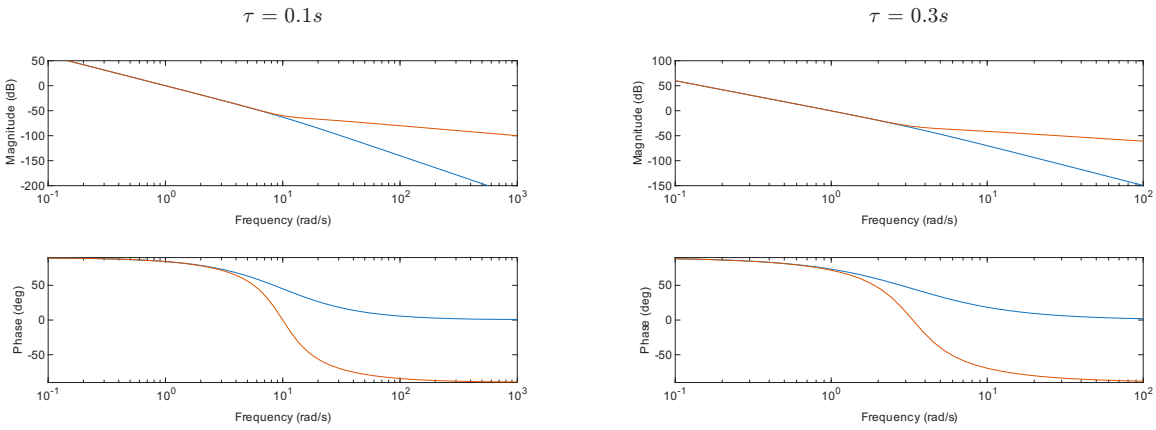

Figure 3.8: Bode plots of first-order term and its approximation

The polynomial is an accurate approximation for the frequency range $[0, \frac{1}{T_4}]$. The $\frac{1}{s^3}$ term that precedes the first-order term strongly attenuates high-frequency components. We see that although $1 - sT_4 + s^2T_4^2$ fails as an approximation at high frequencies, the magnitude of errors are small compared to the dominant low frequency components. Therefore, the polynomial is an appropriate approximation of the low-pass filter when T_4 is small. This is consistent with the time-domain interpretation, as when T_4 is small, the exponential term, which the errors in the Bode plot represent, decays faster. The difference between the polynomial approximation and the low-pass filter is exactly the neglected exponential term in the time domain, as shown by

$$\frac{\alpha}{s^3}\left(\frac{1}{sT_4+1} - \left(1 - sT_4 + s^2T_4^2\right)\right) = \frac{\alpha T_4^3}{sT_4+1} = \mathcal{L}\left[\alpha T_4^2 e^{-\frac{1}{T_4}t}\right] \tag{3.29}$$

3.2.3 Multi-machine Generalization

We now expand the analysis to the multi-machine scenario with the full $G_{\mathrm{T}}(s)$ turbine model shown in Fig. 3.6. Following the ramp approximation, each generator participating in PFR activates its SAT1 block and sustains the power output rate limits $\boldsymbol{U}_{\mathrm{o}}$ prior to the nadir, yielding the open loop system in Fig. 3.7. The Laplace expression for the mechanical power output of generator i,

$$\Delta P_{\mathrm{m}}^i(s) = \frac{U_{\mathrm{o}}^i}{s^2} G_{\mathrm{T}}^i(s),$$

gives a corresponding frequency response of

$$\Delta\omega(s) = \frac{1}{2H_{\mathrm{sys}}}\left(\frac{1}{s^3}\sum_{i\in\mathcal{G}_{\mathrm{po}}} \alpha^i U_{\mathrm{o}}^i G_{\mathrm{T}}^i(s) - \frac{\Delta P_{\mathrm{e}}}{s^2}\right) \tag{3.30}$$

where the first term represents the combined PFR of the SGs, and the second term represents the disturbance. $\mathcal{G}_{\mathrm{po}}$ is the set of generators participating in the PFR. The fourth-order

turbine transfer function $G_{\mathrm{T}}(s)$ is given by

$$G_{\mathrm{T}}(s) = \frac{1}{sT_4+1}\left(K_1 + \frac{1}{sT_5+1}\left(K_3 + \frac{1}{sT_6+1}\left(K_5 + \frac{K_7}{sT_7+1}\right)\right)\right) \tag{3.31}$$

The turbine has a unity DC gain, which is true when

$$K_1 + K_3 + K_5 + K_7 = 1$$

Like in the example, we replace all $\frac{1}{sT_i+1}$ terms in (3.31) with their second-order polynomial approximations $1 - sT + s^2T^2$ by assuming that $T_4^i, T_5^i, T_6^i, T_7^i$ are small.

$$\begin{aligned} G_{\mathrm{T}}(s) \approx (1 - sT_4 + s^2T_4^2)(K_1 + (1 - sT_5 + s^2T_5^2)(K_3 \\ + (1 - sT_6 + s^2T_6^2)(K_5 + (1 - sT_7 + s^2T_7^2)))) \end{aligned}$$

The expression can be expanded, and we neglect terms in s with an order higher than two. The result is a quadratic expression of the form

$$G_{\mathrm{T}}(s) \approx c_1 - c_2 s + c_3 s^2 \tag{3.32}$$

with coefficients

$$c_1 = K_1 + K_3 + K_5 + K_7 = 1 \tag{3.33a}$$

$$c_2 = T_4 + T_5(K_3 + K_5 + K_7) + T_6(K_5 + K_7) + K_7T_7) \tag{3.33b}$$

$$\begin{aligned} c_3 = {} & T_4^2 + T_5(K_3 + K_5 + K_7)(T_4 + T_5) \\ & + T_6(K_5 + K_7)(T_4 + T_5 + T_6) + K_7T_7(T_4 + T_5 + T_6 + T_7) \end{aligned} \tag{3.33c}$$

The coefficients c_1, c_2, c_3 depend only on the turbine parameters and can be found in advance with knowledge of the turbine model alone. Substituting each $G_{\mathrm{T}}^i(s)$ with approximation in (3.32), the expression for frequency deviation becomes

$$\begin{aligned} \Delta\omega(s) &= \frac{1}{2H_{\mathrm{sys}}}\left(\frac{1}{s^3}\sum_{i\in\mathcal{G}_{\mathrm{po}}} \alpha^i U_{\mathrm{o}}^i (1 - c_2^i s + c_3^i s^2)) - \frac{\Delta P_{\mathrm{e}}}{s^2}\right) \\ &= \frac{1}{2H_{\mathrm{sys}}}\left(\frac{1}{s^3}\left(\sum_{i\in\mathcal{G}_{\mathrm{po}}} \alpha^i U_{\mathrm{o}}^i\right) - \frac{1}{s^2}\left(\sum_{i\in\mathcal{G}_{\mathrm{po}}} \alpha^i U_{\mathrm{o}}^i c_2^i\right) + \frac{1}{s}\left(\sum_{i\in\mathcal{G}_{\mathrm{po}}} \alpha^i U_{\mathrm{o}}^i c_3^i\right) - \frac{\Delta P_{\mathrm{e}}}{s^2}\right) \end{aligned}$$

For notational simplicity, we define the coefficients $C_1, C_2, C_3 \in \mathbb{R}_+$ as

$$C_1 = \sum_{i \in \mathcal{G}_{\text{po}}} \alpha^i U_{\text{o}}^i \tag{3.34a}$$

$$C_2 = \sum_{i \in \mathcal{G}_{\text{po}}} \alpha^i U_{\text{o}}^i c_2^i \tag{3.34b}$$

$$C_3 = \sum_{i \in \mathcal{G}_{\text{po}}} \alpha^i U_{\text{o}}^i c_3^i \tag{3.34c}$$

Note that while c_1, c_2, c_3 depend solely on the turbine models, C_1, C_2, C_3 depend on the set of online generators that provide the PFR $\mathcal{G}_{\text{po}}$. With this, the expression becomes

$$\Delta\omega(s) = \frac{1}{2H_{\text{sys}}} \left(\frac{C_1}{s^3} - \frac{C_2}{s^2} - \frac{\Delta P_{\text{e}}}{s^2} + \frac{C_3}{s} \right) \tag{3.35}$$

which is analogous to the single-machine simple turbine case. Converting back to the time domain yields

$$\Delta\omega(t) = \frac{1}{2H_{\text{sys}}} \left(\frac{1}{2} C_1 t^2 - C_2 t - \Delta P_{\text{e}} t + C_3 \right)$$

The nadir occurs at $t_{\text{nadir}} = \frac{C_2 + \Delta P_{\text{e}}}{C_1}$, and the expression of the nadir is

$$\Delta\omega(t_{\text{nadir}}) = \frac{1}{2H_{\text{sys}}} \left(-\frac{(C_2 + \Delta P_e)^2}{2C_1} + C_3 \right) \tag{3.36}$$

Finally, the corresponding maximum power imbalance is

$$\Delta P_{\text{e}} \leq \sqrt{4H_{\text{sys}} C_1 \left|\Delta\omega_{\text{lim}}\right| + 2C_1 C_3} - C_2 = \Delta P_{\text{e,max}} \tag{3.37}$$

The maximum safe imbalance is a function of the frequency limit $|\Delta\omega_{\text{lim}}|$ and parameters $C_1, C_2, C_3, H_{\text{sys}}$, which depend on the set of active generators. Section 3.3 details how the active generator set can be predicted such that the maximum safe imbalance can be represented in the MILP by a constant value.

3.2.4 Nonzero Damping Coefficient

Next, we show that the ramp approximation can be applied to systems with a nonzero damping coefficient, which have the ASF swing equation

$$\Delta\omega(s) = \frac{1}{2H_{\text{sys}} s + D_{\text{sys}}} \left(\Delta P_{\text{m}}(s) - \Delta P_{\text{e}}(s) \right) \tag{3.38}$$

Synchronous machines have much larger inertia constants than damping coefficients, and the effects of damping is usually neglected in the ASF model. However, there are scenarios where damping effects are substantial—for example, the work in [45] shows how the fast

frequency response (FFR) provided by IBRs can be captured by an effective damping coefficient. Although FFR is out of the scope of this work, we demonstrate in this section that the power imbalance bound can be similarly derived when damping effects cannot be ignored. Following the same procedure as in the zero damping case, we begin from the Laplace domain ramp-approximated frequency expression from (3.30) and substitute $G_{\mathrm{T}}(s)$ using the turbine approximation (3.32).

$$\begin{aligned}\Delta\omega(s) &= \frac{1}{2H_{\mathrm{sys}}s + D_{\mathrm{sys}}}\left(\frac{1}{s^2}\sum_{i\in\mathcal{G}_{\mathrm{po}}}\alpha^i U_{\mathrm{o}}^i G_{\mathrm{T}}^i(s) - \frac{\Delta P_{\mathrm{e}}}{s}\right)\\ &= \frac{1}{2H_{\mathrm{sys}}s + D_{\mathrm{sys}}}\left(\frac{C_1}{s^2} - \frac{C_2}{s} - \frac{\Delta P_{\mathrm{e}}}{s} + C_3\right)\end{aligned}$$

The expression is simplified by taking the partial fractions of each term, taking the inverse Laplace, and finding the minimum point of the time-domain frequency expression, which gives

$$\begin{aligned}\Delta\omega(t_{\mathrm{nadir}}) = &-\frac{C_2}{D_{\mathrm{sys}}} - \frac{\Delta P_{\mathrm{e}}}{D_{\mathrm{sys}}}\\ &+ \frac{2H_{\mathrm{sys}}C_1}{D_{\mathrm{sys}}^2}\ln\left(\frac{1}{4H_{\mathrm{sys}}^2C_1}\left(4H_{\mathrm{sys}}^2C_1 + 2H_{\mathrm{sys}}D_{\mathrm{sys}}(C_2+\Delta P_{\mathrm{e}}) + D_{\mathrm{sys}}^2C_3\right)\right)\end{aligned} \tag{3.39}$$

This is an equation with linear and logarithmic terms of ΔP_{e}, and its solution can be explicitly expressed by the Lambert W function $W(\cdot)$. By replacing $\Delta\omega(t_{\mathrm{nadir}}) \geq -|\Delta\omega_{\mathrm{lim}}|$ and performing some algebraic operations, we manipulate the inequality into the form $ye^y = x$, where y contains the variable we wish to isolate, ΔP_{e}.

$$\begin{aligned}\left(-1 - \frac{D_\Sigma C_2 + D\Delta P_{\mathrm{e}}}{2H_\Sigma C_1} - \frac{D_\Sigma^2 C_3}{4H_\Sigma^2 C_1}\right)\exp\left(-1 - \frac{D_\Sigma C_2 + D\Delta P_{\mathrm{e}}}{2H_\Sigma C_1} - \frac{D_\Sigma^2 C_3}{4H_\Sigma^2 C_1}\right)\\ \leq -\exp\left(-\frac{D_\Sigma^2\,|\omega_{\mathrm{lim}}|}{2H_\Sigma C_1} - \frac{D_\Sigma^2 C_3}{4H_\Sigma^2 C_1} - 1\right)\end{aligned}$$

When $-\frac{1}{e} \leq x \leq 0$, as is in this case, two solutions exist for the equation $ye^y = x$: $y = W_0(x)$ and $y = W_{-1}(x)$, where $W_0(\cdot), W_{-1}(\cdot)$ are the principal and lower branches of the Lambert W function. We can express our inequality in terms of the Lambert W function, where the lower branch gives the maximum value for ΔP_{e}.

$$\left(-1 - \frac{D_{\mathrm{sys}}C_2 + D\Delta P_{\mathrm{e}}}{2H_{\mathrm{sys}}C_1} - \frac{D_{\mathrm{sys}}^2 C_3}{4H_{\mathrm{sys}}^2 C_1}\right) = W_{-1}\left(-\exp\left(-\frac{D_{\mathrm{sys}}^2\,|\omega_{\mathrm{lim}}|}{2H_{\mathrm{sys}}C_1} - \frac{D_{\mathrm{sys}}^2 C_3}{4H_{\mathrm{sys}}^2 C_1} - 1\right)\right)$$

Finally, by isolating for ΔP_{e}, the safe imbalance bound

$$\Delta P_{\mathrm{e}} \leq -\frac{2H_{\mathrm{sys}}C_1}{D_{\mathrm{sys}}}\left(w_{-1} + 1 + \frac{D_{\mathrm{sys}}C_2}{2H_{\mathrm{sys}}C_1} + \frac{D_{\mathrm{sys}}^2 C_3}{4H_{\mathrm{sys}}^2 C_1}\right) = \Delta P_{\mathrm{e,max}} \tag{3.40}$$

is found with

$$w_{-1} = W\left(-\exp\left(-\frac{D_{\text{sys}}^2\,|\omega_{\text{lim}}|}{2H_{\text{sys}}C_1} - \frac{D_{\text{sys}}^2 C_3}{4H_{\text{sys}}^2 C_1} - 1\right)\right)$$

Compared to the bound for systems without damping in (3.37), this bound allows larger imbalances when the frequency nadir limit and system parameters (except D_{sys}) are identical. The damping constant reduces the magnitude of the nadir for any given power imbalance, so a larger imbalance is needed to violate the frequency limit. To assess the correctness of (3.40), we can show that as D_{sys} approaches zero, the expression converges to the bound without damping in (3.37). That is,

$$\begin{aligned}\lim_{D_{\text{sys}}\to 0} &-\frac{2H_{\text{sys}}C_1}{D_{\text{sys}}}\left(w_{-1} + 1 + \frac{D_{\text{sys}}C_2}{2H_{\text{sys}}C_1} + \frac{D_{\text{sys}}^2 C_3}{4H_{\text{sys}}^2 C_1}\right)\\ &= \sqrt{4H_{\text{sys}}C_1\,|\Delta\omega_{\text{lim}}| + 2C_1C_3} - C_2 \end{aligned} \tag{3.41}$$

The proof is presented in Appendix C.

3.3 Frequency-constrained MILP Synthesis

In this section, we will show how the frequency nadir constraints from the previous section are integrated into the restoration MILP. First, we show how (3.37) can be integrated into the MILP framework. By adopting an iterative receding-horizon algorithm, we show how the constraint can be made linear in terms of the binary decision variables.

3.3.1 Frequency Constraint Formulation

The power imbalance bound in (3.37) is introduced as linear constraints to ensure that the frequency nadir limit is satisfied.

During restoration, net electrical imbalances $\boldsymbol{\Delta P}_{\text{e}} \in \mathbb{R}^{1\times T}$ are caused by load pick-ups and generator cranking, expressed for all $k \in \{1,\dots,T\}$

$$\boldsymbol{\Delta P}_{\text{e}}(k) = \boldsymbol{P}_{\text{d}}^{\top}\left(\boldsymbol{b}_{\text{d}}(k) - \boldsymbol{b}_{\text{d}}(k-1)\right) + \boldsymbol{P}_{\text{c}}^{\top}\left(\boldsymbol{b}_{\text{gc}}(k) - \boldsymbol{b}_{\text{gc}}(k-1)\right) \tag{3.42}$$

which is linear in the decision variables. The bound for these imbalances, $\boldsymbol{\Delta P}_{\text{e,max}}$, depends on the inertia H_{sys} and the parameters C_1, C_2, C_3 defined in (3.34), which must be defined for each time step of the MILP. These parameters depend on the status of the generators $\boldsymbol{b}_{\text{g}}$ and its auxiliary variables.

Generators begin to contribute to the system inertia after they have been synchronized. During the cranking phase, the rotating mass of the turbine is brought to synchronous speed is connected to the electrical system at the onset of the ramping phase. Denoting the vector of inertia for all time steps as $\boldsymbol{H}_{\text{sys}}$ with initial value $\boldsymbol{H}_{\text{sys},0} = \boldsymbol{H}_{\text{sys}}(0)$, the definition from

(2.6) can be rewritten in terms of status variables as

$$\boldsymbol{H}_{\text{sys}}(k) = \tfrac{1}{S_{\text{sys}}} \overline{\boldsymbol{P}}_{\text{g}}^{\top} \operatorname{diag}(\boldsymbol{H})(\boldsymbol{b}_{\text{gr}}(k) + \boldsymbol{b}_{\text{go}}(k)) \qquad \forall k \in \{0, \dots, T\} \tag{3.43}$$

where $\boldsymbol{b}_{\text{gr}}$ and $\boldsymbol{b}_{\text{go}}$ are the previously introduced indicators of the ramping and online phases and vector $\boldsymbol{H} \in \mathbb{R}^G$ contains the inertia constants of each generator. The set of synchronized generators $\mathcal{G}_{\text{s}}$, which was used in the sum in (2.6), is encoded in the binary variables. Let $\boldsymbol{\alpha} \in \mathbb{R}^{G \times T}$ denote the power conversion factors matrix, with initial values $\boldsymbol{\alpha}_0 = \boldsymbol{\alpha}(0)$, and rewrite the definition from (2.8) in terms of the status variables as

$$\boldsymbol{\alpha}(k) = \tfrac{1}{S_{\text{sys}}} \operatorname{diag}(\overline{\boldsymbol{P}}_{\text{g}}) \boldsymbol{b}_{\text{go}}(k), \qquad k \in \{1, \dots, T\}. \tag{3.44}$$

The set of online generators that provide PFR $\mathcal{G}_{\text{po}}$ is encoded in $\boldsymbol{\alpha}$ by the online status $\boldsymbol{b}_{\text{go}}$ as they determine the parameters C_1, C_2, C_3. The definition in (3.44) assumes that all NBSUs contribute to the PFR once they are fully activated. However, we may only want some of the generators to provide PFR *once online*. This set $\mathcal{G}_{\text{p}}$, where $\mathcal{G}_{\text{po}} \subseteq \mathcal{G}_{\text{p}}$ can be represented in the expression for $\boldsymbol{\alpha}$ by constructing a constant vector $\boldsymbol{p} \in \{0, 1\}^G$ where for all $i \in \{1, \dots, G\}$,

$$\boldsymbol{p}_i = \begin{cases} 1, & i \in \mathcal{G}_{\text{p}} \\ 0, & i \notin \mathcal{G}_{\text{p}} \end{cases} \tag{3.45}$$

The ith element of $\boldsymbol{p}$ indicates whether generator i has been selected to provide PFR once online. The first element represents the BSU and must be 1 since the PFR set would initially be empty. Incorporating this into the definition of $\boldsymbol{\alpha}$ yields

$$\boldsymbol{\alpha}(k) = \tfrac{1}{S_{\text{sys}}} \operatorname{diag}(\boldsymbol{p}) \operatorname{diag}(\overline{\boldsymbol{P}}_{\text{g}}) \boldsymbol{b}_{\text{go}}(k), \qquad k \in \{1, \dots, T\}. \tag{3.46}$$

The nonzero values of $\boldsymbol{\alpha}$ now describe $\mathcal{G}_{\text{po}}$, as it is the intersection of the online set and $\mathcal{G}_{\text{p}}$. To vectorize (3.34), let the vector forms of the parameters $\boldsymbol{C}_1, \boldsymbol{C}_2, \boldsymbol{C}_3 \in \mathbb{R}_+^{1 \times T}$ be defined for all T steps in the MILP as

$$\boldsymbol{C}_1 = \boldsymbol{U}_{\text{o}}^{\top} \boldsymbol{\alpha} \tag{3.47a}$$

$$\boldsymbol{C}_2 = \boldsymbol{U}_{\text{o}}^{\top} \operatorname{diag}(\boldsymbol{c_2}) \boldsymbol{\alpha} \tag{3.47b}$$

$$\boldsymbol{C}_3 = \boldsymbol{U}_{\text{o}}^{\top} \operatorname{diag}(\boldsymbol{c_3}) \boldsymbol{\alpha} \tag{3.47c}$$

where $\boldsymbol{c_2}, \boldsymbol{c_3} \in \mathbb{R}^G$ are constant vectors derived from the turbine approximation defined in (3.33), with their ith entries corresponding to the turbine of the ith generator.

Replacing the zero-damping maximum power imbalance with the vectorized parameters

and variables yields

$$\boldsymbol{\Delta P}_{\mathrm{e}}(k) \leq \sqrt{4\boldsymbol{H}_{\mathrm{sys}}(k)\boldsymbol{C}_1(k)\,|\Delta\omega_{\mathrm{lim}}| + 2\boldsymbol{C}_1(k)\boldsymbol{C}_3(k)} - \boldsymbol{C}_2(k) \tag{3.48}$$

which provides a step-wise bound on the magnitude of load pick-up and generator cranking actions. This inequality is nonlinear in terms of the binary decision variables, which are embedded in the step-dependent parameters, and cannot be integrated into the MILP framework. Next, we present an approach to resolve this nonlinearity by updating $\boldsymbol{H}_{\mathrm{sys}}$ and $\boldsymbol{\alpha}$ outside of the MILP in the iterative algorithm discussed in the next section. The approach simplifies the right-hand side of (3.48) and resolves it to a constant value for all time steps.

3.3.2 Updating System Parameters via the Iterative Algorithm

NBSUs are given the start-up signal a fixed number of time steps before their ramping and online phases, determined by the cranking times $\boldsymbol{T}_{\mathrm{c}}$ and ramping times $\boldsymbol{T}_{\mathrm{r}}$. Therefore, if we know when the ith generator is scheduled to turn on, we can obtain the auxiliary variables $\boldsymbol{b}^i_{\mathrm{gr}}$ and $\boldsymbol{b}^i_{\mathrm{go}}$ for all subsequent time steps. If it is assumed that *no other generators are activated during the time horizon* T, $\boldsymbol{H}_{\mathrm{sys}}$ and $\boldsymbol{\alpha}$ can be predicted.

The IRSC Algorithm from Section 3.1.7 can be extended to include this parameter update step.

Algorithm 2 IRSC with Parameter Updates

1: Initialize $\boldsymbol{b}_0$
2: Initialize $\mathsf{plan} = [\boldsymbol{b}_0]$
3: **while** $\boldsymbol{b}_0 \neq \mathbb{1}$ **do**
4: Assuming $\boldsymbol{b}_{\mathrm{g}} = \boldsymbol{b}_{\mathrm{g},0} \cdot \mathbb{1}^{1\times T}$, predict $\boldsymbol{b}_{\mathrm{gr}}$, $\boldsymbol{b}_{\mathrm{go}}$ by evaluating (3.13), (3.15)
5: Evaluate $\boldsymbol{H}_{\mathrm{sys}}$ and $\boldsymbol{\alpha}$ in (3.43), (3.46), using predicted $\boldsymbol{b}_{\mathrm{gr}}$, $\boldsymbol{b}_{\mathrm{go}}$
6: Evaluate $\boldsymbol{C}_1$, $\boldsymbol{C}_2$, $\boldsymbol{C}_3$ in (3.47) using predicted $\boldsymbol{\alpha}$
7: Evaluate $\boldsymbol{\Delta P}_{\mathrm{e,max}}$ using (3.48)
8: Solve the MILP (3.21) with frequency constraint (3.48) for T steps with initial values $\boldsymbol{b}_0$
9: Append the plan with actions in the control period: $[\mathsf{plan}] \leftarrow [\mathsf{plan}, \boldsymbol{b}(1)]$
10: Update initialization $\boldsymbol{b}_0 = \boldsymbol{b}(1)$
11: **end while**
12: Output plan

Vectors $\boldsymbol{H}_{\mathrm{sys}}, \boldsymbol{\alpha}$ are updated for the next iteration whenever the newest saved actions in the restoration plan include a NBSU start-up. A corresponding maximum electrical imbalance $\boldsymbol{\Delta P}_{\mathrm{e,max}}(k)$ can be obtained for all $k \in \{0, \ldots, T\}$, rendering constraints (3.48) linear to be inserted into the next MILP.

As an example, consider an example system in Fig. 3.9, where NBSU1 has a known cranking time $\boldsymbol{T}^1_{\mathrm{c}} = 4$, and we run the iterative algorithm with a horizon of $T = 4$.

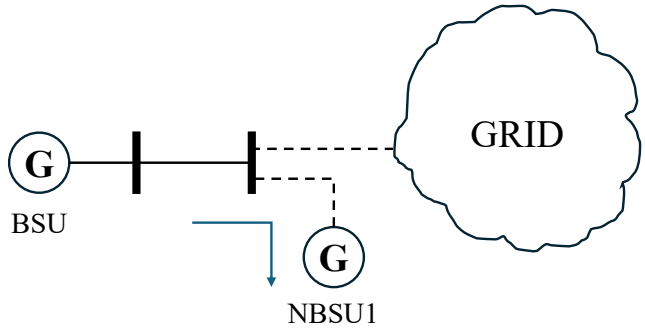

Figure 3.9: An example system to demonstrate the IRSC algorithm

Time Step	0	1	2	3	4	5	6
Iteration 1, obtaining parameters							
$\boldsymbol{H}_{\text{sys}}$	⁄	H_1	H_1	H_1	H_1	H_1	⁄
$\boldsymbol{\Delta P}_{\text{e,max}}$	⁄	ΔP_1	ΔP_1	ΔP_1	ΔP_1	ΔP_1	⁄
Iteration 1, solving MILP							
$\boldsymbol{b}_{\text{g}}$	0	***1***	1	1	1	1	⁄
$\boldsymbol{b}_{\text{gc}}$	0	***1***	1	1	1	0	⁄
Iteration 2, obtaining parameters							
$\boldsymbol{b}_{\text{gc}}$	0	1	1	1	1	0	0
$\boldsymbol{b}_{\text{gr}}$	0	0	0	0	0	1	1
$\boldsymbol{H}_{\text{sys}}$	⁄	⁄	H_1	H_1	H_1	H_2	H_2
$\boldsymbol{\Delta P}_{\text{e,max}}$	⁄	⁄	ΔP_1	ΔP_1	ΔP_1	ΔP_2	ΔP_2
Iteration 2, solving MILP							
$\boldsymbol{b}_{\text{g}}$	⁄	1	***1***	1	1	1	1

Table 3.4: IRSC-based parameter updates on the 3-bus system. Bold and italicized 1 indicate newest actions stored in plan

At the start of the first iteration, the initial values $\boldsymbol{b}_{\mathbf{g,0}}$ are assumed to remain constant throughout the horizon T. The system inertia is supplied by the BSU alone and is notated as H_1 in the table. Doing the same with other parameters, we can find a maximum power imbalance of ΔP_1 using (3.48) for all time steps in the first iteration. After solving the frequency-constrained MILP, the next optimal action prompts NBSU1 to start and enter its cranking phase. The algorithm updates the initial value vector $\boldsymbol{b}_0$ to reflect the NBSU start-up. In the second iteration, the updated initial values are again assumed to be constant during the next T steps. The auxiliary variables $\boldsymbol{b}_{\text{gc}}, \boldsymbol{b}_{\text{gr}}$ can be found under this assumption, and indicate that NBSU1 will enter the ramping phase at the fifth overall time step. The newly synchronized NBSU1 increases the system inertia, notated by H_2, allowing a larger power imbalance ΔP_2 during and after the fifth step without violating the frequency limit.

The process is repeated until the entire system is restored. In general, once an NBSU is started, $\boldsymbol{H}_{\mathbf{sys}}$ and $\boldsymbol{\alpha}$ will be updated at a later time, which increases the bound in constraint (3.48). Physically, this describes how the system becomes more resilient as more SGs are synchronized and join the PFR set. Thus, we are allowing larger power imbalances to be introduced as restoration progresses without violating the static frequency nadir limit. This draws similarities to the IESO load recovery guideline, which recommends load pick-ups of no more than 5% of the online capacity- [8]. Instead, the constraint (3.48) uses the inertia and PFR capability of SGs to approximate a definite value for maximum load pick-up, providing greater transparency into the system behavior and improving reliability.

3.4 Case Study: SGs only

3.4.1 Simulation Setup

A modified IEEE 9-bus system shown in Fig. 3.10 is used to verify the effect of frequency constraints on the optimal restoration sequence. The generator start-up parameters and their IEEEG1 turbine-governors use values referenced from [9] and [44]. Cranking time and ramp rates are chosen within the ranges reported in [41]. The loads in the system are located on buses 4-9 and split into blocks sized between 3-16 MW. Generator 1 is designated as the BSU and generators 2-3 as the NBSUs. All units have a zero damping constant, although nonzero system damping constants can be addressed by methods from Section 3.2.4. For more details on system parameters, please refer to Appendix D.

The system's frequency profile during restoration is obtained by simulating the time-domain ODEs associated with the closed-loop ASF model. The nonlinear system has $6G+1$ states, although we are primarily interested in one state: the frequency deviation. The magnitude of the electrical imbalance following each restorative action, represented by $\boldsymbol{\Delta P}_{\mathrm{e}}$, and the corresponding changes in generator setpoints $\Delta \boldsymbol{P}_{\mathrm{ref}}$ are the inputs to the system. Each generator's setpoint is updated according to (3.24). All SGs in the system participate in PFR, so $\mathcal{G}_{\mathrm{p}} = \{1, 2, 3\}$ and $\boldsymbol{p} = [1 \quad 1 \quad 1]^{\top}$ as defined in (3.45).

The iterative MILP and dynamic simulations are computed in MATLAB. The MILP is constructed using the YALMIP package [46] and solved using GUROBI [47]. Dynamic simulation is conducted by MATLAB's in-built ODE solver. In addition, we validate the restoration plans under more realistic conditions using PSS/E, an industry-level power systems simulator. The software is able to capture effects neglected by the ASF model, such as the transient effects of line charging, load energization, and regional frequency swings. The test system is replicated in PSS/E format and the same restoration sequences are followed. The PSS/E validation components of this work are credited to Dr. Ilyas Farhat, and more details of the PSS/E model can be found in [48].

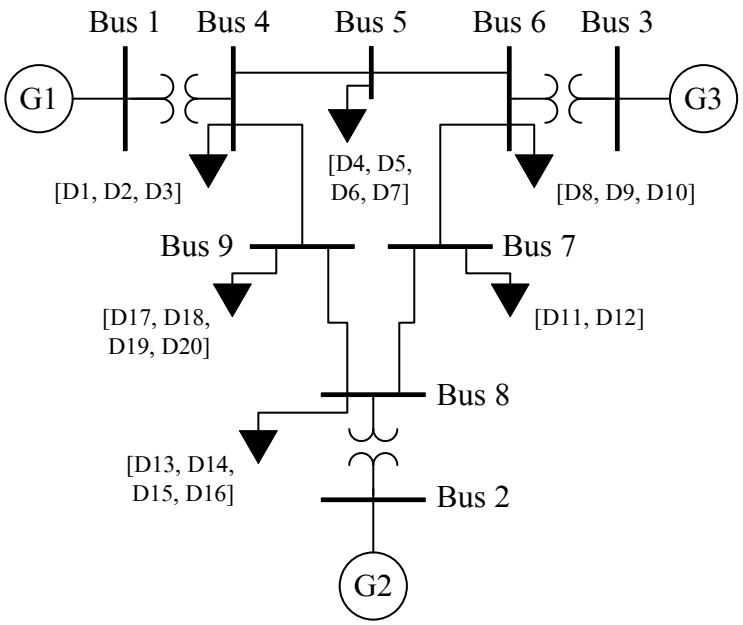

Figure 3.10: Modified IEEE 9-bus system. Number in brackets denote the indices of loads on each bus

3.4.2 Frequency Nadir Prediction

The ramp approximation assumes that if the generator setpoints are allocated as in (3.24), then the initial value entering SAT1 will activate the saturation block. To visualize the performance of the ramp approximation, we introduce loads of various sizes to the modified IEEE 9-bus system with all three generators participating in PFR. The system's frequency deviations under each imbalance, along with their predicted nadirs, are plotted in Fig. 3.11.

The steady-state frequencies return to the nominal due to the manner in which the generator setpoints are selected. In an actual system, power loss and regional generator behavior necessitates secondary control (see Fig. 2.1), which is typically responsible for driving the frequency back to its nominal value. In all cases, the ramp approximation predicts the frequency nadir values optimistically, but the errors decrease as the load magnitude increases. To illustrate this more clearly, the signals entering SAT1 are shown alongside the frequency deviations in Fig. 3.12.

In all cases, the saturation block is activated immediately after the power imbalance is introduced and remains active until the nadir is reached. For even smaller imbalances, SAT1 can remain inactive briefly, leading to higher prediction errors. However, cases with small imbalances are negligible because the small frequency nadirs that ensue will likely remain within safe limits. The frequency nadir prediction error is plotted as a function of the load pick-up magnitude in Fig. 3.13.

The prediction error is highest when the power imbalance is close to zero. As the imbalance increases, the corresponding change in ΔP_{ref} triggers SAT1 more consistently, resulting

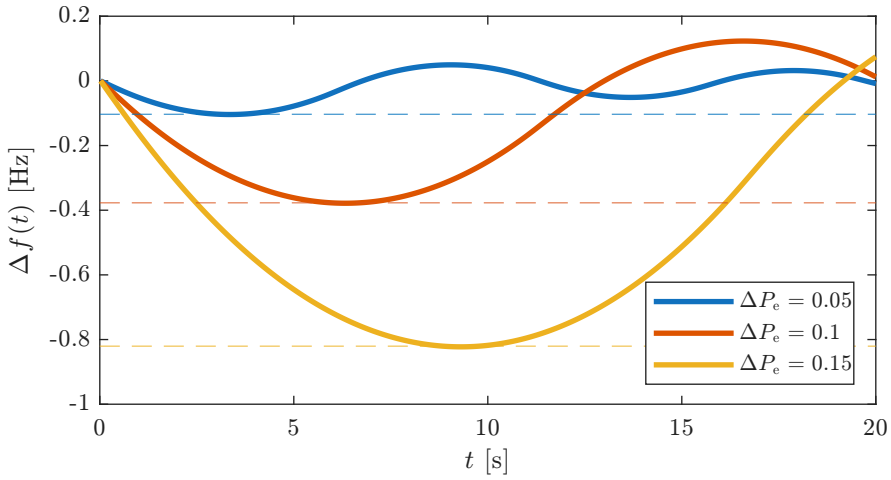

Figure 3.11: System Frequency response to loads of various magnitudes. **In solid**: Actual system frequency response. **Dashed**: Frequency nadir predictions from (3.36)

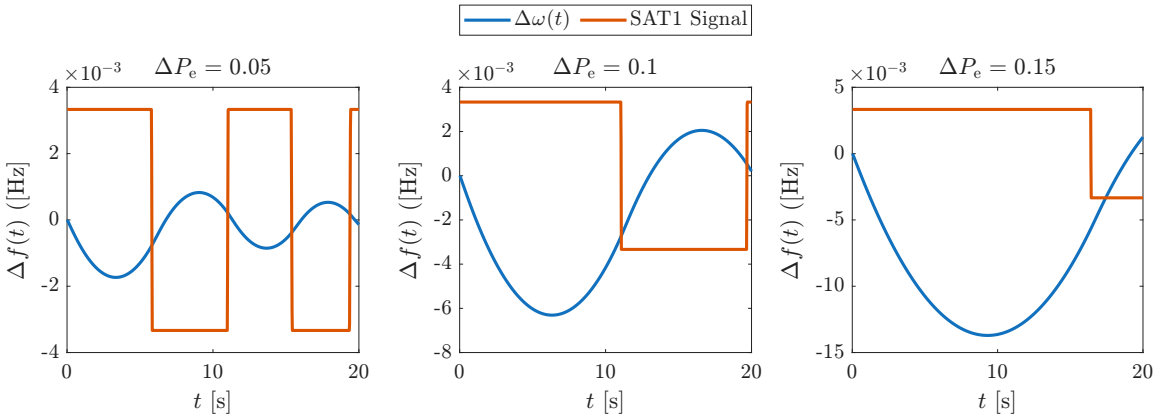

Figure 3.12: Signal entering SAT1 following various load pick-ups

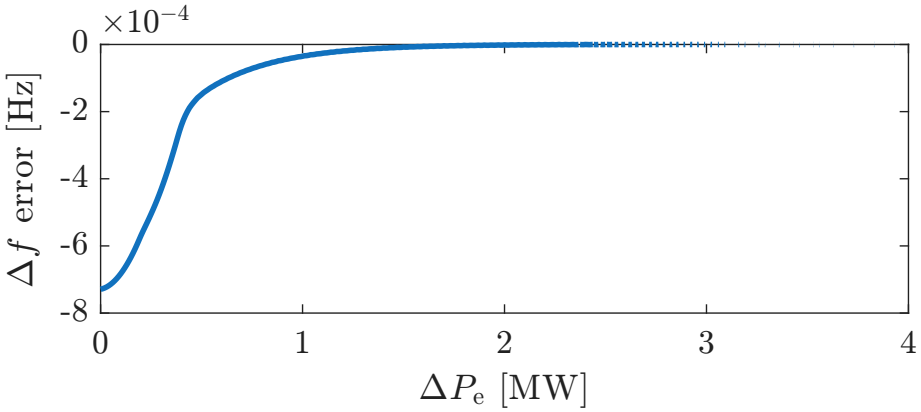

Figure 3.13: Frequency nadir estimation error of the ramp approximation

in lower prediction errors. The errors are lowest near the maximum imbalance permitted by the nadir constraint, though estimates remain slightly optimistic due to the assumption of maximum generator response. In the 9-bus system, the smallest load—3 MW—yields a negligible nadir error on the order of 10^{-4} Hz. Even in the worst-case scenario, the prediction error does not exceed 10^{-3} Hz. These results confirm that the nadir is accurately predicted and that the constraint in (3.37) accurately enforces the frequency limit $\Delta\omega_{\text{lim}}$.

3.4.3 Frequency-Constrained Restoration Sequences

To show the effect of frequency constraints on restoration sequences, two optimal plans are found using the iterative method described in Algorithm 1. The first sequence is found without using the frequency constraints (3.48), while the second enforces a 1 Hz nadir limit. Restorative actions are performed every two minutes to allow the transient dynamics to settle. Fig. 3.14 illustrates the MATLAB simulation of the frequency profile during both restoration sequences. Actions are allowed to occur every two minutes ($t = 2$).

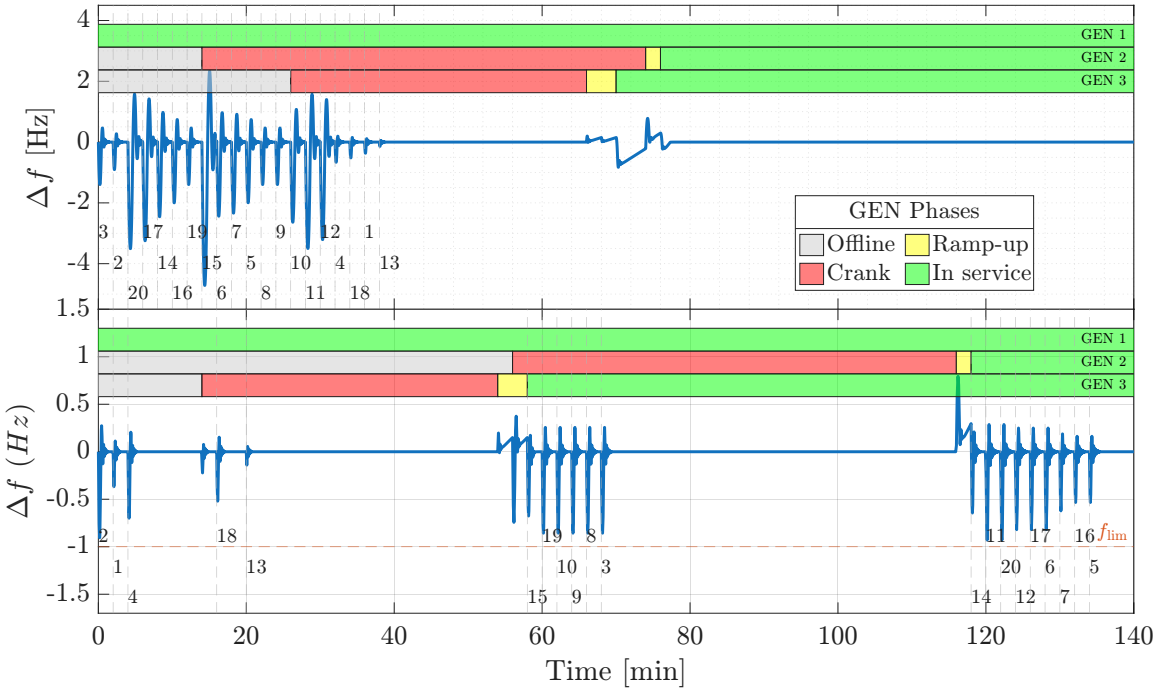

Figure 3.14: Frequency behaviour during restoration sequences. **Top**: No frequency limit. **Bottom**: 1 Hz frequency nadir limit. Label numbers indicate the indices of restored loads

In the unconstrained case, all generators and loads are energized in rapid succession by the black-start unit. Restoration completes in 40 steps as the NBSUs complete their ramping phases. However, the low-inertia system experiences frequency drops as low as 4 Hz below nominal due to the early energization of large loads. The plan is clearly infeasible in a real-world system, as such drastic frequency deviations will trigger protection systems or damage equipment.

In contrast, enforcing a 1 Hz nadir constraint results in a more gradual sequence. The early stages involve only small load pick-ups due to low system inertia. Following each NBSU's ramping phase, the system gains inertia and can withstand greater electrical power imbalances. Thus, the plan energizes loads that would no longer cause a frequency violation, as seen around steps 30 and 60. Although this sequence takes longer to complete, it offers a practical and safe solution to grid recovery.

To validate the MILP-generated plan under more realistic conditions, the frequency-constrained sequence is re-evaluated in PSS/E. An identical 9-bus system is constructed in the simulation software as shown in Fig. 3.15. Fig. 3.16 shows the center-of-inertia frequency from the ASF swing equation.

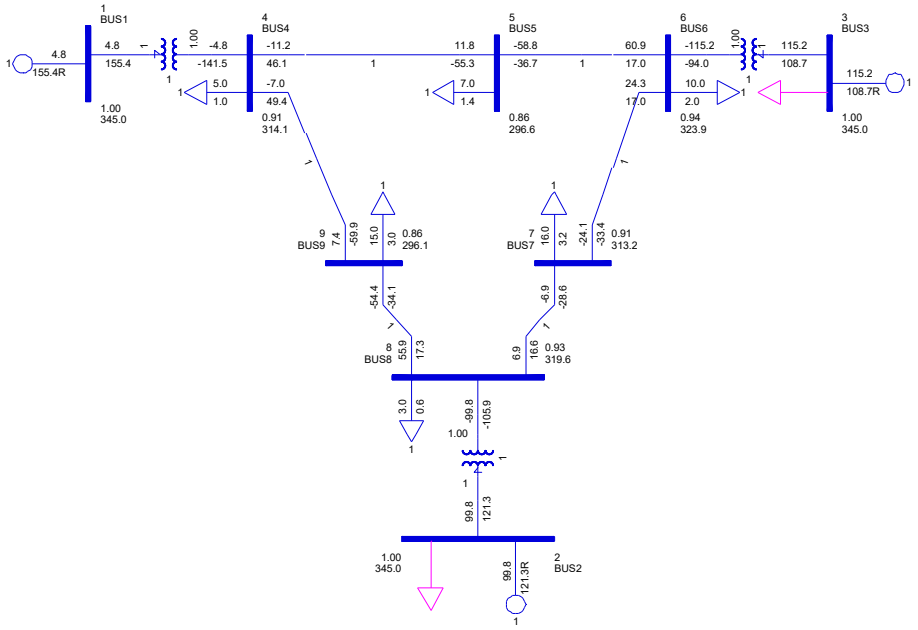

Figure 3.15: PSS/E model of the modified IEEE 9-bus system

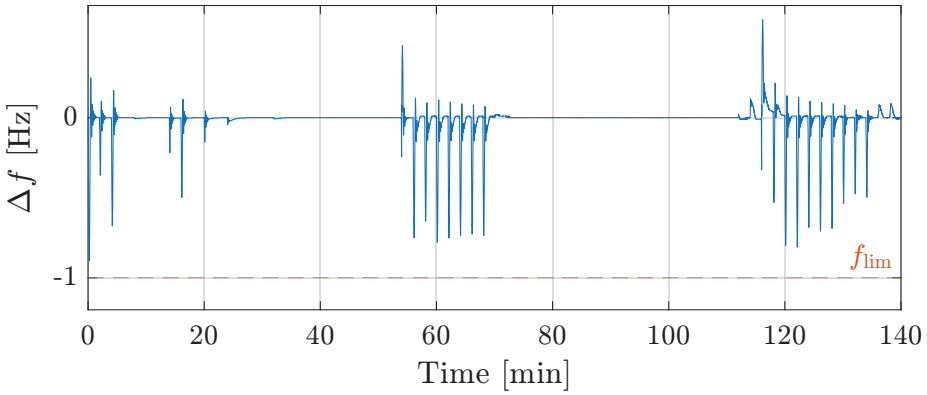

Figure 3.16: Center-of-inertia frequency profile of the frequency-constrained restoration plan obtained by PSS/E

Fig. 3.16 shows that all restoration actions meet the frequency nadir limit of 1 Hz, with minor differences from the MATLAB simulation (Fig. 3.14, bottom) that can be attributed to regional frequency behavior. These results demonstrate that the proposed method produces frequency-constrained restoration plans that remain valid under high-fidelity dynamic simulations.

Chapter 4

Energy Storage System (ESS) Participation

In this section, we investigate ways that ESS units can be used to facilitate the restoration effort. Storage devices can support restoration in two ways—by providing extra power capacity by discharging into the grid when necessary, and by providing frequency support through changes in their power setpoints. To address both applications, we introduce an ESS model into the MILP framework and integrate the changes in the ESS setpoints into the ramp-approximated frequency nadir constraint. The MILP model of the ESS is inspired by the one in [29]. In this work, we describe the logical coupling between variables in further detail and show how the model can be integrated into our frequency analysis from Section 3.2. Finally, we use a numerical example to demonstrate the effects of ESS participation.

4.1 ESS Modeling

4.1.1 Steady-state MILP Model

In a system with E energy storage systems (ESS), we define the binary variables $\boldsymbol{b}_{\mathrm{e}} \in \{0,1\}^{E\times T}$ and $\boldsymbol{b}_{\mathrm{e}}^{0} \in \{0,1\}^{E} = \boldsymbol{b}_{\mathrm{e}}(0)$ to represent their statuses. We also define the state of charge or energy stored in each device as $\boldsymbol{E}_{\mathrm{sto}} \in \mathbb{R}^{E\times T}$ and its initial value as $\boldsymbol{E}_{\mathrm{sto}}^{0} = \boldsymbol{E}_{\mathrm{sto}}(0) \in \mathbb{R}^{E}$. The storage devices have maximum capacities $\overline{\boldsymbol{E}}_{\mathrm{sto}}$ and cannot hold a negative charge.

$$0 \leq \boldsymbol{E}_{\mathrm{sto}}(k) \leq \overline{\boldsymbol{E}}_{\mathrm{sto}} \qquad \forall k \in \{1\ldots,T\} \tag{4.1}$$

Battery storage devices are inverter-based resources (IBRs), which means they are connected to the grid by a DC-AC converter [29]. Each ESS unit is configured as shown in Fig. 4.1. The power lost through the DC-AC converters and storage devices is captured by the efficiency vectors $\boldsymbol{\eta}_{\mathrm{con}}, \boldsymbol{\eta}_{\mathrm{sto}} \in [0,1]^{E}$, respectively, where $\boldsymbol{\eta}_{\mathrm{con}}$ is the efficiency of the power converters in both directions and $\boldsymbol{\eta}_{\mathrm{sto}}$ is the efficiency of the battery storage devices. We

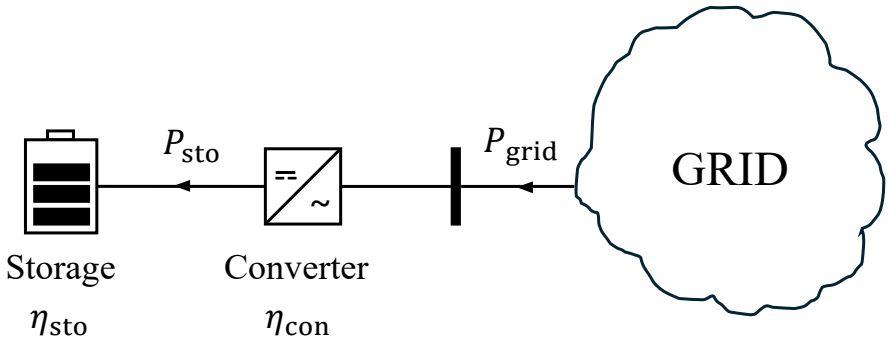

Figure 4.1: ESS grid interconnection

define $\boldsymbol{P}_{\text{sto}} \in \mathbb{R}^{E\times T}$ as the power flow to the battery device. When the battery is charged by an inflow P_{sto}, the actual power it receives is $\eta_{\text{sto}}P_{\text{sto}} \leq P_{\text{sto}}$. In contrast, a power outflow of P_{sto} requires the battery to discharge $\frac{P_{\text{sto}}}{\eta_{\text{sto}}} \geq P_{\text{sto}}$. The dependence on the direction of flow can be modeled by superposition, where the DC side's power flow is split into two nonnegative terms.

$$\boldsymbol{P}_{\text{sto}} = \boldsymbol{P}^{\text{in}}_{\text{sto}} - \boldsymbol{P}^{\text{out}}_{\text{sto}} \tag{4.2}$$

We then define binary variables attributed to each term as $\boldsymbol{b}_{\text{e,in}}, \boldsymbol{b}_{\text{e,out}} \in \{0,1\}^{E\times T}$, which turn on when $\boldsymbol{P}^{\text{in}}_{\text{sto}}$ and $\boldsymbol{P}^{\text{out}}_{\text{sto}}$ are nonzero, respectively. The binary variables act as indicators for the direction of the power flow on the DC side. The big M logical constraints

$$0 \leq \boldsymbol{P}^{\text{in}}_{\text{sto}} \leq M_{12}\boldsymbol{b}_{\text{e,in}} \tag{4.3a}$$

$$0 \leq \boldsymbol{P}^{\text{out}}_{\text{sto}} \leq M_{13}\boldsymbol{b}_{\text{e,out}} \tag{4.3b}$$

couples the continuous and binary variables and forces the directed power flows $\boldsymbol{P}^{\text{in}}_{\text{sto}}, \boldsymbol{P}^{\text{out}}_{\text{sto}}$ to be nonnegative. The battery cannot charge and discharge simultaneously, so only one of the two terms can be nonzero at any step. Furthermore, the battery is allowed to charge and discharge only after the ESS device has been restored. These two requirements can be represented in a single constraint as

$$\boldsymbol{b}_{\text{e,in}} + \boldsymbol{b}_{\text{e,out}} \leq \boldsymbol{b}_{\text{e}} \tag{4.4}$$

The ESS cannot be turned on unless its bus is active. A ESS-to-bus adjacency matrix $\mathbf{A}_{\text{e}} \in \{0,1\}^{B\times E}$ can be formed as defined in (3.3) and used in the constraint

$$\mathbf{A}_{\text{e}}\boldsymbol{b}_{\text{e}} \leq M_{14}\boldsymbol{b}_{\text{b}} \tag{4.5}$$

where $\mathbf{A}_{\text{e}}$ matches the indices of the ESS to their buses. Having defined the power flow

of the ESS unit, the update equation for the SoC is

$$\boldsymbol{E}_{\text{sto}}(k+1) = \boldsymbol{E}_{\text{sto}}(k) + 60t(\text{diag}(\boldsymbol{\eta}_{\text{sto}})\boldsymbol{P}^{\text{in}}_{\text{sto}} - \text{diag}(\boldsymbol{\eta}_{\text{sto}})^{-1}\boldsymbol{P}^{\text{out}}_{\text{sto}}) \tag{4.6}$$

where t is the time interval between each step of the MILP, in minutes. Due to the binary constraint (4.4), only one of $\boldsymbol{P}^{\text{in}}_{\text{sto}}$ and $\boldsymbol{P}^{\text{out}}_{\text{sto}}$ can be nonzero. Finally, the power balance constraint in (3.4) is updated to include the ESS power contribution at the grid connection.

$$\underbrace{\mathbf{A}_{\text{g}}\boldsymbol{P}_{\text{g}} - \mathbf{A}_{\text{d}}\,\text{diag}(\boldsymbol{P}_{\text{d}})\boldsymbol{b}_{\text{d}} - \mathbf{A}\boldsymbol{P}_{\text{l}}}_{\boldsymbol{P}_{\text{grid}}} + \text{diag}(\boldsymbol{\eta}_{\text{con}})\boldsymbol{P}^{\text{out}}_{\text{sto}} - \text{diag}(\boldsymbol{\eta}_{\text{con}})^{-1}\boldsymbol{P}^{\text{in}}_{\text{sto}} = 0 \tag{4.7}$$

The storage device has a rated power $\overline{\boldsymbol{P}}_{\text{sto}}$ that is enforced by the following constraint.

$$-\mathbb{1}^{\top}\overline{\boldsymbol{P}_{\text{sto}}} \leq \boldsymbol{P}_{\text{sto}} \leq \mathbb{1}^{\top}\overline{\boldsymbol{P}_{\text{sto}}} \tag{4.8}$$

The ESS also has a rate-of-change limit $\overline{\Delta\boldsymbol{P}}_{\text{sto}}$ on its power output during any step.

$$-\overline{\Delta\boldsymbol{P}}_{\text{sto}} \leq \boldsymbol{P}_{\text{sto}}(k+1) - \boldsymbol{P}_{\text{sto}}(k) \leq \overline{\Delta\boldsymbol{P}}_{\text{sto}} \qquad \forall k \in \{1, \ldots, T-1\} \tag{4.9}$$

As modeled in the MILP, excess available power from the grid can be stored in ESS devices and withdrawn when it can facilitate the restoration effort. For example, ESS devices can assist in load recovery when the system's remaining online capacity is low, or when the available units have slow ramp rates.

The complete formulation with ESS participation can be formed by introducing constraints (4.1), (4.3), (4.2) (4.4), (4.5), (4.6), (4.8), (4.9), and replacing (3.4) with (4.7).

4.1.2 Frequency response with ESS contribution

In the previous section, we described the steady-state model of the ESS with power outputs defined at each time step. The ESS are dispatched at the same time as the restorative actions are carried out. Since this dispatch is not instantaneous, $\boldsymbol{P}_{\text{sto}}$ describes the desired steady-state output of each ESS, which can be interpreted as a setpoint similar to those given to SGs by $\Delta\boldsymbol{P}_{\text{ref}}$.

In this section, we describe the dynamic behaviour of the ESS apparatus shown in Fig. 4.1 with a first-order transfer function with unity DC gain and time constant $\boldsymbol{\tau}$.

$$G_{\text{ess}}(s) = \frac{1}{1+s\tau}$$

The ESS receives a power setpoint $P^{\text{ref}}_{\text{ess}}$ simultaneously to an operator action that introduces a power imbalance ΔP_{e}. We again assume the system to be in steady state prior to each action. Since the swing equation (2.7) relates the frequency deviation to the net power imbalance, the *ESS setpoint updates* $\Delta P^{\text{ref}}_{\text{ess}}$ are integrated as

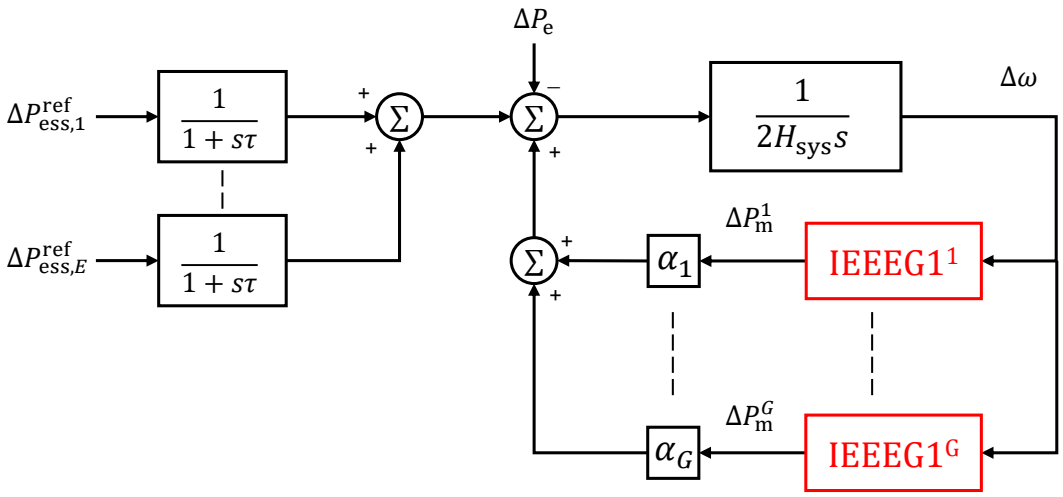

Figure 4.2: Full closed-loop swing equation with ESS support

$$\Delta\dot{\omega} = \frac{1}{2H_{\text{sys}}}\left(\sum_{i\in\mathcal{G}_{\text{po}}} \alpha^i \Delta P^i_{\text{m}} - \frac{\Delta P_{\text{e}}}{s} - \sum_{i\in\mathcal{G}_{\text{e}}} \Delta P^{\text{ref}}_{\text{ess,i}}\right) \tag{4.10}$$

where $\mathcal{G}_{\text{e}}$ is the set of active ESS devices, and $\Delta P^{\text{ref}}_{\text{ess,i}}$ defines the setpoint update of the ith ESS. The full ASF model with SG and ESS support is shown in Fig. 4.2. The goal of this simple ESS dynamic model is to describe a non-instantaneous (with time constant τ, dispatchable device from which power can be stored and retrieved. The model sheds some surprising insight into how such devices can coordinate with the restoration effort to improve recovery speed and reliability from both steady state and dynamic perspectives.

To derive the frequency nadir with ESS participation, we begin with a system with a single ESS device and zero system damping constant ($D_{\text{sys}} = 0$). The change in the ESS output to a step input $\frac{\Delta P^{\text{ref}}_{\text{ess}}}{s}$ can be written in the Laplace domain as

$$\Delta P_{\text{ess}} = \frac{1}{s(\tau s + 1)}\Delta P^{\text{ref}}_{\text{ess}}$$

The setpoint $\Delta P^{\text{ref}}_{\text{ess}}$ can be positive (discharging) or negative (charging). We introduce this new term to the ramp-approximated frequency expression from Eq. (3.35).

$$\Delta\omega(s) = \frac{1}{2H_{\text{sys}}s}\left(\frac{C_1}{s^2} + \frac{C_2}{s} + C_3 - \frac{\Delta P_{\text{e}}}{s} + \frac{\Delta P^{\text{ref}}_{\text{ess}}}{s(\tau s + 1)}\right) \tag{4.11}$$

where C_1, C_2, C_3 are constants derived from the IEEEG1 model. The final term in (4.11) can be expanded into first-order terms by partial fractions. Performing this expansion, collecting like terms and applying the inverse Laplace transform, the time-domain frequency

expression is found as

$$\Delta\omega(t) = \frac{1}{2H_{\text{sys}}}\left(\frac{C_1}{2}t^2 + (\Delta P_{\text{ess}}^{\text{ref}} - \Delta P_{\text{e}} - C_2)t + C_3 - \tau\Delta P_{\text{ess}}^{\text{ref}} + \tau\Delta P_{\text{ess}}^{\text{ref}} e^{-\frac{1}{\tau}t}\right)$$

We follow the procedure in Section 3.2.3 to find the frequency nadir as a function of the power imbalance ΔP_{e} and the ESS setpoint update $\Delta P_{\text{ess}}^{\text{ref}}$. However, the extra exponential term complicates the nadir time expression, which does not have a closed form if the system contains multiple ESS devices with different time constants. Instead, since the ESS devices are often much faster than the overall frequency dynamics, we assume that the exponential term becomes negligibly small when the nadir is reached. The elimination of the exponential yields the nadir time and frequency nadir as

$$\begin{aligned} t_{\text{nadir}} &= \frac{\Delta P_{\text{e}} + C_2 - \Delta P_{\text{ess}}^{\text{ref}}}{C_1} \\ \Delta\omega_{\text{nadir}} &= \frac{1}{2H_{\text{sys}}}\left(-\frac{(\Delta P_{\text{e}} + C_2 - \Delta P_{\text{ess}}^{\text{ref}})^2}{2C_1} + C_3 - \tau\Delta P_{\text{ess}}^{\text{ref}}\right) \end{aligned} \tag{4.12}$$

For a frequency limit of $-|\Delta\omega_{\text{lim}}|$, the maximum electrical imbalance can be found by isolating ΔP_{e} in (4.12) as

$$\Delta P_{\text{e}} \leq \sqrt{4H_{\text{sys}}C_1|\Delta\omega_{\text{lim}}| + 2C_1C_3 - 2C_1\tau\Delta P_{\text{ess}}^{\text{ref}}} - C_2 + \Delta P_{\text{ess}}^{\text{ref}} \tag{4.13}$$

The MILP framework requires linear expressions of the variables ΔP_{e} and $\Delta P_{\text{ess}}^{\text{ref}}$ to impose (4.13) as a constraint in the MILP framework. Observe that when $\Delta P_{\text{ess}}^{\text{ref}} = 0$, we recover the maximum load pick-up expression from Eq. (3.37).

$$(\Delta P_{\text{e,max}})_{\Delta P_{\text{ess}}^{\text{ref}}=0} = \sqrt{4H_{\text{sys}}C_1|\Delta\omega_{\text{lim}}| + 2C_1C_3} - C_2$$

Eq. (4.13) can be linearized around this operating point to obtain

$$\begin{aligned} \Delta P_{\text{e,max}} &\approx (\Delta P_{\text{e,max}})_{\Delta P_{\text{ess}}^{\text{ref}}=0} + \Delta P_{\text{ess}}^{\text{ref}}\left(\frac{d\Delta P_{\text{e,max}}}{d\Delta P_{\text{ess}}^{\text{ref}}}\right)_{\Delta P_{\text{ess}}^{\text{ref}}=0} \\ &\approx \underbrace{\sqrt{4H_{\text{sys}}C_1|\Delta\omega_{\text{lim}}| + 2C_1C_3} - C_2}_{\text{max load without ESS participation}} + \underbrace{\Delta P_{\text{ess}}^{\text{ref}}\left(1 - \frac{2C_1\tau}{2\sqrt{4H_{\text{sys}}C_1|\Delta\omega_{\text{lim}}| + 2C_1C_3}}\right)}_{\text{effect of ESS setpoint change}} \\ &= \Delta P_{\text{e,max,0}} + g_{\text{ess}}\Delta P_{\text{ess}}^{\text{ref}} \end{aligned} \tag{4.14}$$

With no ESS participation, the maximum safe power imbalance $\Delta P_{\text{e,max,0}}$ is identical to that in Eq. (3.37). The second term in (4.14) accounts for the frequency support by the ESS, where $0 < g_{\text{ess}} < 1$ is a sensitivity term that describes how $\Delta P_{\text{e,max}}$ changes with the ESS setpoint update $\Delta P_{\text{ess}}^{\text{ref}}$. For every 1 unit of increase in the setpoint, the bound on the power

imbalance increases by g_{ess}. The net power shortage caused by load pick-ups ($\Delta P_{\text{e}} > 0$) is offset by an increase in ESS output. Since we model load pick-ups as step changes and ESS output as non-instantaneous changes, $g_{\text{ess}} < 1$, which indicates that the ESS is unable to completely offset step imbalances. The sensitivity g_{ess} is proportional to the time constant τ, and a faster ESS has a greater influence on the maximum power imbalance.

Equation (4.14) also captures the effect of charging the ESS on grid frequency. A negative $\Delta P_{\text{ess}}^{\text{ref}}$ reduces the maximum safe imbalance because it contributes to a decrease in system frequency. When $\Delta P_{\text{e,max}} = 0$, which means that no load pick-ups of any size can occur, we find that

$$\Delta P_{\text{ess}}^{\text{ref}} = -\frac{\Delta P_{\text{e,max},0}}{g_{\text{ess}}} \tag{4.15}$$

which is an implicit bound on how much the ESS setpoint can decrease. Eq. (4.14) can be generalized to systems with multiple ESS units, as well as a nonzero damping constant.

$$\begin{aligned}\Delta P_{\text{e,max}} &= \underbrace{-\frac{2H_{\text{sys}}C_1}{D_{\text{sys}}}\left(w_{-1}+1+\frac{C_3D_{\text{sys}}^2}{4H_{\text{sys}}^2C_1}+\frac{C_2D_{\text{sys}}}{2H_{\text{sys}}C_1}\right)}_{\text{max load without ESS participation}} \\ &\quad + \underbrace{\sum_i^E\left(\frac{2H_{\text{sys}}}{2H_{\text{sys}}-D_{\text{sys}}\tau_i}\left(1-\frac{D_{\text{sys}}\tau_i}{2H_{\text{sys}}}\left(\frac{w_{-1}}{1+w_{-1}}\right)\right)\Delta P_{\text{ess}}^{\text{ref},i}\right)}_{\text{combined effect of ESS setpoint changes}} \\ &= \Delta P_{\text{e,max},0} + \sum_i^E g_{\text{ess}}^i \Delta P_{\text{ess}}^{\text{ref},i}\end{aligned} \tag{4.16}$$

where w_{-1} is a constant obtained from the Lambert W function, and $\tau_i, \Delta P_{\text{ess}}^{\text{ref},i}$ are the time constant and setpoint update of the ith ESS device. Please see Appendix E for the full derivation.

In the MILP, the ESS setpoints correspond to the steady-state output as seen from the grid, which is the injection through the AC side of the converters. In the notation of the MILP, let $\boldsymbol{\Delta P}_{\text{ess}}^{\text{ref}} \in \mathbb{R}^{E\times T}$ contain setpoints changes of all ESS devices for T time steps, defined for all $k \in \{1,\dots,T\}$

$$\boldsymbol{\Delta P}_{\text{ess}}^{\text{ref}}(k) = \text{diag}(\boldsymbol{\eta}_{\text{con}})(\boldsymbol{P}_{\text{sto}}^{\text{out}}(k) - \boldsymbol{P}_{\text{sto}}^{\text{out}}(k-1)) - \text{diag}(\boldsymbol{\eta}_{\text{con}})^{-1}(\boldsymbol{P}_{\text{sto}}^{\text{in}}(k) - \boldsymbol{P}_{\text{sto}}^{\text{in}}(k-1)) \tag{4.17}$$

where $\boldsymbol{P}_{\text{sto}}^{\text{out}}(0), \boldsymbol{P}_{\text{sto}}^{\text{in}}(0)$ are steady-state ESS inflows and outflows before restoration begins. Constraint (4.14) can be written at any time step $k \in \{1,\dots,T\}$ as

$$\boldsymbol{\Delta P}_{\text{e,max}}(k) = \boldsymbol{\Delta P}_{\text{e,max},0}(k) + \boldsymbol{g}_{\text{ess}}^{\top}\,\boldsymbol{\Delta P}_{\text{ess}}^{\text{ref}}(k) \tag{4.18}$$

where $\boldsymbol{\Delta P}_{\text{e,max},0} \in \mathbb{R}^{1\times T}$ is the vector of the maximum power imbalance without ESS participation at each time step, and $\boldsymbol{g}_{\text{ess}} \in \mathbb{R}^{E\times T}$ contains gradient vectors that represent the sensitivities of the maximum imbalance to each ESS device's output at each time step. Both can be obtained by Algorithm 2 and appear in the MILPs as constant vectors/matrices. The linear constraint (4.18) replaces (3.48) in the MILP to enforce the frequency nadir limit.

4.2 Case Study: ESS Participation

First, we examine the accuracy of the linearized constraint (4.14). In Fig. 4.3, the linearized relation between the ESS setpoint updates $\boldsymbol{\Delta P}^{\text{ref}}_{\text{ess}}$ and the maximum allowable power imbalance $\boldsymbol{\Delta P}_{\text{e,max}}$ is compared to their exact nonlinear relation. The parameters of the IEEE 9-bus system are used with all synchronous machines online, and two cases are plotted with different ESS time constants.

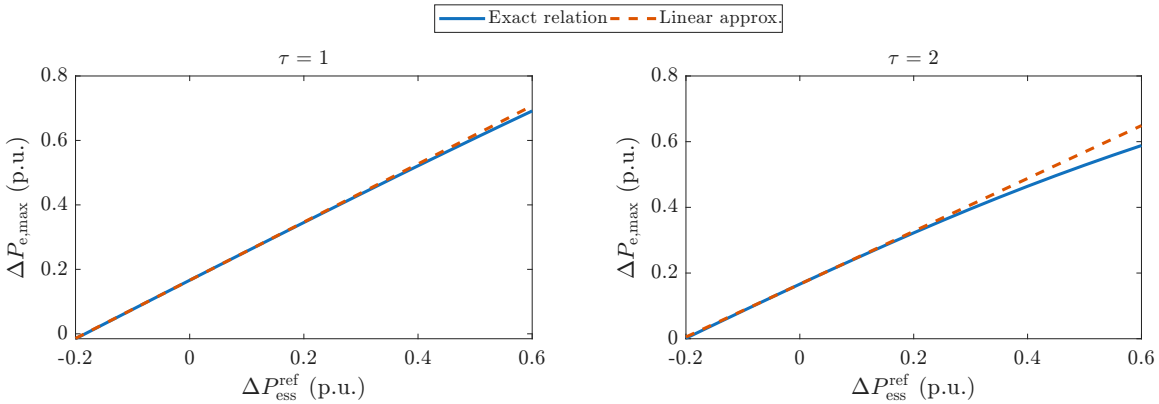

Figure 4.3: Effect of ESS reference point updates on the maximum power imbalance

In both cases, the affine relation remains above the exact curve. This means that the ability of the ESS outputs to expand the safe range of imbalances is overestimated. The errors become larger as the ESS setpoint update increases. Errors also grow larger when the time constant τ is slower, due to the derivation assuming a fast decay of the $e^{-\frac{1}{\tau}t}$ term. When ESS devices are slower to track their setpoints, their ability to provide frequency support is reduced. The linear constraint is also able to capture the effect of ESS charging, which reduces the size of the allowable imbalance.

The IEEE 9-bus test system from Section 3.4 is used to examine how ESS can participate in restoration. An ESS device is added to bus 5 with the parameters displayed in Table 4.1. The frequency nadir constraints (4.18), containing the ESS power setpoints, are inserted into the MILP and solved using the IRSC algorithm. With a frequency nadir limit of 1 Hz, the frequency profile of the optimal restoration plan with ESS participation is shown in 4.4.

In contrast to the frequency-secure plan without the ESS device in (Fig. 3.14, bottom), the plan does not wait until the NBSUs are synchronized. Rather, the plan uses the ESS setpoints to offset the imbalances caused by larger load pick-ups. The relation in (4.18) allows

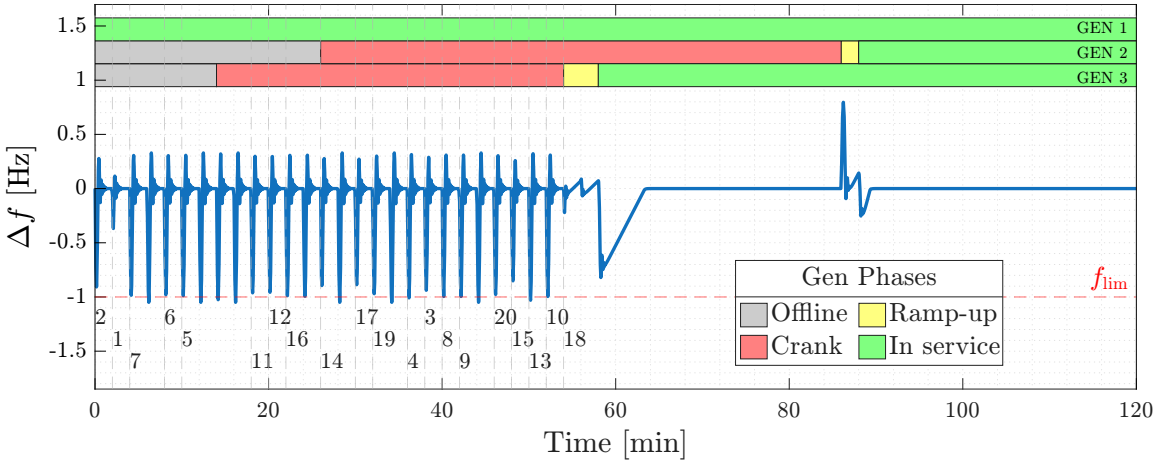

Figure 4.4: Frequency during the optimal restoration sequence with ESS support

$\overline{\boldsymbol{E}}_{\text{sto}}$ [MJ]	$\overline{\boldsymbol{P}}_{\text{sto}}$ [MW]	$\overline{\boldsymbol{\Delta P}}_{\text{sto}}$ [MW]	$\boldsymbol{\tau}$ [s]	$\boldsymbol{\eta}_{\text{sto}}$	$\boldsymbol{\eta}_{\text{con}}$
6000	20	20	1	1	1

Table 4.1: Parameters of the ESS on bus 3 in the modified IEEE 9-bus system

the ESS setpoints to enable larger load pick-ups without violating the nadir constraint. The plan recommends that the ESS is charged in between load pick-ups to remain available to assist future actions. The nadirs at some time steps slightly violate the 1 Hz constraint and are caused by the optimistic nature of both the ramp approximation and the linearized ESS relationship. Since the optimal strategy involves actions that cause a frequency nadir of exactly 1 Hz, approximation errors may cause slight violations. This can be addressed by adjusting the input $\Delta\omega_{\text{lim}}$ of the MILP to include a margin of safety.

The ESS power setpoints and SoC during the restoration process are shown in Fig. 4.5. When frequency support from the ESS is needed, the setpoint is increased from the previous

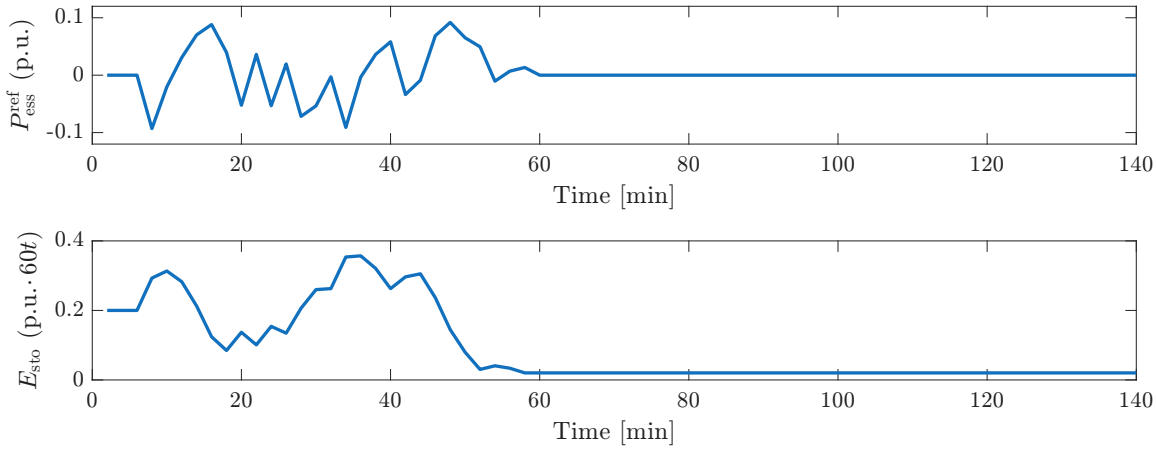

Figure 4.5: Power reference points and SoC of the ESS device during restoration

time step. However, because the ESS has a limited power rating and SOC, the setpoint needs to be lowered during subsequent steps so that 1) it can be increased again and 2) the device has enough charge to sustain an output at the increased setpoint. If fluctuation of the ESS output is undesirable, it can be limited by using tighter limits on (4.9) or by introducing additional constraints, such as forcing the device to charge or discharge for a sustained period.

Chapter 5

Future Work and Conclusion

In this chapter, we first present some extensions to the frequency-constrained MILP framework, many of which are ongoing research topics in this project that are incomplete due to time limitations. For each topic, we briefly show candidate approaches and suggest possible next steps. Finally, we draw some general conclusions based on our findings and summarize the strengths and limitations of our methodology.

5.1 Future Directions

5.1.1 Voltage and Reactive Power Modeling

In addition to frequency security, voltage security is another prime concern during restoration. The energization of network elements can cause voltage fluctuations and transients, especially in weaker systems. In particular, charging long transmission lines with little or no load on the other end can cause large voltage rises [5]. This phenomenon is known as the Ferranti effect and can also occur through lines with capacitive compensation that are designed for normal operating conditions.

DCPF is adopted in this work as a linearized power flow constraint in the MILP. However, the approximation neglects voltage magnitudes and reactive power flow. Thus, a clear extension involves adding voltage and reactive power constraints. We will show how the Q-V relationship derived in Section 2.1 can be integrated.

Let $\boldsymbol{Q}_{\mathrm{l}} \in \mathbb{R}^{L \times T}$ and $\boldsymbol{Q}_{\mathrm{g}} \in \mathbb{R}^{G \times T}$ represent the reactive line flows and the reactive generator outputs at all time steps.

$$\boldsymbol{Q}_{\mathrm{l}} = \begin{bmatrix} \boldsymbol{Q}_{\mathrm{l}}(1) & \boldsymbol{Q}_{\mathrm{l}}(2) & \dots & \boldsymbol{Q}_{\mathrm{l}}(T) \end{bmatrix}$$
$$\boldsymbol{Q}_{\mathrm{g}} = \begin{bmatrix} \boldsymbol{Q}_{\mathrm{g}}(1) & \boldsymbol{Q}_{\mathrm{g}}(2) & \dots & \boldsymbol{Q}_{\mathrm{g}}(T) \end{bmatrix}$$

The reactive power balance condition on each bus is analogous to the active power

balance condition (2.3).

$$\mathbf{A}_{\mathrm{g}}\boldsymbol{Q}_{\mathrm{g}} - \mathbf{A}_{\mathrm{d}}\,\mathrm{diag}(\boldsymbol{Q}_{\mathrm{d}})\boldsymbol{b}_{\mathrm{d}} + \boldsymbol{\beta}_{\mathrm{s}} = \mathbf{A}\boldsymbol{Q}_{\mathrm{l}}$$

where $\boldsymbol{\beta}_{\mathrm{s}} \in \mathbb{R}^{B}$ is a vector of shunt reactances. In this model, the reactive power flows between the sending and receiving ends are equal and depend on the differences of the bus voltages $\boldsymbol{V} \in \mathbb{R}^{B\times T}$. The definition in (2.4) can be vectorized as

$$\begin{aligned} -M(\mathbb{1} - \boldsymbol{b}_{\mathrm{l}}) \leq \boldsymbol{Q}_{\mathrm{l}} - \mathbf{X}^{-1}\mathbf{A}^{\top}\boldsymbol{V} \leq M(\mathbb{1} - \boldsymbol{b}_{\mathrm{l}}) \\ -M\boldsymbol{b}_{\mathrm{l}} \leq \boldsymbol{Q}_{\mathrm{l}} \leq M\boldsymbol{b}_{\mathrm{l}} \end{aligned}$$

where the matrix of bus voltage magnitudes $\boldsymbol{V} \in \mathbb{R}^{B\times T}$ must fall within a safe range $[\underline{\boldsymbol{V}}, \overline{\boldsymbol{V}}]$ for all time steps.

$$\mathrm{diag}(\underline{\boldsymbol{V}})\,\boldsymbol{b}_{\mathrm{b}} \leq \boldsymbol{V} \leq \mathrm{diag}(\overline{\boldsymbol{V}})\,\boldsymbol{b}_{\mathrm{b}} \tag{5.1}$$

On inactive buses, the voltage magnitudes are set to zero. The voltage on the slack (BSU) bus is assumed to be unity throughout restoration.

$$\boldsymbol{V}^{1}(k) = 1 \qquad \forall k \in \{0, \ldots, T\}$$

$\boldsymbol{Q}_{\mathrm{g}}$ can be defined for the four phases of generator start-up depending on the desired model. Additional constraints associated with voltage and reactive power can be defined, such as line current limits. Although this model provides a linear relation between the reactive power flows and bus voltages, its accuracy relies on the assumption of bus voltages are close to unity per unit values, which may not hold particularly for weaker grid connections, which appear more commonly during the restoration process. Other linear models of reactive power should be explored as a continuation of this work. Furthermore, dynamic voltage limits may be introduced by analyzing the exciter systems of the SGs. These extensions outline an avenue for future extensions to the MILP restoration framework.

5.1.2 Fast Frequency Response and Variable Renewable Energy Participation

In this work, we showed that ESS setpoint adjustments can facilitate frequency regulation during restoration. Another way for ESS devices to provide frequency support is through an FFR feedback loop, which automatically adjusts power output according to a detected frequency deviation. The ESS model in this work can be extended to provide FFR services.

The FFR model in Section 3.2.4 includes proportional and derivative components of the frequency deviation. The work from [45] showed that the effect of FFR can be aggregated into inertia and damping constants. In the MILP, some additional constraints are required to integrate FFR. That is, the ESS must have enough stored energy and power capacity

to provide FFR. The ramp approximation, valid up to the nadir time, may be used to estimate the energy and maximum output during the FFR. For instance, it can be shown that the maximum FFR power is always achieved before the nadir, allowing the use of the ramp-approximate expressions. Further derivation and validation are required to incorporate ESS-supplied FFR to the MILP framework.

Finally, ESS devices are often adjacent to variable renewable energy (VRE) resources such as utility-level solar or wind plants. This work can be extended to investigate VRE participation in restoration. A combined ESS-VRE model is shown in Fig. 5.1, where the renewable source is connected to the DC end of the converter.

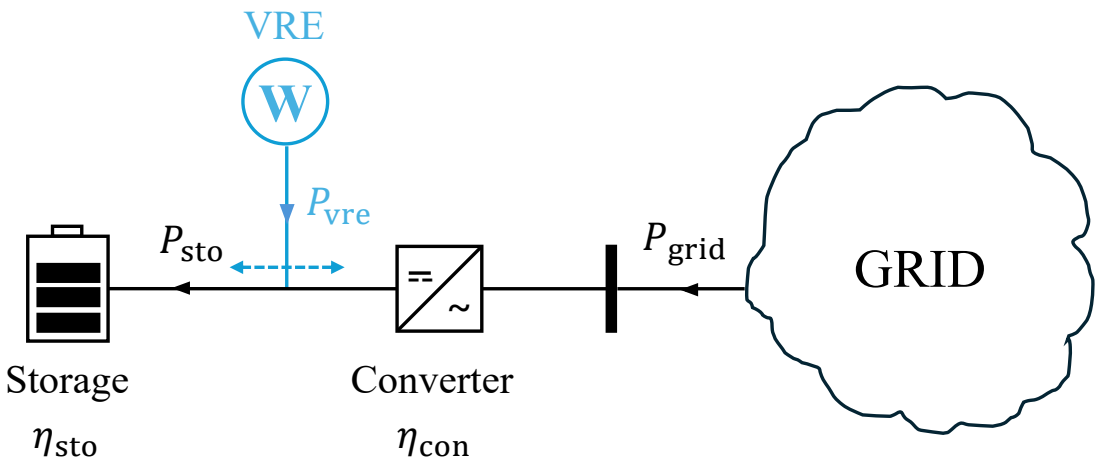

Figure 5.1: Grid interconnection of a hybrid ESS-VRE system

The VRE can be used to charge the ESS device or supply power to the grid. A superposition method can be used, similar to how the ESS power output is formulated in Section 4.1.1. The total output P_{vre} can be divided into two positive components that represent flows in each direction.

$$P_{\text{vre}} = P_{\text{vre}}^{\text{in}} + P_{\text{vre}}^{\text{out}} \qquad P_{\text{vre}}^{\text{in}}, P_{\text{vre}}^{\text{out}} \geq 0 \tag{5.2}$$

The variable P_{vre} can be modeled deterministically using forecast data or as random variables, leading to many approaches such as robust constraints or chance constraints.

5.2 Conclusion

In this work, we synthesized a frequency-constrained MILP for optimal black-start restoration planning of transmission systems. We focus on the generator and load recovery phases and seek a sequence of frequency-secure operator actions that expedites system recovery. The core of this work can be summarized by its three components—MILP formulation,

dynamic frequency analysis, and the iterative parameter prediction algorithm. Furthermore, an extension involving ESS contributions is presented that fits seamlessly into the framework.

In Section 3.1, a discrete-time MILP for restoration planning is introduced. We show how the logical coupling between binary and continuous variables can be resolved using the big M method. The MILP integrates both the generator and load recovery phases and smoothly transitions between them using a weighted objective function. Another strength of the framework is its flexibility—the objective function allows the priority of each network component to be adjusted as required by the operator. Furthermore, many other network and equipment conditions, such as critical start-up times of generators and dynamic reserve constraints, can be described by mixed-integer linear constraints.

One key limitation to the current framework is its use of the DCPF equations, which neglect bus voltage magnitudes and reactive power transfer. During restoration, the weak recovering system may cause abnormal voltage levels that cause the DCPF assumptions to fail. More detailed linear power flow models would improve the overall modeling accuracy and allow for voltage constraints to be introduced. A candidate voltage model is described in Section 5.1.1. Another limitation of the current work is its static load model. First, the power consumption of loads in actual systems is dynamic and can vary over time due to changes in demand and system conditions. In conjunction with a power flow model that does not neglect voltage magnitudes, a more detailed load model, such as the ZIP model, can be used to model the dependence of loads on voltage. Furthermore, changes in demand during the restoration period can be captured by a deterministic model relying on forecasted values, or an uncertain model to account for a range of demands. Developing models that are more representative of the actual system allows the restoration tool to produce plans with improved performance.

In Section 3.2, we analyze the IEEEG1 governor-turbine model and its PFR behavior. Using knowledge of power imbalance magnitudes and timing during restoration, we devised an approach to adjust generator setpoints to improve the system's frequency response. The setpoint changes inspired the ramp approximation, an open-loop approximation of the PFR feedback, which can be used to estimate the frequency nadir following step disturbances. In Section 3.3, we integrate the nadir as a constraint on the magnitude of load pick-up and generator cranking using an iterative receding-horizon algorithm. The frequency-constrained framework improves on the heuristic approaches of the current ISO restoration plans by strictly outlining which actions are permissible with respect to the frequency nadir bound. In addition, (3.36) predicts the value of the nadir for any given power imbalance, providing more knowledge to operators about how their actions can affect the system. The parameter updating concept of Algorithm 2 has broader applications for any receding horizon problem with parameters that depend on decision variables from previous time steps. In the IRSC algorithm, the predictions of the online generator set converts the frequency constraint (3.48) into a linear inequality. The predictions are made by assuming that no other generators are

started during the time horizon, an assumption that is more accurate for shorter horizons. The loss of accuracy of the parameter predictions for future steps is compensated for by saving only the next immediate action in each MILP solution.

Restoration plans from the frequency-constrained framework are illustrated numerically in Section 3.4. We demonstrate that without considering frequency, the optimization problem produces plans with large frequency swings that cannot be applied to real systems. The same problem may undermine other optimization-based planning tools in the literature that do not account for frequency dynamics. In contrast, the frequency-constrained sequence satisfies the operator-defined safe limit and gives insight into the system frequency behavior. The constraints are shown to effectively bound the frequency nadir with negligible magnitudes of error.

In Chapter 4, the MILP framework is extended to include contributions from ESS devices. ESS models are introduced to the static MILP model and the dynamic frequency nadir prediction model. We show that ESS can be dispatched to facilitate the restoration effort in two major ways, by acting as a power bank and by providing frequency support. First, if a low system inertia prohibits further action until more SGs are synchronized, the ESS devices can be charged to later provide additional power. More surprisingly, we demonstrate that by adjusting the setpoints of the ESS, the frequency nadir can be reduced to allow larger load pick-ups. The numerical results indicate that restoration can be accelerated by increasing and decreasing the ESS setpoints. Perhaps unintuitively, this may involve charging the devices prior to restoring larger loads so that their power outputs can be increased in subsequent steps.

Appendix A

Optimal Selection of Big M Constants

As discussed in Section 3.1.2, the M constants are best selected to give tight bounds when they are active. Here we give the tightest values of each M_i constant that appear in this work.

M_1 appears in (3.6). Phase angles in power systems are typically defined in the range $[-\frac{\pi}{2}, \frac{\pi}{2}]$, Active and reactive line flows depend on phase differences, which are in the range $[-\pi, \pi]$.

$$M_1 = \frac{\pi}{2}$$

M_2 appears in (3.8a). M_2 is active when a line is de-energized and bounds the power that would flow through the line if it were energized. Active power flow is maximized when the phase difference is $\frac{\pi}{2}$ and is greater through lines with smaller reactances.

$$M_2 = \frac{\pi}{2} \min_i(X_i)$$

M_3 appears in (3.8b). M_3 bounds the active line flows and can be chosen equal to M_2

$$M_3 = \frac{\pi}{2} \min_i(X_i)$$

M_4 appears in (3.12a). M_4 bounds the number of loads on any bus.

$$M_4 = \max(\mathbf{A}_{\mathrm{d}}\, \mathbb{1}^D)$$

M_5 appears in (3.12a). M_5 bounds the number of generators on any bus.

$$M_5 = \max(\mathbf{A}_{\mathrm{g}}\, \mathbb{1}^G)$$

M_6 appears in (3.17a). M_6 is active outside the cranking phase and bounds the difference

between the cranking power and the output power.

$$M_6 = \max(\overline{\boldsymbol{P}_{\mathrm{g}}} + \boldsymbol{P}_{\mathrm{c}})$$

M_7 appears in (3.17b). M_7 is active outside the ramping phase and bounds the difference between the ramping reference signal $\boldsymbol{P}_{\mathrm{r}}$, which is fixed at $-\frac{1}{2}\boldsymbol{r}$, and the output power.

$$M_7 = \max(\overline{\boldsymbol{P}_{\mathrm{g}}} + \frac{1}{2}\boldsymbol{r})$$

M_8 appears in (3.17c). M_8 bounds the difference between the output power and its upper and lower limits. This is maximized during the cranking phase, as the output power becomes negative.

$$M_8 = \max(\underline{\boldsymbol{P}_{\mathrm{g}}} + \boldsymbol{P}_{\mathrm{c}})$$

M_9 appears in (3.18a). M_9 bounds the difference between the ramp reference signal and $\frac{1}{2}\boldsymbol{r}$, which is maximized just before the ramping phase ends.

$$M_9 = \max(\mathrm{diag}(\boldsymbol{r})(\boldsymbol{T}_{\mathbf{r}} - \mathbf{1}))$$

M_{10} appears in (3.18b). M_{10} bounds the change in the ramp reference signal and ramp rate. This is maximized immediately after the ramping phase, when the reference signal is reset to $-\frac{1}{2}\boldsymbol{r}$.

$$M_{10} = \max(\boldsymbol{r} + \underline{\boldsymbol{P}_{\mathrm{g}}})$$

M_{11} appears in (3.19). M_{11} bounds the difference between the ramp rate and the change in generator output outside the online phase. This is maximized at the onset of the cranking phase.

$$M_{11} = \max(\boldsymbol{P}_{\mathrm{c}} - \frac{1}{2}\boldsymbol{r})$$

M_{12} appears in (4.3a). M_{12} bounds the maximum power inflow of the storage system.

$$M_{12} = \max(\overline{\boldsymbol{P}_{\mathrm{sto}}})$$

M_{13} appears in (4.3b). M_{13} bounds the maximum power outflow of the storage system.

$$M_{13} = \max(\overline{\boldsymbol{P}_{\mathrm{sto}}})$$

M_{14} appears in (4.5). M_{14} bounds the number of ESS units on any bus.

$$M_5 = \max(\mathbf{A}_{\mathrm{e}}\,\mathbb{1}^E)$$

Appendix B

Steady State PFR Values of SGs

For a positive power imbalance $\Delta P_{\mathrm{e}} > 0$ (shortage), synchronous generators provide PFR to stop the decline of system frequency. When the transients settle, the frequency will stabilize to a steady-state value below its nominal value, denoted by $\Delta\omega_{\mathrm{ss}}$. The PFR output of each participating machine during steady state can be defined by the DC gain of the ith IEEEG1 turbine-governor, which is K_i.

$$\Delta P^i_{\mathrm{m,ss}} = K_i \Delta\omega_{\mathrm{ss}}$$

At steady state, the swing equation from (2.5) becomes

$$\frac{1}{2H_{\mathrm{sys}}} \left(\sum_i^{G_{\mathrm{p}}} \alpha^i \Delta P^i_{\mathrm{m,ss}} - \Delta P_{\mathrm{e}} \right) = 0$$

Substituting the expression for $P^i_{\mathrm{m,ss}}$, we can solve for the steady-state frequency deviation and the PFR output of each unit.

$$\begin{aligned}
&\sum_i^{G_{\mathrm{p}}} \alpha^i K_i \Delta\omega_{\mathrm{ss}} - \Delta P_{\mathrm{e}} = 0 \\
&\Delta\omega_{\mathrm{ss}} = \frac{\Delta P_{\mathrm{e}}}{\sum_{i=1}^{G_{\mathrm{p}}} K_i \alpha^i} \\
&\Delta P^i_{\mathrm{m}} = \frac{K_i \Delta P_{\mathrm{e}}}{\sum_{i=1}^{G_{\mathrm{p}}} K_i \alpha^i} \qquad \forall i \in \{1, \ldots, G_{\mathrm{p}}\}
\end{aligned}$$

which gives the relation from (3.22).

Appendix C

Consistency of Maximum Imbalance With Damping

In this section, we prove (3.41), which states that the maximum safe power imbalance of nonzero damping converges to that of zero damping as $D_{\text{sys}} \to 0$. We begin by simplifying the limit.

$$\begin{aligned}
\Delta P_{\text{e,max}} &= \lim_{D_{\text{sys}} \to 0} -\frac{2H_{\text{sys}}C_1}{D_{\text{sys}}} \left(w_{-1} + 1 + \frac{D_{\text{sys}}C_2}{2H_{\text{sys}}C_1} + \frac{D_{\text{sys}}^2 C_3}{4H_{\text{sys}}^2 C_1} \right) \\
&= -2H_{\text{sys}}C_1 \lim_{D_{\text{sys}} \to 0} \left(\frac{w_{-1}+1}{D_{\text{sys}}} + \frac{D_{\text{sys}}C_3}{2H_{\text{sys}}} \right) - C_2 \\
&= -2H_{\text{sys}}C_1 \lim_{D_{\text{sys}} \to 0} \frac{w_{-1}+1}{D_{\text{sys}}} - C_2
\end{aligned}$$

w_{-1} is the some value given by the lower branch of the Lambert W function.

$$w_{-1} = W\left(-\exp\left(-\frac{D_{\text{sys}}^2 \left|\omega_{\text{lim}}\right|}{2H_{\text{sys}}C_1} - \frac{D_{\text{sys}}^2 C_3}{4H_{\text{sys}}^2 C_1} - 1 \right) \right)$$

Outlined in [49], the lower branch has a series expansion of form

$$W_{-1}\left[-\exp\left(-\frac{x^2}{2} - 1 \right) \right] = -\sum_{n \geq 0} a_n x^n$$

for some constants $a_0 = a_1 = 1$ and recursively defined $a_{n \geq 2}$. In our case, we can express w_{-1} as

$$w_{-1} = W_{-1}\left(-\exp\left(-\frac{1}{2}\left(D_\Sigma \sqrt{\frac{\left|\omega_{\text{lim}}\right|}{H_\Sigma C_1} + \frac{C_3}{2H_\Sigma^2 C_1}} \right)^2 - 1 \right) \right)$$

and use the series expansion in the expression for the maximum imbalance.

$$
\begin{aligned}
\Delta P_{\mathrm{e,max}} &= -2H_{\mathrm{sys}}C_1 \lim_{D_{\mathrm{sys}}\to 0} \frac{w_{-1}+1}{D_{\mathrm{sys}}} - C_2 \\
&= -2H_{\mathrm{sys}}C_1 \lim_{D_{\mathrm{sys}}\to 0} \frac{1}{D_{\mathrm{sys}}} \left(1 - a_0 - a_1 D_{\mathrm{sys}} \sqrt{\frac{|\omega_{\mathrm{lim}}|}{H_{\mathrm{sys}}C_1} + \frac{C_3}{2H_{\mathrm{sys}}^2 C_1}} - a_2 D_{\mathrm{sys}}^2(\cdots) \right) - C_2 \\
&= 2H_{\mathrm{sys}}C_1 \sqrt{\frac{|\omega_{\mathrm{lim}}|}{H_{\mathrm{sys}}C_1} + \frac{C_3}{2H_{\mathrm{sys}}^2 C_1}} - C_2 \\
&= \sqrt{|4H_{\mathrm{sys}}C_1\omega_{\mathrm{lim}}| + 2C_1C_3} - C_2
\end{aligned}
$$

which is the maximum power imbalance when the damping constant is zero. The proof is complete.

Appendix D

Modified IEEE 9-Bus System Parameters

Line #	From bus	To bus	Reactance [p.u.]
1	1	4	0.0576
2	4	5	0.092
3	5	6	0.17
4	3	6	0.0586
5	6	7	0.1008
6	7	8	0.072
7	8	2	0.0625
8	8	9	0.161
9	9	4	0.085

Table D.1: Branch information of the modified IEEE 9-bus system

Bus #	Loads [MW]
4	[5, 8, 10]
5	[7, 12, 15, 13]
6	[10, 10, 10]
7	[16, 15]
8	[3, 13, 9, 12]
9	[6, 10, 16]

Table D.2: Load information of the modified IEEE 9-bus system

Bus #	$\underline{P_g}$ [MW]	$\overline{P_g}$ [MW]	P_c [MW]	T_c [min]	r [%cap/min]
1	0	247.5	0	0	10
2	38.4	192	9.6	60	10
3	25.6	128	3.84	40	5

Table D.3: Generator start-up parameters for the modified IEEE 9-bus system

Bus #	H [s]	T_1	T_2	T_3	T_4	T_5	T_6	T_7	K	K_1	K_3	K_5	K_7
1	5.55	4	8	0.2	0.2	0.12	0.12	0.15	20	0.4	0.2	0.2	0.2
2	4.33	4	8	0.2	0.2	0.12	0.12	0.15	20	0.4	0.2	0.2	0.2
3	3.35	4	8	0.2	0.2	0.12	0.12	0.15	20	0.4	0.2	0.2	0.2

Table D.4: Generator dynamic parameters for the modified IEEE 9-bus system

w

Appendix E

ESS-supported Power Imbalance Bound With Nonzero Damping

This section derives (4.16), the maximum safe power imbalance with ESS participation. To begin, the ramp-approximated frequency for nonzero damping in the Laplace-domain is

$$\Delta\omega(s) = \frac{1}{2H_{\text{sys}}s + D_{\text{sys}}}\left(\frac{C_1}{s^2} + \frac{C_2}{s} + C_3 - \frac{\Delta P_{\text{e}}}{s} + \sum_i^E \frac{\Delta P_{\text{ess}}^{\text{ref},i}}{s(\tau_i s + 1)}\right)$$

All terms can be expanded using partial fractions. For notational concision, let

$$\beta = 4H_{\text{sys}}^2 C_1 + 2D_{\text{sys}}H_{\text{sys}}(\Delta P_{\text{e}} + C_2) + C_3 D_{\text{sys}}^2$$
$$\gamma = \sum_i^E \frac{\Delta P_{\text{ess}}^{\text{ref},i}}{2H_{\text{sys}} - D_{\text{sys}}\tau_i}$$

The expanded frequency expression becomes

$$\Delta\omega(s) = \frac{C_1}{D_{\text{sys}}s^2} - \frac{1}{D_{\text{sys}}^2 s}\left(2H_{\text{sys}}C_1 + D_{\text{sys}}\left(\Delta P_{\text{e}} + C_2 - \sum_i^E \Delta P_{\text{ess}}^{\text{ref},i}\right)\right)$$
$$+ \frac{1}{D_{\text{sys}}^2(2H_{\text{sys}}s + D_{\text{sys}})}\left(\beta - 4H_{\text{sys}}^2 D_{\text{sys}}\gamma\right) + \sum_i^E \frac{\tau_i^2}{2H_{\text{sys}} - D_{\text{sys}}\tau_i} \cdot \frac{\Delta P_{\text{ess}}^{\text{ref},i}}{\tau_i s + 1}$$

The $\frac{1}{\tau_i s+1}$ terms are neglected, assuming that the ESS act much faster than the SGs, so that a closed-form solution is available. The inverse Laplace gives the time-domain frequency expression.

$$\Delta\omega(t) = \frac{C_1}{D_{\text{sys}}}t - \frac{1}{D_{\text{sys}}^2}\left(2H_{\text{sys}}C_1 + D_{\text{sys}}\left(\Delta P_{\text{e}} + C_2 - \sum_i^E \Delta P_{\text{ess}}^{\text{ref},i}\right)\right) + \frac{1}{2D_{\text{sys}}^2 H_{\text{sys}}}\left(\beta - 4D_{\text{sys}}H_{\text{sys}}^2\gamma\right)e^{-\frac{D_{\text{sys}}}{2H_{\text{sys}}}t}$$

By taking the derivative to zero, the nadir time can be found.

$$t_{\text{nadir}} = \frac{2H_{\text{sys}}}{D_{\text{sys}}}\ln\left(\frac{\beta - 4D_{\text{sys}}H_{\text{sys}}^2\gamma}{4H_{\text{sys}}^2 C_1}\right)$$

The frequency nadir can be found as a function of the electrical disturbance and the ESS setpoint changes.

$$\Delta\omega_{\text{nadir}} = \frac{2H_{\text{sys}}C_1}{D_{\text{sys}}^2}\ln\left(\frac{\beta - 4D_{\text{sys}}H_{\text{sys}}^2\gamma}{4H_{\text{sys}}^2 C_1}\right) - \frac{1}{D_{\text{sys}}}\left(\Delta P_{\text{e}} + C_2 - \sum_i^E \Delta P_{\text{ess}}^{\text{ref},i}\right)$$

What follows is similar to the derivations without the ESS. We let $\omega_{\text{nadir}} = -|\Delta\omega_{\text{lim}}|$, and manipulate the equation so that an explicit solution can be represented by the Lambert W function. The maximum electrical disturbance is

$$\Delta P_{\text{e,max}} = -\frac{2H_{\text{sys}}C_1}{D_{\text{sys}}}(w_{-1}^{\text{E}} + 1 + \frac{C_3 D_{\text{sys}}^2}{4H_{\text{sys}}^2 C_1} - \frac{D_{\text{sys}}\gamma}{C_1}) - C_2$$

where

$$w_{-1}^{\text{E}} = W_{-1}\left(-\exp\left(-\frac{D_{\text{sys}}}{2H_{\text{sys}}C_1}\sum_i^E \Delta P_{\text{ess}}^{\text{ref},i} - \frac{D_{\text{sys}}^2|\Delta\omega_{\text{lim}}|}{2H_{\text{sys}}C_1} - 1 - \frac{C_3 D_{\text{sys}}^2}{4H_{\text{sys}}^2 C_1} + \frac{D_{\text{sys}}\gamma}{C_1}\right)\right)$$

The linearized equation around the point of zero ESS contribution is

$$\Delta P_{\text{e,max}} \approx (\Delta P_{\text{e,max}})_{\Delta P_{\text{ess}}^{\text{ref},i}=0} + \sum_i^E \left(\frac{\partial \Delta P_{\text{e}}}{\partial \Delta P_{\text{ess}}^{\text{ref},i}}\right)_{\Delta P_{\text{ess}}^{\text{ref},i}=0} \Delta P_{\text{ess}}^{\text{ref},i}$$

where $(\Delta P_{\text{e,max}})_{\Delta P_{\text{ess}}^{\text{ref},i}=0}$ is the maximum power imbalance without ESS support.

$$(\Delta P_{\text{e,max}})_{\Delta P_{\text{ess}}^{\text{ref},i}=0} = -\frac{2H_{\text{sys}}C_1}{D_{\text{sys}}}\left(w_{-1} + 1 + \frac{C_3 D_{\text{sys}}^2}{4H_{\text{sys}}^2 C_1} + \frac{C_2 D_{\text{sys}}}{2H_{\text{sys}}C_1}\right)$$

We note that the derivative of the Lambert W function is

$$\frac{dW(x)}{dx} = \frac{W(x)}{x(1+W(x))}$$

and use this to find the partial derivatives in the linear expression.

$$\left(\frac{\partial \Delta P_{\mathrm{e}}}{\partial \Delta P_{\mathrm{ess}}^{\mathrm{ref},i}}\right)_{\Delta P_{\mathrm{ess}}^{\mathrm{ref},i}=0} = \frac{2H_{\mathrm{sys}}}{2H_{\mathrm{sys}} - D_{\mathrm{sys}}\tau_i}\left(1 - \frac{D_{\mathrm{sys}}\tau_i}{2H_{\mathrm{sys}}}\left(\frac{w_{-1}}{1+w_{-1}}\right)\right)$$

Combining the expressions, the full linearized constraint is

$$\Delta P_{\mathrm{e,max}} = \underbrace{-\frac{2H_{\mathrm{sys}}C_1}{D_{\mathrm{sys}}}\left(w + 1 + \frac{C_3 D_{\mathrm{sys}}^2}{4H_{\mathrm{sys}}^2 C_1} + \frac{C_2 D_{\mathrm{sys}}}{2H_{\mathrm{sys}}C_1}\right)}_{\text{max load without ESS participation}}$$
$$\underbrace{+\sum_i^E \left(\frac{2H_{\mathrm{sys}}}{2H_{\mathrm{sys}} - D_{\mathrm{sys}}\tau_i}\left(1 - \frac{D_{\mathrm{sys}}\tau_i}{2H_{\mathrm{sys}}}\left(\frac{w}{1+w}\right)\right)\Delta P_{\mathrm{ess}}^{\mathrm{ref},i}\right)}_{\text{combined effect of ESS setpoint changes}}$$

Bibliography

[1] E. L. Ratnam, K. G. Baldwin, P. Mancarella, M. Howden, and L. Seebeck, "Electricity system resilience in a world of increased climate change and cybersecurity risk," *The Electricity Journal*, vol. 33, no. 9, p. 106833, 2020, special Issue: The Future Electricity Market Summit. [Online]. Available: https://www.sciencedirect.com/science/article/pii/S1040619020301251

[2] M. Macmillan, K. Wilson, S. Baik, J. P. Carvallo, A. Dubey, and C. A. Holland, "Shedding light on the economic costs of long-duration power outages: A review of resilience assessment methods and strategies," *Energy Research & Social Science*, vol. 99, p. 103055, 2023. [Online]. Available: https://www.sciencedirect.com/science/article/pii/S2214629623001159

[3] J. Minkel, "The 2003 northeast blackout–five years later," *Scientific American*, vol. 13, pp. 1–3, 2008.

[4] North American Electric Reliability Corporation (NERC), "System restoration from blackstart resources," NERC, Atlanta, GA, USA, Tech. Rep. EOP-005-3, 2018. [Online]. Available: https://www.nerc.com/pa/Stand/Reliability%20Standards/EOP-005-3.pdf

[5] U. Knight, *Power Systems in Emergencies: From Contingency Planning to Crisis Management*. Wiley, 11 2013.

[6] F. Qiu and P. Li, "An integrated approach for power system restoration planning," *Proc. IEEE*, vol. 105, no. 7, pp. 1234–1252, 2017.

[7] B. Vargas, "An essential guide to power system restoration," https://medium.com/@brandonvar/an-essential-guide-to-power-system-restoration-e5a7f0797575, 2023.

[8] Independent Electricity System Operator (IESO), "Part 7.8: Ontario power system restoration plan," IESO, Toronto, ON, Canada, Tech. Rep., 2022. [Online]. Available: https://www.ieso.ca/rules/-/media/24a42a9238b6482687c2ec2203a1e4e4.ashx

[9] P. Anderson, A. Fouad, and Institute of Electrical and Electronics Engineers, *Power System Control and Stability*, ser. IEEE Press power engineering series Power system control and stability. Wiley, 2003.

[10] L. Meng, J. Zafar, S. K. Khadem, A. Collinson, K. C. Murchie, F. Coffele, and G. M. Burt, "Fast frequency response from energy storage systems—a review of grid standards, projects and technical issues," *IEEE transactions on smart grid*, vol. 11, no. 2, pp. 1566–1581, 2019.

[11] C. Li, S. Zhang, J. Zhang, J. Qi, J. Li, Q. Guo, and H. You, "Method for the energy storage configuration of wind power plants with energy storage systems used for black-start," *Energies*, vol. 11, no. 12, p. 3394, 2018.

[12] P. Denholm, T. Mai, R. W. Kenyon, B. Kroposki, and M. O'Malley, "Inertia and the power grid: A guide without the spin," National Renewable Energy Lab.(NREL), Golden, CO, US, Tech. Rep., 2020. [Online]. Available: https://www.osti.gov/biblio/1659820

[13] New York Independent System Operator (NYISO), "Manual 20: System restoration manual," NYISO, Rensselaer, NY, United States, Tech. Rep., 2024. [Online]. Available: https://www.nyiso.com/documents/20142/2923301/srp_mnl.pdf/4a4cb29a-f935-0714-b8be-5d7718bdcbc2

[14] ——, "Miso power system restoration plan," MISO, Carmel, IN, United States, Tech. Rep., 2025. [Online]. Available: https://cdn.misoenergy.org/20220505%20SRRTWG%20Item%2003c%20SO-P-PSR-01%20Rev%205%20MISO%20Power%20System%20Restoration%20Plan_Supplemental624427.pdf

[15] M. Adibi, P. Clelland, L. Fink, H. Happ, R. Kafka, J. Raine, D. Scheurer, and F. Trefny, "Power system restoration - a task force report," *IEEE Trans. Power Syst.*, vol. 2, no. 2, pp. 271–277, 1987.

[16] ——, "Power system restoration - a task force report," *IEEE Trans. Power Syst.*, vol. 2, no. 2, pp. 271–277, 1987.

[17] M. Adibi, L. Fink, J. Giri, D. Kirschen, S. Shahidehpour, and J. Zaborszky, "New approaches in power system restoration," *IEEE Transactions on Power Systems (Institute of Electrical and Electronics Engineers);(United States)*, vol. 7, no. 4, 1992.

[18] M. Adibi, L. Kafka, and D. Milanicz, "Expert system requirements for power system restoration," *IEEE Transactions on Power Systems*, vol. 9, no. 3, pp. 1592–1600, 1994.

[19] M. Adibi, G. Adsunski, R. Jenkins, and P. Gill, "Nuclear plant requirements during power system restoration," *IEEE Transactions on Power Systems*, vol. 10, no. 3, pp. 1486–1491, 1995.

[20] M. Adibi and D. Milanicz, "Protective system issues during restoration," *IEEE Transactions on Power Systems*, vol. 10, no. 3, pp. 1492–1497, 2002.

[21] D. Lindenmeyer, H. Dommel, and M. Adibi, "Power system restoration—a bibliographical survey," *International journal of electrical power & energy systems*, vol. 23, no. 3, pp. 219–227, 2001.

[22] Y. Liu, R. Fan, and V. Terzija, "Power system restoration: a literature review from 2006 to 2016," *Journal of Modern Power Systems and Clean Energy*, vol. 4, no. 3, pp. 332–341, 2016.

[23] C. Coffrin and P. Van Hentenryck, "Transmission system restoration with co-optimization of repairs, load pickups, and generation dispatch," *International Journal of Electrical Power & Energy Systems*, vol. 72, pp. 144–154, 2015, the Special Issue for 18th Power Systems Computation Conference. [Online]. Available: https://www.sciencedirect.com/science/article/pii/S0142061515001106

[24] Y. Xie, S. Cai, J. Wang, Y. Chen, and C. Qiu, "A milp-based power system parallel restoration model with the support of mobile energy storage systems," *Electric Power Systems Research*, vol. 234, p. 110592, 2024. [Online]. Available: https://www.sciencedirect.com/science/article/pii/S0378779624004784

[25] P. Van Hentenryck and C. Coffrin, "Transmission system repair and restoration," *Mathematical Programming*, vol. 151, no. 1, pp. 347–373, Jun. 2015, publisher Copyright: © 2015, Springer-Verlag Berlin Heidelberg and Mathematical Optimization Society.

[26] N. Rhodes, C. Coffrin, and L. Roald, "Recursive restoration refinement: A fast heuristic for near-optimal restoration prioritization in power systems," *Electric Power Systems Research*, vol. 212, p. 108454, 2022. [Online]. Available: https://www.sciencedirect.com/science/article/pii/S0378779622005934

[27] F. Qiu, Y. Zhang, R. Yao, and P. Du, "Power system restoration with renewable participation," *IEEE Trans. Sust. Energy*, vol. 14, no. 2, pp. 1112–1121, 2023.

[28] A. Golshani, W. Sun, Q. Zhou, Q. P. Zheng, and Y. Hou, "Incorporating wind energy in power system restoration planning," *IEEE Transactions on Smart Grid*, vol. 10, no. 1, pp. 16–28, 2017.

[29] J. M. Miller, H. N. Villegas Pico, I. Dobson, A. Bernstein, and B. Cui, "Feedback control approaches for restoration of power grids from blackouts," *epsr*, vol. 211, p. 108414, 2022.

[30] H. Chávez, R. Baldick, and S. Sharma, "Governor rate-constrained opf for primary frequency control adequacy," *IEEE Transactions on Power Systems*, vol. 29, no. 3, pp. 1473–1480, 2014.

[31] P. Anderson and M. Mirheydar, "A low-order system frequency response model," *IEEE Transactions on Power Systems*, vol. 5, no. 3, pp. 720–729, 1990.

[32] Q. Shi, F. Li, and H. Cui, "Analytical method to aggregate multi-machine sfr model with applications in power system dynamic studies," *IEEE Transactions on Power Systems*, vol. 33, no. 6, pp. 6355–6367, 2018.

[33] H. Huang, P. Ju, Y. Jin, X. Yuan, C. Qin, X. Pan, and X. Zang, "Generic system frequency response model for power grids with different generations," *IEEE Access*, vol. 8, pp. 14 314–14 321, 2020.

[34] I. Egido, F. Fernandez-Bernal, P. Centeno, and L. Rouco, "Maximum frequency deviation calculation in small isolated power systems," *IEEE Transactions on Power Systems*, vol. 24, no. 4, pp. 1731–1738, 2009.

[35] L. Liu, W. Li, Y. Ba, J. Shen, C. Jin, and K. Wen, "An analytical model for frequency nadir prediction following a major disturbance," *IEEE Trans. Power Syst.*, vol. 35, no. 4, pp. 2527–2536, 2020.

[36] J. H. Chow and J. J. Sanchez-Gasca, *Power system modeling, computation, and control*. John Wiley & Sons, 2020.

[37] J. McCalley, "The power flow equations 1.0 the admittance matrix," 2011, for ECE458, Economic systems for electric power planning. [Online]. Available: https://home.engineering.iastate.edu/~jdm/ee458_2011/PowerFlowEquations.pdf

[38] M. L. Chan, R. D. Dunlop, and F. Schweppe, "Dynamic equivalents for average system frequency behavior following major distribances," *IEEE Transactions on Power Apparatus and Systems*, vol. PAS-91, no. 4, pp. 1637–1642, 1972.

[39] S. Bradley, A. Hax, and T. Magnanti, *Applied Mathematical Programming*. Addison-Wesley Publishing Company, 1977. [Online]. Available: https://books.google.ca/books?id=MSWdWv3Gn5cC

[40] D. Luenberger and Y. Ye, *Linear and Nonlinear Programming*, ser. International Series in Operations Research & Management Science. Springer US, 2008. [Online]. Available: https://books.google.ca/books?id=EJTrgq79QWUC

[41] A. B. Birchfield, "Graph decomposition for constructing blackstart restoration strategies in benchmark cases," *Electric Power Systems Research*, vol. 212, p. 108402, 2022.

[42] F. Bullo, *Lectures on Network Systems*. CreateSpace Independent Publishing Platform, 2018. [Online]. Available: https://books.google.ca/books?id=JpoxtwEACAAJ

[43] J. Löfberg, "Logics and integer-programming representations," 2016. [Online]. Available: https://yalmip.github.io/tutorial/logicprogramming

[44] Neplan AG, *Turbine-governor models: Standard dynamic turbine-governor systems in neplan power system analysis tool*, 2015.

[45] S. Dong, X. Fang, J. Tan, N. Gao, X. Cui, and A. Hoke, "A unified analytical method to quantify three types of fast frequency response from inverter-based resources," in *22nd Wind and Solar Integration Workshop (WIW 2023)*, vol. 2023. IET, 2023, pp. 669–674.

[46] J. Löfberg, "Yalmip : A toolbox for modeling and optimization in matlab," in *In Proceedings of the CACSD Conference*, Taipei, Taiwan, 2004.

[47] Gurobi Optimization, LLC, "Gurobi Optimizer Reference Manual," 2024. [Online]. Available: https://www.gurobi.com

[48] I. Farhat and X. Y. Zou, "BSPSSEPy application v0.4," 2025. [Online]. Available: https://github.com/aldahabi27/BSPSSEPy

[49] N. J. Higham, M. R. Dennis, P. Glendinning, P. A. Martin, F. Santosa, and J. Tanner, *Princeton companion to applied mathematics*. Princeton University Press, 2015.